Teng, Shi-Ping

ELECTRON TRANSPORT USING NEUTRAL PARTICLE TRANSPORT CODES

The University of Oklahoma PH.D. 1982

PLEASE NOTE:

In all cases this material has been filmed in the best possible way from the available copy. Problems encountered with this document have been identified here with a check mark __√__.

1. Glossy photographs or pages _____
2. Colored illustrations, paper or print _____
3. Photographs with dark background _____
4. Illustrations are poor copy _____
5. Pages with black marks, not original copy ✓
6. Print shows through as there is text on both sides of page _____
7. Indistinct, broken or small print on several pages _____
8. Print exceeds margin requirements _____
9. Tightly bound copy with print lost in spine _____
10. Computer printout pages with indistinct print _____
11. Page(s) _____ lacking when material received, and not available from school or author.
12. Page(s) _____ seem to be missing in numbering only as text follows.
13. Two pages numbered _____. Text follows.
14. Curling and wrinkled pages _____
15. Other _____

THE UNIVERSITY OF OKLAHOMA

GRADUATE COLLEGE

ELECTRON TRANSPORT USING NEUTRAL PARTICLE TRANSPORT CODES

A DISSERTATION

SUBMITTED TO THE GRADUATE FACULTY

in partial fulfillment of the requirements for the

degree of

DOCTOR OF PHILOSOPHY

BY

SHI-PING TENG

Norman, Oklahoma

1982

ELECTRON TRANSPORT

USING NEUTRAL PARTICLE TRANSPORT CODES

A DISSERTATION

APPROVED FOR THE SCHOOL OF AEROSPACE, MECHANICAL

AND NUCLEAR ENGINEERING

APPROVED BY

Duane Lindstrom

Charles W. Tindall

Craig M. Jensen

Luther W. White

David W. Anderson

Emin Ilmaz

DISSERTATION COMMITTEE

ABSTRACT

Success of electron beam therapy depends on the ability to deliver a prescribed radiation dose to a tumorous region. ETRAN, a Monte Carlo electron transport code is the most widely used tool for predicting electron interactions with matter. However, ETRAN results vary by as much as 15% from measured values. The objective of this research is to produce an alternative to ETRAN by applying radiation transport techniques familiar to nuclear engineers. Two computer codes for neutral particle transport have been used. One is a discrete ordinates code ANISN which offers a different approach from ETRAN. The other is a Monte Carlo code MORSE-E which has the capability to model the geometric complexities that occur in measurements. A group-skipping model developed in this work for the preparation of ANISN format electron transport cross sections has been used in calculations by ANISN and MORSE-E.

For the case of a 10 MeV electron beam incident on a water phantom, the energy deposition distribution predicted by ANISN is indistinguishable from that calculated by MORSE-E. The ANISN/MORSE-E results show better agreement with the measured depth dose data than ETRAN calculations. Two-dimensional irradiation geometry calculations by the use of MORSE-E are performed to predict the central-axis depth dose distribution with various sizes of beam field and compared to measured values. Other

types of problems which have been solved by ANISN/MORSE-E are: transmitted electron energy/angular distributions in water, aluminum and gold; charge deposition distribution in a water phantom. The calculated results are compared with ETRAN predictions and with available experimental results.

ACKNOWLEDGMENT

The author wishes to express appreciation to his advisor Dr. Duaine G. Lindstrom for his valuable guidance. Thanks are also offered to Dr. Charles W. Terrell for his suggestions and assistance. The author also wishes to express his sincere gratitude to his wife, Nai-Chi, for her understanding and assistance during the preparation of this dissertation.

TABLE OF CONTENTS

LIST OF TABLES

LIST OF ILLUSTRATIONS

FIGURE Page

CHAPTER I

INTRODUCTION

A. Background to the Investigation

Cancer probably is of more significance to most people today than any other form of disease. According to a recent report [1] more than 400,000 persons died from cancer in the United States in 1981. The death rate continually rises, despite advances in diagnosis and treatment. This is largely because of the increased longevity of the population. More and more persons are living to the ages where certain cancers show their highest incidence.

The most dominant method of cancer treatment is surgical excision. Chances of recovery are good when the cancer is still confined to the organ or tissue in which it develops. The application of surgical removal is limited by the degree of usefulness of the organ that must be removed.

Chemical and biological agents provide the other main method of cancer treatment. Chemotherapy became an effective tool in cancer treatment by the use of toxic radicals in conjunction with chemical substances that are required by the cancerous cell for its metabolism and division [2]. When the cancer cell ingests or absorbs these compounds, it tends to be sterilized or killed.

Radiation therapy, which was empirical two decades ago, became relatively standardized and quite accurate in application in recent years. An immense body of knowledge was accumulated concerning the radiation sensitivity of various cancers. Also the dosages of radiant energy necessary to destroy various cancers became well-known. By itself, radiotherapy is an increasingly potent tool. The basis of the value of radiation therapy in the treatment of cancer lies in the fact that ionizing radiation produces more damage in malignant than in non-malignant tissues (3). A dose of radiation sufficient to kill cancer cells will produce considerable, but not irreparable, damage to normal tissue, so that the latter recovers whereas the malignant tissue does not. The aim of radiation therapy is the delivery of a known and uniform dose of radiation to a zone believed to encompass the tumor, and as little radiation as possible elsewhere.

Radiation therapy can be conveniently divided into three categories based upon the distance between the radiation source and the malignant tumor (4).

1. Internal Therapy. - This form of treatment is entirely by means of radioactive isotopes which emit beta particles and/or gamma rays. In some form or another, the radioactive isotopes are incorporated into body tissues.

2. Plesiotherapy. - This is the general term applied to indicate those forms of radiation therapy where the radiation source is close to the tissues being treated. This includes treatments where small beta , or gamma-ray sources (for example

cesium 137, cobalt 60, and iridium 192) are placed within a centimeter or two of the body surface, or gamma-ray sources are actually implanted into the tissues.

3. Teletherapy. - This is generally applied to treatments when the external source of radiation is many centimeters from the part being treated. Beams of X- and gamma-rays, high-energy electrons, and neutrons have all been used in this way. Dependent upon the depth of the tumor in the body, it requires beams of various penetrating powers. Also, to allow for the various tumor shapes and sizes, it calls for beams of different shapes and sizes which are produced by suitable collimators or trimmers.

Among the above mentioned methods of cancer treatment, high-energy electron beam therapy, being the selected topic of this research, is reviewed in the following paragraphs.

Historically, the first successful application of high energy electrons to patients was accomplished by Harvey, Hass and Laughlin in 1951 [5]. During the past three decades, as machines capable of accelerating electrons to high energy become more widely available, considerable clinical trials have been focused on the possibilities of using an electron beam as a therapeutic agent. In recent years, electron beams have become an important asset to radiation therapy and have played an increasingly important role in the treatment of malignant tumors.

The main advantage of high-energy electron beam therapy is the uniform dose it produces in the first few centimeters of tissue, and the subsequent very sharp fall-off of the dose.

Electron irradiation also permits easy manipulations and convenient adjustment of the depth of penetration of radiation. Therefore, it becomes the most suitable type of radiation at the present time for treating diseases which extend from the skin surface to a few centimeters depth. For the example of the cases of breast cancer, Chu [6] reported that the results of electron beam therapy appear to be comparable with super-voltage X-ray irradiation with lessened probability of lung complication.

The University of Oklahoma Health Sciences Center is equipped with the SAGITTAIRE electron accelerator for radiation therapy. This facility is used to treat cancer patients with beams of electrons with selected energies up to 40 MeV and beams of 25 MeV X-rays. Measurements of relative energy deposition versus depth, also known as 'depth dose measurements', in phantom material are available for a number of incident electron energies and beam areas from the SAGITTAIRE electron accelerator [7]. These measurements form the basis of comparison of the results predicted by the analysis methods in this report.

B. Problems in the Prediction of Depth Dose Curves

Excessive irradiation leads to the destruction of the healthy tissues as well as the cancer. Conversely, inadequate dosage fails to kill the cancer cells, so that after a time they recover from such damage and start to multiply again. To treat cancer patients safely and efficiently, the therapy units (radiotherapist, physicist and radiotheraphy technician) must administer the proper amount of radiation therapy dose. Safe

and efficient treatments can only be performed when at least approximate optimum dosage levels have been established. These can only be known after considerable clinical observation of the effects of known doses of radiation. Good electron beam therapy requires not only accurate, but also constant dosimetry. Because of the undesirable consequences of over- and under-dosage, the general aim of electron beam therapy is to deliver as uniform a dose of electron beam as possible to all parts of the cancer-bearing zone. Outside this zone, as low a dose as possible is the goal.

To administer the accurate dosage, a therapy physicist needs to know the absorbed dose of radiation that would result at a reference point and at any points within the patient. These measurements are necessary to obtain trustworthy distributions of absorbed dose for general treatment planning in radiology. The reference point is determined by the conditions under which the calibration was made. Further measurements at other points in the irradiated medium may require some correction factors due to different absorbed dose distribution and different energy distribution in the beam. Factors influencing these absorbed dose distributions under conditions relevant to therapeutic applications are discussed in the ICRU Report 21[8].

The commonly used reference point for electron beam therapy is the point of maximum absorbed dose. In such case the absorbed dose at the point of interest is expressed as

a percentage of that at the reference point and is called the percent depth dose. Its value at the reference point is 100.

For fairly obvious reasons, it is impractical to make the required measurements either on, or inside, patients. Therefore, it is necessary to find some material which attenuates the electron beam and absorbs radiation energy as closely as possible to the way in which the human body attenuates and absorbs. Such material then can be used as a 'phantom' in which measurements can be made.

To have closely similar absorbing and attenuating properties, two materials must have similar atomic numbers, densities, and electron densities. For muscle tissue the values of these quantities are, respectively, 7.42, 1.0 gram per c.c., and 3.36×10^{23} electrons per gram. The common material with the closest resemblance to these values is water (Z = 7.42, density = 1.0 gram per c.c., and electron density = 3.34×10^{23} electrons per gram)[4]. Water, therefore, has been generally regarded as the most acceptable material for standard radiation dosimetric measurements.

Although water is a good phantom material, when photographic film is used to measure the radiation dose, a phantom of solid material is more convenient, and many different materials have been tried. The most suitable water equivalent material for electron dosimetry is polystyrene. However, it cannot be considered as a perfect substitute for water due to its smaller density, 0.97 grams per c.c.[8].

Depth dose curves have been reported by many researchers. However, their experimentally determined depth dose curves show great discrepancies at small phantom depths [9]. It is commonly believed that the actual absorbed dose at the surface of a water equivalent medium usually is about 85% of the maximum in the absence of contamination of the beam [8]. However, the surface dose for 10 MeV electrons with various beam areas were measured to be between 87% to 93% at the University of Oklahoma Health Sciences Center. The apparent uncertainty might be reduced if certain analysis methods are adapted to provide the appropriate details of radiation energy deposition in therapy conditions.

The one-dimensional electron transport computer code ETRAN [10] was used [13] to simulate 10 MeV measurements using the physical characteristics of electron-water interactions. They were compared with similar calculations reported in the literature for ETRAN [11] and for a comparable code [12]. The results were nearly indistinguishable from the published results but the surface dose was about 70% of the maximum. This difference may imply that the measured beam may contain radiation other than electrons or electrons with energies less than 10 MeV. These low energy electrons and photons are produced by interactions of the electron beam with air and with the collimators and trimmers used to define the beam area. This difference may also indicate that one should be cautious in using the ETRAN code to calculate the energy deposition in media.

In recent years, some developments have been reported in electron transport calculation using the discrete ordinates method [54]. But their results were unsatisfactory and none of them has yet been developed into a generally useful computer code.

Recently, Özdemir [13] employed a computer code ANISN [14], which was developed for neutral partical transport analysis, to calculate electron transport data. The depth dose curve predicted by his continuous-slowing-down-model was in agreement with the experimental data. However, some mathmatical inconsistencies have been found in the data prepared for the continuous-slowing-down-model, bringing these results into question. Özdemir's work will be discussed in detail later in this report.

C. Aims of This Study

One major drawback of the computer codes commonly used for electron transport analysis lies in the fact that they (ETRAN and ANISN) are capable of treating only a single-space-dimension (depth). In the pratical system of electron beam therapy, the geometry is multi-dimentional. This system can not be completely described by either ETRAN or ANISN. The two-dimentional discrete ordinates codes; e.g., DOT[15] and TWOTRAN[16], open the door to a much broader range of physical problems. They, however, suffer from the requirement of larger machine storage and greatly increased computer running time. As a result, multi-dimensional discrete ordinates codes have not been as fully developed nor as widely used as their one-dimensional counterparts.

In many electron transport problems where perfectly valid assumptions can not be made to reduce the geometry complexity, the use of a multi-dimensional Monte Carlo neutron transport calculation appears to be a practical approach worth investigating. The logic of the random walk process is identical for neutrons, gamma rays and electrons. Thus, many familiar Monte Carlo codes for uncharged particles can be used for the electron transport calculations so long as the appropriate cross sections for electrons can be provided. A few of the existing Monte Carlo codes use multigroup cross-sections in the same form as discrete ordinates codes. In discrete-ordinates type calculations the machine running time is almost directly proportional to the number of energy groups. The running time for the Monte Carlo method, however, is almost independent of the number of energy groups. In this study, the electron transport problems will be modeled with the multi-group, three-dimensional Monte Carlo code MORSE (17,18).

In this report, the interactions of electron with matter are reviewed and the evaluation processes concerning the transport of electrons are reexamined. The present state of electron transport studies is also discussed in this work.

The aims of this study include:

1. For practical purposes, standardizing the continuous-slowing-down model in a multi-group cross section production code to make it usable by the scientific community with existing

transport codes.

2. Extending Özdemir's model to consider slowing down to energies below the next group. In other words, change the model from continuous-slowing-down to a model which allows larger energy changes.

3. Extending Özdemir's work to take the transport of secondary electrons into consideration.

4. Comparing the predicted results of MORSE with measurements at the University of Oklahoma Health Sciences Center and also with the calculated results of ETRAN and ANISN.

CHAPTER II

REVIEW OF ELECTRON TRANSPORT THEORY

A. Introduction

Electron penetration through matter has been studied for over eighty years [19]. From the earliest scattering experiments of Rutherford to the sophisticated high-energy experiments of today, studies of the interactions of electrons with the matter through which they pass have been very informative. An understanding of these interactions has led to a more detailed knowledge of atomic and nuclear structure, to a better insight into the nature of the radiations themselves, and to their effects on living systems. Details of electron absorption are of particular interest since they are the particles produced in all of the common processes by which photons give up their energy.

Several authors including Evans [20], Bethe and Ashkin [21], Zerby and Keller [22], and Fano [23] have extensively reviewed the principal interactions that contribute to the transport of electrons through matter. The intent here is to summarize briefly these interactions for reference in the subsequent chapters of this work.

In any discussion of electron penetration, it is absolutely

necessary to state the range of energy of the electrons which interact with the atoms. This is because of the fact that in the very low range of a few eV, and in the very high range of the order of 100 MeV, different processes dominate the interaction which are of no or little importance in the range of 10 KeV to 10 MeV. In this research, the work is restricted to the last mentioned energy range.

B. Basic Electron Interactions with Matter

1. Introduction

When electrons, in the energy range of interest in this work, penetrate matter, they undergo a large number of collisions within a very short pathlength. Since there are many possible energy and angular changes for each collision, this results in a distribution of electrons in terms of both energy and direction of motion. The most essential interactions for the prediction of the resulting distribution by transport calculations include elastic nuclear scattering (Coulomb scattering), inelastic scattering from atomic electrons, and radiative (bremsstrahlung) interactions with both nuclei and atomic electrons.

The nuclear Coulomb scattering cross section and the electron scattering cross sections are both very large and produce scattered distributions concentrated mostly in the forward direction. These interactions lead to a very large number of small-angle scattering collisions as the electron traverses even a small distance in the transport medium. Dispersed among the small-angle scattering is an occasional large-angle scattering.

In the case of scattering by atomic electrons, this large-angle scattering gives rise to a secondary knock-on electron (or delta ray) which is ejected from the atomic structure. Because the mass of a target nucleus is so much greater than that of the electron, the energy lost by the electron is negligible in nuclear Coulomb scattering. The dominant mode of electron energy loss, in the energy range of interest in this work, is through inelastic collisions with the bound electrons of the atoms or molecules of the transport media. The atoms are either ionized, with the ejection of an electron, or left in an excited state. The incident electron can transfer a significant fraction (up to half) of its energy to the target. Since the electron-electron cross section is large, the energy transfer to the target leads to a rapid loss of energy by the primary electron as it traverses the medium.

The emission of secondary bremsstralung photons in radiative collisions is another mechanism of electron energy degradation. The radiative collisions deflect the incident electron as well as create secondary radiation. The extent of this deflection, however, is usually negligible compared to the deflection resulting from the much more frequent scattering by nuclei and atomic electrons [22].

2. Energy Loss

For electrons of relatively low energy, the energy loss in matter is due to excitation and ionization of the bound electrons in the stopping substance. For high energies, however, the main energy loss of electrons is due to the emission of electromagnetic

radiation in the electric field of the nuclei of the stopping material. An electron in the Coulomb field of a nucleus can experience a large acceleration by virtue of its small mass, the aceleration being proportional to the nuclear charge Z divided by the electron mass m. The resulting radiation (bremsstrahlung) is the dominant influence in the energy loss of fast electrons. The energy at which the two above mentioned loss are equal is called the critical energy. This energy is often represented as a function of the atomic number Z by [22]

$$E_{critical} = \frac{800}{Z + 1.2} \text{ MeV} \qquad (2.1)$$

which has been independently verified by the calculations of Berger and Seltzer [24].

It is not possible to say which of the two electrons emerging from an inelastic collision was the incident electron and which is the freed electron. By convention, the electron with the higher energy is taken to be the primary. This results in the maximum possible energy of a secondary electron being half of the energy of the incident electron before the interaction. By convention, then, the energy loss in an interaction is the difference between the incident and primary electron energies.

The average rate of energy loss due to ionization and excitation is represented by the collision stopping power. For relativistic velocities the energy loss per centimeter has been worked out by Bethe [26] on the basis of Møller's [27] formula for the scattering of electrons by electrons. The result is

$$-\left(\frac{dE}{dx}\right)_c = \frac{2\pi Ne^4}{mv^2} Z\left(\ell n \frac{mv^2 E}{2I^2(1-\beta^2)} - (2\sqrt{1-\beta^2} - 1 + \beta^2)\ell n 2 + (1-\beta^2) + \frac{1}{8}(1-\sqrt{1-\beta^2})^2 \right) \qquad (2.2)$$

where e = charge on the electron, esu

N = number of absorbing atoms per c.c.

Z = atomic number of the absorber

I = average excitation potential, ergs

m = rest mass of the electron

v = velocity of the incident electron

β = v/c for the electron

E = kinetic energy of the incident electron.

A complete discussion of the energy loss of an electron by radiative collisions has been given by Bethe and Heitler [28]. The average rate of energy loss due to bremsstrahlung production can be represented by the radiative stopping power. The result is [29]

$$-\left(\frac{dE}{dx}\right)_r = \frac{NEZ(Z+1)\, e^4}{137\, m^2 c^4} \left(4 \ell n \frac{2E}{mc^2} - \frac{4}{3}\right), \qquad (2,3)$$

where the terms have the same meanings as in Eq. (2.2).

Comparison of Eq. (2.3) with (2.2) for the energy loss by ionization and excitation collisions shows that the radiative energy loss has a strikingly different behavior. Owing to radiation the energy loss is proportional to Z(Z + 1) and increases linearly with energy, while, owing to collisions, the energy loss

is proportional to Z and increases only logarithmically with energy. Thus, in lead, radiation and collision losses are about equal at 15 MeV; in air, equality is reached at about 250 MeV [29]. The critical energy for water is about 93 MeV [25]. For 10 MeV electron incident on water, the fraction of energy loss by radiative collisions is about 8%.

3. Scattering

In both of the energy loss mechanisms described above, the primary electron is deflected. In the elastic Coulomb interactions between the electron and the heavy nucleus of charge Z, the electron is also deflected with no loss of energy. It is the large number of such elastic scatterings which produce the characteristic multiple-scattering effects discussed in Section C of this chapter.

Since elections have so small a mass, they may be deflected through large angles by the electric field of an atom without passing in the immediate neighborhood of the nucleus. Therefore, for the scattering of electrons by atoms, we expect the shielding of the nuclear charge by the orbital electrons in the atom to play an important role. Rutherford first derived the distribution of the electron deflections assuming that the nucleus was a point charge [30]. More refined treatments have included the effect of the finite size of the nucleus and the screening of the nuclear field by the atomic electrons. Goudsmit and Saunderson [31] developed an expression for the screened Rutherford cross section using the Bohr approximation where the

potential form $V = Ze^2 r^{-1} \exp(-r/a)$ was used to represent the electrostatic field of the atom. The resulting cross section is

$$d\delta = \frac{2\pi e^4 Z^2}{p^2 v^2} \cdot \frac{\sin\theta \, d\theta}{(1+\cos\theta+0.5\theta_1)^2} \quad , \tag{2.4}$$

where p is the relativistic momentum of the incident electron, $\theta_1 = \lambda\!\!\!^{-}/a$, $\lambda\!\!\!^{-} = \hbar/p$, and $a = a_o Z^{-1/3}$ with $a_o = \hbar^2/me^2$ (the Bohr radius).

C. Multiple Interaction of Electrons

1. Introduction

In the course of slowing down, an electron not only loses energy by numerous colisions, but also makes multiple small-angle changes in direction from its original paths. This makes it possible to describe the behavior of an electron with reasonable accuracy by making use of multiple-collision statistical models. Various theories have been developed to estimate the energy distribution of an electron after it has travelled a given distance. Distributions have also been calculated for the size of the deflection angle after the electron has traversed a given depth. An example is the continuous slowing down model of Bethe [32] for the energy loss per unit path length. Another is the multiple small-angle scattering theory of Fermi [25] which accounts for the lateral movement and change in direction as the electron moves a small fraction of its range. Both of these models, however, are approximate and have been modified to make them more accurate. Extensive reviews of the energy loss theory

and multiple scattering theory have been given by Bethe and Ashkin [21] and by Birkhoff [30].

2. Energy Loss

a) Continuous Slowing Down

The most comprehensive and thorough calculations of the stopping power for electrons have been published by Berger and Seltzer [24]. Their calculations were based on Bethe's stopping power theory [32] as formulated by Rohrlich and Carlson [33] and included the stopping power contribution from bremsstrahlung.

The electron-electron collision contribution was calculated from the expression

$$-\frac{1}{\rho}\left(\frac{dE}{dx}\right)_c = \frac{2\pi N_a r_o^2 mc^2}{\beta^2}\cdot\frac{Z}{A}\cdot\left(\ell n\left(\frac{T_o^2(T_o+2)}{2(I/mc^2)^2}\right)+F(T_o)-\delta\right), \quad (2.5)$$

where $F(T_o) = 1-\beta^2+\left(T_o^2/8 - (2T_o - 1)\ell_{n2}\right)/(T_o+1)^2$, (2.6)

and T = kinetic energy in mc^2 units

A = atomic number

ρ = density

δ = density effect correction

N_a = Avogadro's number

r_o = classical electron radius.

The bremsstrahlung contribution was calculated from

$$-\frac{1}{\rho}\left(\frac{dE}{dx}\right)_r = \frac{N_a}{A}\, mc^2 \int_o^{T_o} K d\sigma_K^{corr}, \quad (2.7)$$

where K is the energy of the photon in mc^2 units, and $d\sigma_K^{corr}$ is the bremsstrahlung cross section (which is differential in the photon energy) with Z^2 replaced with $Z(Z+1)$.

The total stopping power is

$$-\frac{1}{\rho}\left(\frac{dE}{dx}\right)_{tot} = -\frac{1}{\rho}\left(\frac{dE}{dx}\right)_c - \frac{1}{\rho}\left(\frac{dE}{dx}\right)_r , \qquad (2.8)$$

b) Energy Straggling

The use of the continuous-slowing-down approximation yields a unique mathematical relationship between the distance traveled by the electron and its residual energy. In fact, the relationship of nature is not unique since electrons experience discrete and sometimes large energy losses as they traverse a material. As a result, at any particular distance a spectrum of electron energies is possible.

The deviation of the energy of the electrons from the average is known as straggling and was first investigated by Williams [34]. Subsequent improvements have been made by Landau[35] and by Blunck and Leisegang [36]. Zerby and Keller [22] have given a summary of this work which is repeated here.

If an electron with initial energy T_o travels a distance X, it will suffer an energy loss by electron-electron collision, W, whose distribution has been derived by Landau for the case that $W << T_o$. His result can be expressed as

$$f_I(W)dW = f_L(\lambda)\, d\lambda \qquad (2.9)$$

where

$$\lambda = \frac{W - \bar{W}}{N C Z X} + \ell_n \left(\frac{T_o}{NZCX}\right) - 0.803 \qquad (2.10)$$

with N = atomic denrity, atoms/c.c.

$$C = \frac{2\pi r_o^2 (T_o + 1)^2}{T_o (T_o + 2)}$$

W = energy loss in mc^2 units

$\bar{W}$ = average energy loss in mc^2 units for traversing X cm.

The function $f_L(\lambda)$ was evaluated by Landau and is given by

$$f_L(\lambda) = \frac{1}{2\pi i} \int_{-i\infty + c}^{i\infty + c} \exp(u \ell_n u + \lambda u)\, du \qquad (2.11)$$

which has been tabulated by Borsch-Supan [37].

Blunck and Leisegung have refined Landau's theory by considering in more detail the binding of the atomic electrons to which the incident electron transfers its energy. This arrives at a broader distribution function $f_L^*(W)$ which is given as

$$f_L^*(W) = \frac{1}{NZCXb\sqrt{\pi}} \int_{-\infty}^{\infty} f_I(W-u) \exp\left(-\frac{u^2}{NZCXb}\right) du, \qquad (2.12)$$

where the broadening parameter b can be expressed as

$$b = \sqrt{Q \bar{W}}\ \frac{Z^{2/3} 10^{-3}}{NZCX} \qquad (2.13)$$

with $Q \cong 39.1$ eV.

Blunck and Westphal [38] have also considered the additional

broadening of the spectrum as a result of radiative energy losses and found that the combined distribution $f_{IR}(W)$ should be

$$f_{IR}(W) = \int_o^W f_I\ (W-\eta)\ f_R(\eta)d\eta \qquad (2.14)$$

where $f_R(\eta)$ is the probability distribution for radiative distribution similar to $f_I(W)$.

3. Multiple Scattering Theory [22]

As electrons travel through a stopping medium they not only lose energy by multiple interactions, but they are also deflected from their original paths as they make multiple discrete changes in direction. The analytical treatment of this process is difficult without extensive simplification. As a result of different approximations made, a number of approaches have been developed. Review of these approaches was given by Scott [39]. Of these various treatments, the Goudsmit-Saunderson [31] approach, which has been adopted by the Monte Carlo transport code ETRAN[10], is described below.

Goudsmit-Saunderson approach is directed at finding the angular distributions without regard to the lateral displacement. In the treatment of the angular distributions, this approach develops a theory valid for all angles by expanding the distribution function in a series of Legendre polynomials.

The Goudsmit-Saunderson aproach for electron multiple scattering is valid for an arbitrary scattering cross section, and it gives

$$F(\theta,t)\sin\theta d\theta = \sum_{\ell=0}^{\infty}(\ell+\tfrac{1}{2})\exp\left(-\int_0^t K_\ell(t')dt'\right) P_\ell(\cos\theta)\sin\theta d\theta, \quad (2.15)$$

$$\text{where } K_\ell(t) = 2\pi N\int_0^\pi \sigma(\theta,t)\left(1-P_\ell(\cos\theta)\right)\sin\theta\, d\theta \quad (2.16)$$

and $F(\theta,t)$ = the distribution function at depth t in material

$P_\ell(\cos\theta)$= a Legendre polynomial of degree n

$\sigma(\theta,t)$ = scattering cross section per unit solid angle

N = atoms per unit volume.

The cross section is actually a function of energy, but it is assumed in Eq.(2.16) that there is a unique relation between energy and distance t. The number of terms required in the sum in Eq.(2.15) may be very large, leading to slow convergence. Berger [40] for example, found that at 150° the use of twenty terms would give a result which is ten times too large in absolute value and has the wrong sign, and almost sixty terms are required to provide convergence to six significant figures.

CHAPTER III

NUMERICAL METHODS FOR ELECTRON TRANSPORT

A. Introduction

This research considers the following problem: A beam of electrons with kinetic energy Eo is incident on a phantom material. As the electrons penetrate into the phantom they lose energy and change directions. We want to determine the energy dissipated by the electrons at various locations in the phantom. This would be exactly the absorbed dose if we were able to follow all secondary particles to the ends of their paths.

The multiple interaction models that attempted to represent the behavior of electrons as they passed through matter were reviewed in Chapter II. In general, one common limitation exists in all these models. They are dependent upon the distance traveled in contrast to position. Since the path of the electron deviates from a straight line quite quickly, these models can only be applied to penetrations that are small fractions of the electron range. Additional approximations that ignore lateral displacements, such as in the Goudsmit-Saunderson theory, further restrict the applicability of the results.

Two techniques that eliminate most of the restrictive features of previous electron transport theories have been

developed for solution on computers. These include the transport methods and the Monte Carlo method. The transport methods include the numerical techniques for solving the transport equation. The Monte Carlo method is also a way to determine the flow of electrons and gamma rays. However, the Monte Carlo method may be related directly to the transport problem and need not be based directly on the Boltzmann transport equation. A discussion of these methods is presented in this chapter. The status of utilizing these methods in electron transport calculations is also reviewed.

B. Transport Methods

The basic equation of electron conservation is the Boltzmann transport equation. The general time-dependent integro-differential form of the Boltzmann transport equation, which can be derived by a bookkeeping process that sets the net storage of electrons within a differential element of phase space ($drdEd\Omega$) equal to the electron gains minus electron losses in ($drdEd\Omega$) and can be written as the following familiar form [17]:

$$\frac{1}{v}\frac{\partial}{\partial t}\phi(r,E,\Omega,t) + \Omega\cdot\nabla\phi(r,E,\Omega,t) + \Sigma_t(r,E)\phi(r,E,\Omega,t) = S(r,E,\Omega,t) + \int\int dE'\,d\Omega'\Sigma_s(r,E'\to E,\Omega'\to\Omega)\,\phi(r,E',\Omega',t), \qquad (3.1)$$

where

(r,E,Ω,t) denotes the general seven-dimensional phase space,

r = position variable,

E = the particle's kinetic energy,

v = the particle's speed corresponding to its kinetic energy E,

Ω = a unit vector which describes the particle's direction of motion,

t = time variable,

$\phi(r,E,\Omega,t)$ = the time-dependent angular flux,

$\phi(r,E,\Omega,t)dEd\Omega$ = the number of particles that cross a unit area normal to the direction per unit time at the space point r and time t with energies in dE about E and with directions that lie within the differential solid angle $d\Omega$ about the unit vector Ω,

$\frac{1}{v}\frac{\partial}{\partial t}\phi(r,E,\Omega,t)dEd\Omega$ = net storage (gains minus losses) per unit volume and time at the space point r and time t of particles with energies in dE about E and with directions which lie in $d\Omega$ about Ω.

$\Omega\cdot\nabla\phi(r,E,\Omega,t)dEd\Omega$ = net convective loss per unit volume and time at the space point r and time t of particles with energies in dE about E and directions which lie in $d\Omega$ about Ω,

$\Sigma_t(r,E)$ = the total cross section at the space point r for particles of energy E,

$\Sigma_t(r,E)o(r,E,\Omega,t)dEd\Omega$ = collision loss per unit volume and time at the space point r and time t of particles with energies in dE about E and directions which lie in $d\Omega$ about Ω,

$\Sigma_s(r,E'\rightarrow E,\Omega'\rightarrow\Omega)dEd\Omega$ = the differential scattering cross section which describes the probability per unit path that a particle with an initial energy E' and an initial direction Ω' undergoes a scattering collision at r which places it into a direction that lies in $d\Omega$ about Ω with a new energy in dE about E,

$\left(\iint \Sigma_s(r,E'\rightarrow E,\Omega'\rightarrow \Omega)x\phi(r,E',\Omega',t)dE'd\Omega'\right)$ $dEd\Omega$ = inscattering gain per unit volume and time at the space point r and time t of particles with energies in dE about E and directions which lie in $d\Omega$ about Ω,

$S(r,E,\Omega,t)dEd\Omega$ = source particles emitted per unit volume and time at the space point r and time t with energies in dE about E and directions which lie in $d\Omega$ about Ω.

A direct, analytic solution of the Boltzmann equation can be found only in a few very simple and highly idealized cases. For the most part, approximate solutions are all that are possible in practical situations. Approximate solutions can usually be obtained through numerical methods on high-speed computers.

Successful numerical solutions to the Boltzmann equation have been obtained with difference methods and iterative procedures. The approach commonly used requires the derivation of a difference approximation to the Boltzmann equation for each point of a mesh filling the transport medium. Steps in such a calcuation include [41]:

1). Choosing the appropriate division of energy groups..

2). Selecting a method of representing the differential scattering cross section and the angular dependence of the flux.

3). Integrating the Boltzmann equation over each energy group (cross section must be suitably averaged over each group).

4). Approximating the equations relating the spatial derivatives of the differential (energy and angle) flux as functions of r by a finite difference system at each mesh point.

5). Solving the resulting system of equations by an iterative method.

The moments method and the discrete ordinates method are two numerical techniques used for solving the transport equation. These methods are discussed in the following sections.

1. Moments Method [41,42,43]

The moments method was formulated by Spencer and Fano [44] for treating the Boltzmann equation. This method has been devised to treat the difficult problems of neutron and gamma-ray deep penetration by many investigators [45,46,47]. It was the first technique to be successfully applied to the transport equation for solutions useful to reactor shielding.

In the moments method one considers first the definition of moments and the manner in which they relate to some parameter of interest, say f(x). If f(x) is for all x within the interval (x_1,x_2), the n^{th} moment of f(x) is

$$M_n = \int_{x_1}^{x_2} x^n f(x)\, dx \qquad (3.2)$$

provided the integral exists. Only non-negative integer values of n are considered in practical application.

Definite interpretations may be associated with the various moments. For example, the zeroth moment is a normalizing number, the first and second moments are closely related to the mean value and variance respectively. In the physics of statics and dynamics, the first moment of the mass is the center of gravity and the second is the moment of inertia.

No such particular meanings are given to the moments as they are used in the solution of radiation transport problems. Rather, they are regarded as a transform, much the same as Laplace or Fourier transforms. The major portion of the calculation is performed in terms of the moments space; then, by an appropriate inversion, the desired answer is reconstructed.

The moments method can only be applied to solve the Boltzmann transport equation in a limited source-media configuration. It is usually applied only to infinite homogeneous media with point, line or plane sources.

The first step towards the application of the moments method to the theoretical treatment of the electron penetration was taken by H. W. Lewis. He reported formal expressions for spatial moments of the electron distribution with the approximation of a continuous slowing down model [48]. His treatment was based on the large angle multiple scattering in an infinite homogeneous medium. Both elastic and inelastic deflections were included in his derivation, the latter being considered as statistically independent of the energy losses. However, Lewis made no attempt to evaluate the moments numerically in a systematic way or to use them to obtain spatial distributions.

Spencer [43,49] derived methods for calculating spatial moments to treat the electron transport equation. In his works, the theory of electron penetration in an infinite medium under the combined influence of scattering and slowing down was developed to the point of numerical application. The transformation of spatial moments is quite tedious and is not repeated here.

Sample calculations of energy dissipation versus distance from the source showed good agreement with the experiments. However, the moments method is limited to application where the medium is unbounded and homogeneous. The extension of the theory to the treatment of practical boundary effects still represents a major obstacle.

2. Discrete Ordinates Method [50,51]

The method of discrete ordinates is commonly called the Sn method and was originated by B. G. Carlson [52]. It is based directly upon the solution of the transport equation by numerical methods. The characteristic feature of the Sn method is the assumption of linear variation of the directional flux between interpolation points in both the angular and spatial variations.

The essential bases of the discrete ordinates method is that the angular distribution of the particle flux is evaluated in a number of discrete directions, just as the spatial system is discretized into a number of spatial mesh pointsand the energy domain is broken into a number of groups. The n in Sn is related to the number of directions selected, therefore, the larger the n, the smaller the "angular mesh". Associated with each direction is a "window" or directional mesh area. All particles having directions that are subtended by a window are lumped into the direction associated therewith. The relative size of the window is called the "quadrature weight". Then, one can treat separately the transport for each of these directions and solve for the associated angular flux. The solutions approach the exact

solution of the Boltzmann equation as the energy, space and angle mesh approach differential size.

Basically, the discrete ordinates method is formulated as a finite-difference equation. It should be noted that a finite-difference equation is defined as an algebraic statement relating values of the discrete ordinate flux from point to point in phase space. By dividing the phase space into a finite number of discrete points and integrating the conservative form of the Boltzmann equation over a finite-difference cell in phase space, the difference equations that relate the flux at each point to the flux at neighboring points can be obtained. This procedure replaces the Boltzmann integro-differential equation with a system of simutaneous difference equations. These difference equations may then be solved numerically by an iterative technique.

Many discrete ordinates Sn computer codes are available for the scientific community to solve the deep penetration problem of neutrons and gamma-rays. The code ANISN is the most famous and commonly used one-dimensional anisotropic scattering code. However, no "discrete ordinates" electron-specific code has been available to date [53]. Fortunately, the Sn codes for uncharged particles can be employed to solve charged particle transport problems if the multigroup cross sections for the charged particles may be obtained. Because when multigroup cross sections are employed, the energy group to energy group transfers contain the cross sections for all interaction processes. The logic of the discrete ordinates approach is identical for both charged and uncharged particles.

The first attempt to adapt discrete ordinates method for the transport of electrons through matter was accomplished by Bartine et al. (54). Their investigation was focused on low energy (on the order of a few MeV) electrons in aluminum because of their specific concern for shielding of space vehicles. The discrete ordinates code they employed was ANISN. In principle, ANISN may be used to transport electrons by introduction into the code the differential cross sections for electron-nucleus elastic scatterings, electron-nucleus bremsstrahlung-producing collisions, and electron-electron collisions. In practice, however, these cross sections are quite different from those occuring in neutron transport, and the method has shown only partial success in transporting electrons. In their model, it is assumed that there is no angular deflection associated with inelastic electron-electron collisions and the large number of Coulomb interactions forces the use of a very large number of discrete intervals. It also requires that the ANISN code be revised to include a continuous energy loss term. Calculated results obtained with ANISN were compared with experimental data for the transmitted energy and angular distributions for 1-, 2.5-, 4-, 8- MeV electrons normally incident on aluminum slabs of various thicknesses and for 1-MeV electrons normally incident on a gold slab. The calculated and experimental results are in reasonably good agreement for the aluminum slabs but are in poor agreement for the gold slab.

Another development using the ANISN code to transport electrons was accomplished by Özdemir (13). He produced ANISN

cross sections which treat several elastic scatters as a single elastic scatter with broadened multiple-scattering angular distribution in the manner of ETRAN. This results in the necessity for a large number of spatial intervals being substantially relaxed from that of the Bartine, et al. work [54]. In Özdemir's work the inelastic electron-electron collisions are treated with a continuous slowing down model and angular deflection of both elastic and inelastic scattering are expressed by a Legendre polynomial series. No modification was necessary on the ANISN code. This makes it possible that the ANISN code, which is familiar to many potential users, be widely used for electron transport calculations.

The water phantom depth dose curve predicted by Özdemir's ANISN-CSDM (Continuous Slowing Down Model) was in good agreement with experimental data measured at the University of Oklahoma Health Sciences Center. However, a mathemetical inconsistency in Özdemir's treatment of frequency of elastic scattering was uncovered in the course of this work which alters the results somewhat. This will be improved and discussed in Chapters IV and V.

Özdemir's ANISN-CSDM can also be improved by considering the following features in electron transport calculations:

a). "Catastrophic" collisions. In an electron deep penetration problem, "catastrophic" collisions, in which the energy loss and deflection of electrons are very large, occur once in a while. These collisions play an important role in shaping the depth dose

curve. Considering their contributions separately requires extending the continuous-slowing-down model to a group-skipping model in the preparation of electron transport cross sections.

b). Delta Rays. No secondary particles were transported in the ANISN-CSDM. All secondary particles were assumed to deposit all their energies at the positions where they were generated. This assumption biases results to shorter range energy deposition because energetic secondary particles might penetrate further in the phantom and reshape the depth dose curve. Transporting the delta rays will also offer the information to determine the charge distribution in the phantom.

C. Monte Carlo Method [40,55]

As its name implies, the Monte Carlo method is equivalent to playing a game of chance. The Monte Carlo method is very simple in concept and offers the potential of precise, relatively assumption-free results.

In its simplest form, the Monte Carlo method is a mathematical analog of the physical processes that can occur. These processes (elastic Coulomb scattering, inelastic electron-electron collision, bremsstrahlung interaction) are randomly occuring events whose probabilities have been evaluated in terms of cross sections. The mathematical analog uses computer-generated random numbers to choose from probability data the specific interactions occurring to a single electron. This electron can be followed until it is lost or of negligible significance. Then, its contribution to any information of interest: fluxes, energy deposition, leakage, etc., can be tabulated. Many source electrons are

transported in the same manner. The average behavior of all these electrons offers the statistical data of interest.

In principle, the Monte Carlo method is capable of simulating completely all the processes that govern the behavior of electrons. Codes to perform such simulations are common for neutrons and gamma rays. In practice, however, this is not feasible due to the large number of Coulomb scatterings that take place as an electron moves in the transport medium. A single electron with an initial energy of 0.5 MeV will undergo in the neighborhood of 10^5 collisions in gold in the process of downscattering to 0.25 MeV. Therefore, individual electronic collisions are not treated in the Monte Carlo calculations. Instead, an alternative Monte Carlo technique was developed specifically for electrons. This alternative technique, which has been used successfully by the ETRAN [10] code, reduces the detailed simulation by utilizing theories describing various segments of the transport problem to group together large number of collisions.

The ETRAN code divides the electron tracks to be sampled into a large number of short segments. The changes of energy, direction and position in each segment are sampled from suitable interaction distributions. At the end of each short segment, the direction of motion of the electron is changed by a multiple scattering angular deflection that is sampled from the Goudsmit-Saunderson distribution. The spectrum resulting from energy loss is determined, in part, by the modified Landau energy-straggling distribution. An option is also provided for using

the continuous slowing down approximation in which all of the energy loss by collisions is simply computed with the use of the stopping power formula. Collisions involving large energy transfers can be considered separately from the continuous slowing down model, and secondary electrons and bremsstrahlung are produced and transported through the target material. The Monte Carlo calculation then proceeds through simulation segment by segment, rather than collision by collision, thus reducing the computing time considerably.

Berger [40] dealt in great detail with the application of the Monte Carlo method to the solution of electron transport problems. He proposed various models for constructing condensed particle histories, based on different approximations for the energy loss and different multiple-scattering theories. He found good agreement between his calculations of electron transmission through gold and aluminium foils and experimental measurements. Berger and Seltzer [56] subsequently presented the results of both the energy deposition and total electron flux at different depths in water irradiated by high energy electron beams. Energy-loss straggling and energy transport by bremsstrahlung were included in the calculations and their effects on depth-dose curves were shown. Nahum [12] developed a comparable Monte Carlo code and obtained some depth-dose curves which are very close to Berger's and Seltzer's results.

A comparison between the ETRAN-calculated and experimently measured depth dose curves is shown in Figure 3.1. It is readily

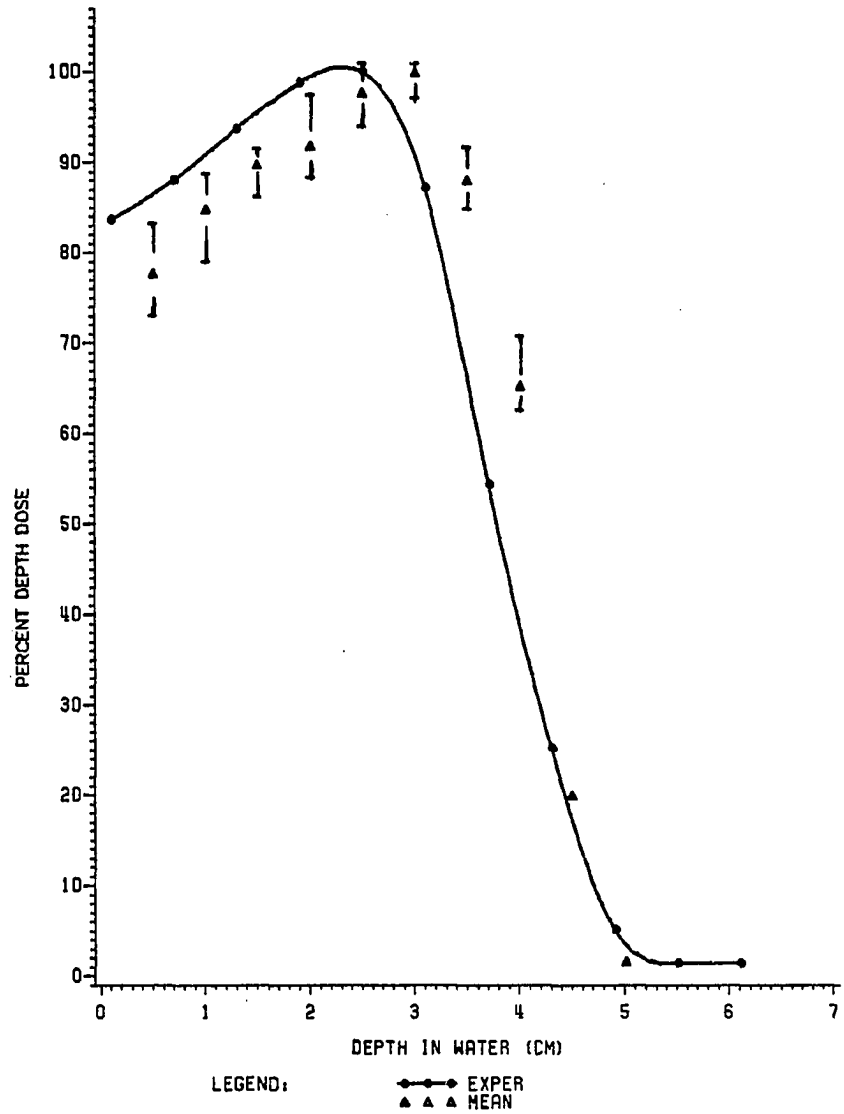

Figure 3.1. Normalized energy deposition in a water phantom irradiated with a 10 MeV electron beam. The measured data for a 8cm x 8cm beam area is shown by solid curve. The error bars indicate the range of results obtained in six ETRAN calculations in which both c-s-d-a and straggling were used. The triangles represent the mean of the six calculations. Each calculation simulated 1000 incident electrons.

observed that whereas the calculated and measured curves are quite similar at depths near the range of the incident beam, the curves are significantly different at lesser depths. That is, the energy deposition for shorter distances into phantom material is greater than that predicted by ETRAN for 10 MeV electron beams. This difference makes it questionable to utilize ETRAN predictions as a basis for administering radiation dosage to cancer patients.

A common limitation of ETRAN and Nahum's electron transport code lies in that they are capable of treating only a single dimensional geometry. This drawback can be removed by using a multi-dimensional Monte Carlo code. Just as ANISN code can be used to solve an electron transport problem providing the multigroup electron cross sections are available, Monte Carlo codes for neutral particles can also be utilized for electron transport calculations. The preparation of the electron transport cross sections will be discussed in Chapter IV. Then these cross-section data will be used in a discrete ordinates code, ANISN, and a Monte Carlo code, MORSE, to calculate information of interest.

CHAPTER IV

PREPARATION OF TRANSPORT CROSS-SECTION DATA

A. Introduction

Theoretically, the transport of neutral particles or charged particles from an initial energy and angular distribution to a final energy and angular spectrum can be calculated without a knowledge of the particle type and knowing only the probabilities of all interactions which can occur. This is the basis by which it is possible to use neutral particle transport computer codes for the study of an electron transport problem.

In this study, two neutral particle transport codes were tested for electron transport analysis. One is a discrete ordinates code, ANISN, the other is a Monte Carlo code, MORSE-E. Both codes use multigroup cross-section data. The energy dependence of the cross-sections is expressed in multigroup form. The angular dependence of the cross-sections is represented by Legendre polynomial expansions in the cosine of the scattering angle. The crucial task of employing these two codes for electron transport analysis is the preparation of a set of appropriate transport cross-section data.

Özdemir [13] developed an ANISN-CSDM (Continuous-Slowing-Down-Model) electron transport cross-section model with the

adaptation of the "condensed random walk" concept employed in the ETRAN code. In this method one representative elastic interaction replaces a large number of physical elastic interactions and the scattering angle of this representative electron is chosen from a broadened angular distribution. The characteristic of Özdemir's model lies in its simplicity of transporting an electron to the next lower energy group by one average inelastic scattering. One special feature of the ANISN-CSDM is its use of the equally probable effective elastic and inelastic collisions. The elastic part changes the angular direction of the electron and the inelastic part results in both energy and angular changes.

In the preparation of multigroup cross-section data, a logical extension of the continuous-slowing-down model is the group-skipping model developed in this study. In the continuous-slowing-down model, every inelastic collision of the electron loses the amount of energy necessary to reach the next lower energy group. In the group-skipping model, the inelastic collisions are allowed to skip beyond the next lower energy group. This group-skipping cross-section corresponds to the probability, per unit path length, of a "catastrophic" collision occuring during electron penetration. The continuous-slowing-down model assumes local deposition of the energy lost by the primary electron when it is inelastically collided. The group-skipping model, however, allows the energy lost by a catastrophically collided electron to be transferred to a secondary electron (delta ray) and then allows for further transport of the delta ray.

Described in this chapter is the preparation of the group-skipping model cross-sections used in the electron transport calculations presented in the following chapters.

B. Group Structure of the Group-Skipping Model

1. Inelastic Scattering of Electrons by Electrons

Møller [27] has derived a relativistic cross-section for electron scattering from free electrons at rest. If T is the incident kinetic energy in mc^2 units (0.511 MeV) and xT is the kinetic energy in mc^2 units of the lowest energy electron in the scattered pair, the cross-section may be stated as

$$\frac{d\sigma}{dx} = 2\pi r_o^2 \frac{(T+1)^2}{T^2(T+2)}\left(\frac{1}{x^2} - \frac{1}{x(1-x)} \cdot \frac{(2T+1)}{(T+1)^2} + \frac{1}{(1-x)^2} + \left(\frac{T}{T+1}\right)^2\right) \quad (4.1)$$

where

σ = cross-section per electron;

r_o = the classical electron radius;

x = fractional energy transfer.

Since the resultant electron with the highest kinetic energy is defined as the primary electron, the maximum fraction of energy transfer is 1/2. Therefore, the range of x is (0,1/2).

The angular distribution of the scattered electrons may be obtained from Eq. (4.1) and the energy-momentum conservation conditions. The angle of scattering θ_l of the lower energy electron (delta ray) is given by

$$\cos\theta_l = \left(x(T+2) \,/\, (xT+2)\right)^{1/2} , \quad (4.2)$$

and the angle of scattering θ_h of the higher energy electron with kinetic energy (1-x)T in mc^2 units is obtained from

$$\cos\theta_h = \left((1-x)(T+2) \,/\, ((1-x)T+2)\right)^{1/2} , \qquad (4.3)$$

where $\cos\theta_h \geq \cos\theta_\ell \geq 0$ since $0 \leq x \leq 1/2$.

Comparisons of Møller's cross-section with experiment are presented by Birkoff [30] and show good agreement. However, it should be noted that Møller's cross-section is applicable only if the energy transferred by the incident electron to the atomic electron is large enough so that the binding energy is insignificant and the atomic electron can be assumed to be free. When the energy transfer is of the order of the binding energy, Møller's cross-section does not apply, and the binding of the atomic electrons must be taken into account through the Bethe [26,33] theory of stopping power which predicts that for small x'

$$\int_0^{x'} x\frac{d\sigma}{dx}\,dx = \frac{C}{E}\left(\log\left(\frac{2E^2\, x'\,(T+2)}{I^2}\right) - \beta^2 \right), \qquad (4.4)$$

where $C = \dfrac{2\pi e^4}{mv^2}$;

E = kinetic energy of the incident electron;

I = mean ionization potential.

2. Formulation of the Energy Group Structure

When an electron penetrates through the transport medium, it will make numerous collisions that result in small energy losses and deflections, and a relatively small number of catastrophic collisions that cause it to lose a large fraction of its energy and turn through a large angle. In electron Monte Carlo calculations, Schneider and Cormack [56] applied a scheme which treats the catastrophic collisions separately by random sampling. In

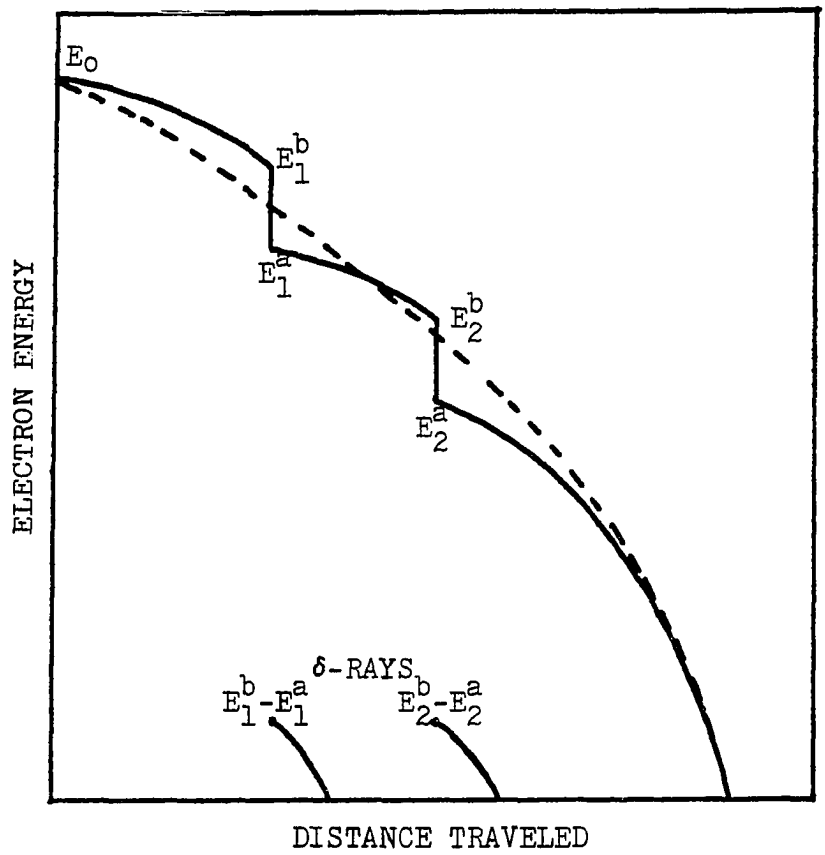

Figure 4.1. Energy-pathlength plot of a hypothetical electron case history. The solid curve corresponds to a Monte Carlo model with catastrophic collisions that lower the energy from E_1^b to E_1^a and from E_2^b to E_2^a and generates delta rays. The dotted curve corresponds to an equivalent continuous-slowing-down model. Adapted from Schneider and Cormack.

their model, the history of the electron is divided into sections, within which no catastrophic collisions occur and in which continuous-slowing-down is assumed. Each section is ended by a catastrophic collision. A pictorial representation of this scheme is illustrated by Figure 4.1, adapted from their paper. The catastrophic collisions lead to delta rays with energy transferred from the primary electrons. The history of the delta rays can be followed.

The fractional energy transfer of a catastrophic collision may fall in the range of a reasonably defined cut-off parameter, x_c, and the maximum possible value, 1/2. The characteristic of the group-skipping model developed in this study lies in that each catastrophically collided electron is assumed to lose a fixed fraction of its energy. This fixed fraction of energy transfer is the average value, $\bar{x}_{cat}$, of all possible fractional losses of the catastrophic collisions. In subsequent paragraphs, the average fractional energy transfer will be defined and used to construct the energy group structure of the group-skipping model.

Since the energy transfer for catastrophic collisions far exceeds the binding energy of atomic electrons, Møller's cross-section is applicable in the calculation of the average fractional energy transfer of a catastrophic collision, $\bar{x}_{cat}$. Therefore, the following definition may be used to determine $\bar{x}_{cat}$

$$\bar{x}_{cat} = \frac{\int_{xc}^{1/2} x \frac{d\sigma}{dx} dx}{\int_{xc}^{1/2} \frac{d\sigma}{dx} dx} , \qquad (4.5)$$

where

x = fractional energy transfer of a catastrophic collision;

x_c = cut-off parameter of the fractional energy loss of a catastrophic collision.

Substituting the Møller cross-section Eq. (4.1) into Eq. (4.5), the average fractional catastrophic energy transfer can be obtained

$$\bar{x}_{cat} = \frac{\left(\ell n\, x + \frac{1}{1-x} + \ell n(1-x) + \frac{2T+1}{(T+1)^2}\,\ell n(1-x) + \frac{1}{2}\left(\frac{T}{T+1}\right)^2 x^2\right)_{x_c}^{1/2}}{\left(-\frac{1}{x} + \frac{1}{1-x} + \left(\frac{T}{T+1}\right)^2 x + \frac{2T+1}{(T+1)^2}\ell n\left(\frac{1-x}{x}\right)\right)_{x_c}^{1/2}} \qquad (4.6)$$

Thus, for a given initial energy in units of mc^2, T, the average fractional catastrophic energy loss depends on x_c only. The choice of x_c is not arbitrary. An iterative method should be used to obtain a value of x_c such that it enables $\bar{x}_{cat}$ to fit a logarithmic spacing energy group structure. The logarithmic spacing, which has been adopted by DATAPAC6 [10] to produce data of interest, has the advantage that the distribution of angular deflections changes very slowly from step to step [40]. This group structure follows the rule of

$$E_{g+1} = k \cdot E_g \qquad (4.7)$$

where E_g represents the upper bound of energy group g, and k is an energy reduction factor. It is often expressed as

$$k = 2^{-1/m} \qquad (4.8)$$

where m is an integer such that after m groups the energy is reduced by half. In other words, $E_{g+m} = \frac{1}{2} \cdot E_g$.

With this knowledge of logarithmic spacing, it is easy to

construct a multigroup energy structure by setting

$$\bar{x}_{cat} = k^n \quad , \tag{4.9}$$

where n, an integer in the range of 2 and m-1, is the number of groups skipped.

For the case of 10 MeV electrons transported through a water phantom, the calculated values of the cut-off fractional energy transfer for various multigroup energy structure parameters m and n are listed in Table 4.1.

TABLE 4.1

Cut-off Catastrophic Fractional Energy Transfers, x_c, for Various Group Structures.

(Electron initial energy = 10 MeV, Medium: Water)

m \ n	2	3	4	5	6	7
4	0.1687	0.3218	—	—	—	—
5	0.1202	0.2247	0.3570	—	—	—
6	0.0919	0.1687	0.2661	0.3807	—	—
7	0.0737	0.1336	0.2080	0.2975	0.3978	—
8	0.0611	0.1092	0.1687	0.2398	0.3218	0.4107

A large value of m will produce a fine group structure but will need more computer storage space. An increase of the value of n, which is the number of energy groups skipped in a catastrophic collision, will increase the cut-off catastrophic fractional energy transfer thus decreasing the number of catastrophic collisions. Once this catastrophic collision occurs it will produce an energetic delta ray. In the extreme case of a large

m together with a small n, the group-skipping model will produce depth dose data very close to those predicted by the continuous-slowing-down model. This is due to the fact that the delta rays generated under this extreme case of the group-skipping model are of low energy and cannot be transported further from their generating sites, and the energy lost by electron in a down-scattering interaction of the continuous-slowing-down model is deposited at the collision site. The results of the group-skipping model reported in this study are based upon the group structures that produce the optimized results.

The multigroup energy structure of the electron transport group-skipping model has been constructed on the basis of average fractional catastrophic energy transfer. This is the characteristic of the group-skipping model that uses a fixed fractional catastrophic energy transfer for all catastrophic collisions. Similarly, it is appropriate to use a fixed average fraction of electron energy loss to represent all possible fractions of "moderate" energy transfers. This average fractional moderate energy transfer, $\bar{x}_{mod}$, may be defined as

$$\bar{x}_{mod} = \frac{\int_{x_1}^{x_c} x \frac{d\sigma}{dx} dx}{\int_{x_1}^{x_c} \frac{d\sigma}{dx} dx} , \qquad (4.10)$$

where x_1 is a cut-off value of fractional energy transfer for moderate inelastic collisions. The other variables and constants in Eq. (4.10) are the same as previously defined.

The value of x_1 can be determined by equating $\bar{x}_{mod}$ to k,

the fractional energy transfer from the original energy group to the next lower group. Thus each moderate collision results in an energy loss which places an electron in the next lower energy group.

Those electron interactions with fractional energy transfers less than the lower limit of moderate fractional energy transfer are grouped into the in-group scatterings. The removal of these small energy losses from the average energy transfer calculations results in loss of energy deposition. This neglect of small energy loss in energy conservation analysis can be compensated by a slight modification of the moderate collision cross-section which will be discussed in Section C of this chapter.

Based upon the above introduction, the group-skipping model developed in this study may be represented by Figures 4.2, 4.3 and 4.4. Figure 4.2 shows the average catastrophic fractional energy loss that replaces all other catastrophic fractional energy transfers. Both energy scale and the corresponding fractional energy transfer scale are shown. The average moderate collision which represents all possible moderate energy loss collisions is shown in Figure 4.3. The multigroup energy structure of a group-skipping model is shown in Figure 4.4. For energy group g, E_g, E_{g+1} and E(g) are its upper bound, lower bound and mean energy, respectively.

It could be very clearly seen from Fig. 4.4 that in a limiting case of the group-skipping model with x_c having a value of 1/2, the catastrophic and moderate energy transfers are

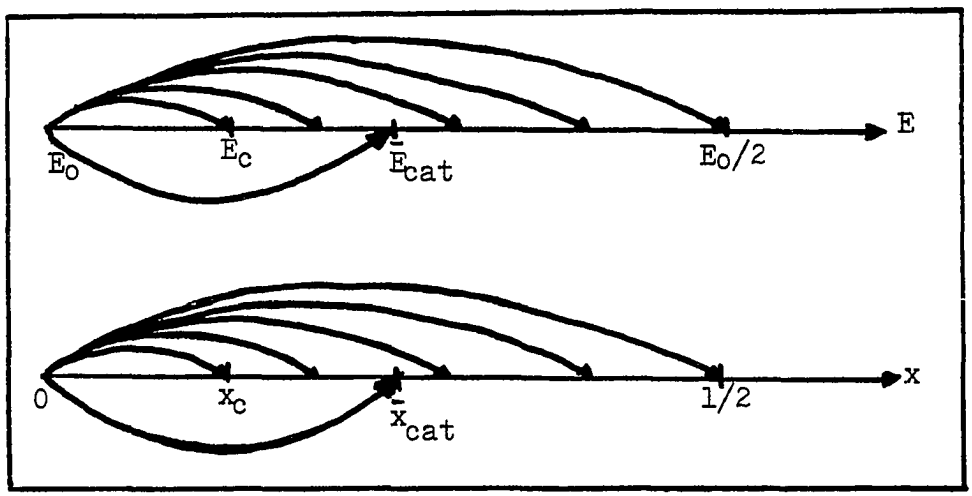

Figure 4.2. Average catastrophic fractional energy transfer.

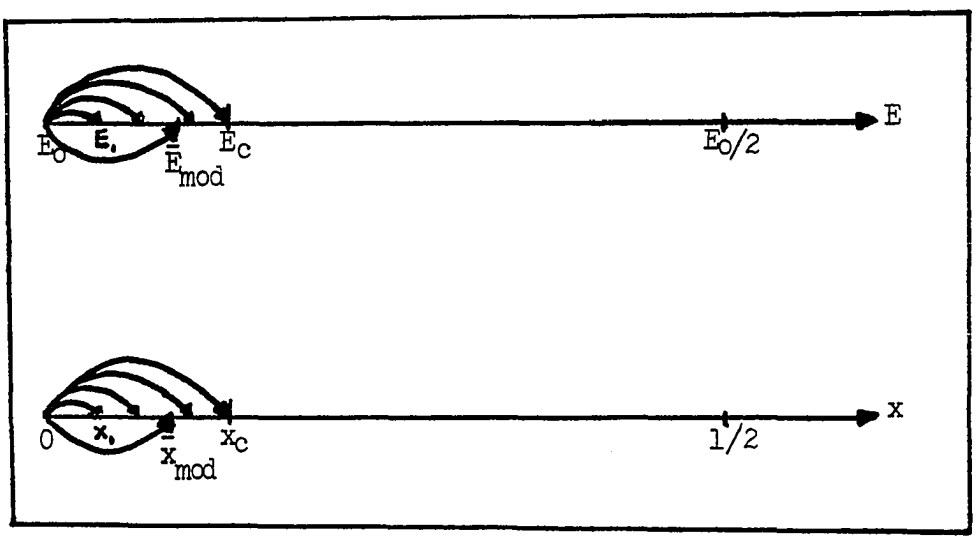

Figure 4.3. Average moderate fractional energy transfer.

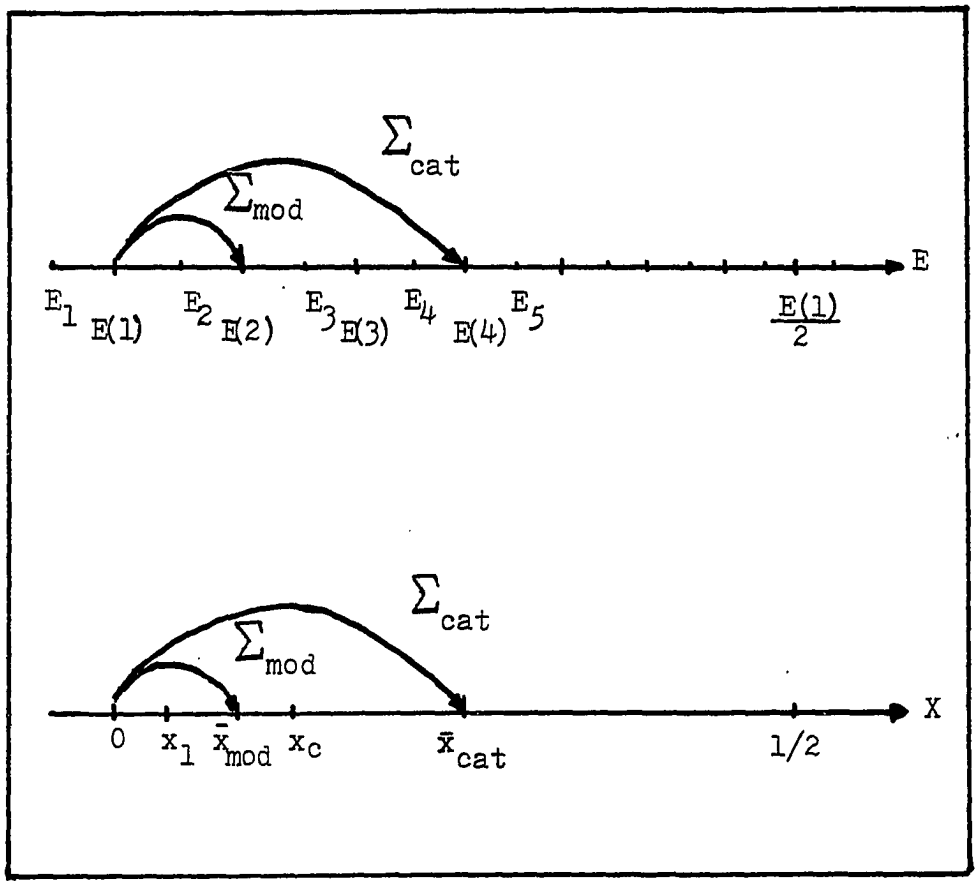

Figure 4.4. Multigroup structure of the group-skipping model.

collapsed into a single energy transfer. Therefore, the continuous-slowing-down model developed by Özdemir is a limiting case of the group-skipping model.

C. Production of Macroscopic Cross-Sections

To employ computer codes ANISN and MORSE-E for electron transport calculations, it is necessary to define the appropriate multigroup macroscopic cross-sections for the group structure constructed in section B. Described in this section are the physical cross-sections that govern the probabilities of in-group scatterings, moderate energy transfer collisions to the next lower energy group, catastrophic group-skipping collisions and absorption interactions. The angular distribution of scattered electrons is represented by the expansion of cross-sections in Legendre polynomials and is discussed in section D of this chapter.

1. Catastrophic Collision Cross-Section

As discussed earlier, the group-skipping model uses a fixed catastrophic fractional energy transfer to replace all other possible catastrophic fractional energy losses. Therefore, when an electron in group g has a catastrophic collision it suffers an energy loss of $\Delta E_{cat}(g)$ which can be expressed as

$$\Delta E_{cat}(g) = E(g) - E(g+n) , \qquad (4.11)$$

where E(g) is the mean energy of group g, n is the number of groups skipped by a catastrophic collision in the group-skipping model.

To determine the magnitude of a catastrophic collision cross section, the concept of "catastrophic collision stopping power" must be introduced. This stopping power is the mean

energy loss per unit path length resulting from catastrophic collisions. For an electron in energy group g, the catastrophic collision stopping power can be defined as

$$S_{cat}(g) = NZ \int_{x_c}^{1/2} E(g) \times \frac{d\sigma}{dx} \, dx \quad , \tag{4.12}$$

where $\frac{d\sigma}{dx}$ is the inelastic Møller cross-section given by Eq. (4.1). Since all constants in Eq. (4.12) are known, the catastrophic collision stopping power can be easily calculated.

The macroscopic catastrophic collision cross-section, which is the probability, per unit path length, of a catastrophic collision, can be obtained by

$$\Sigma_{cat}(g) = \frac{S_{cat}(g)}{\Delta E_{cat}(g)} \quad , \tag{4.13}$$

It should be noted that since n is the number of groups skipped in a catastrophic collision and IGM is the final group number, the catastrophic collision cross-section for group beyond IGM-n should be set to zero. Therefore, the catastrophic collision cross-section can be written as

$$\Sigma_{cat}(g) = \frac{S_{cat}(g)}{\Delta E_{cat}(g)} \qquad \text{for } g \leqq \text{IGM-n}$$

$$\Sigma_{cat}(g) = 0 \qquad \text{for IGM-n} < g \leqq \text{IGM} \quad .$$

2. Moderate Collision Cross-Section

In principle, the moderate collision cross-section may be defined by the same procedure used to define the aforementioned catastrophic collision cross-section. That is,

(1). define the moderate collision stopping power by

$$S_{mod}(g) = NZ \int_{x_1}^{x_c} E(g) \, x \, \frac{d\sigma}{dx} \, dx \ , \text{ and} \qquad (4.14)$$

(2). equate the moderate collision cross-section to the ratio of $S_{mod}(g)$ and $\Delta E_{mod}(g)$, which is the energy difference between $E(g)$ and $E(g+1)$.

With this procedure, however, the energy transfer by inelastic collisions with fractional energy loss less than x_1 and by bremsstrahlung are excluded from the energy loss mechanisms of the group-skipping model. With a view to preserving the correct total stopping power in the group-skipping model, the moderate collision cross-section is obtained by

$$\Sigma_{mod}(g) = \frac{S_{tot}(g) - S_{cat}(g)}{E(g) - E(g+1)} \ , \qquad (4.15)$$

where $S_{tot}(g)$ is the total stopping power for electrons with energy $E(g)$. The total stopping power is available from the calculations of DATAPAC6 [10] which is an auxiliary routine of the ETRAN code.

The moderate collision cross-section defined by Eq. (4.15) can also be called the "non-catastrophic inelastic collision" cross-section. Now, the total stopping power of the group-skipping model is equal to the sum of stopping powers of catastrophic, moderate and in-group scattering, or

$$\Sigma_{cat}(g).(E(g)-E(g+n)) + \Sigma_{mod}(g).(E(g)-E(g+1)) + \Sigma_{ing}(g).(E(g)-E(g))$$
$$= S_{cat}(g) + (S_{tot}(g) - S_{cat}(g)) + 0$$
$$= S_{tot}(g) \ .$$

Therefore the total stopping power employed by the group-skipping model is identical with the actual total stopping power. Then λ_{mod} is the moderate collision mean-free-path, the inverse of Σ_{mod}. It is the mean distance traveled by an electron in losing the amount of energy other than that accounted for by catastrophic collisions. We account for this "moderate" energy loss in a single collision in distance λ_{mod}. This "moderate" energy loss is also the difference between the mean energy of one group and the mean energy of the next lower group, so that one such collision results in an electron being slowed into the next lower group.

3. In-Group Scattering Cross-Section

The in-group scattering cross-section in this model is the probability, per unit path length, of an elastic scattering. Since no energy loss is suffered by the electron in an in-group elastic scattering, the in-group scattering cross-section is a measure only of the angular redistribution due to elastic collisions. This angle change is described by the Legendre expansion coefficients for multiple scattering available in DATAPAC6 routines.

The DATAPAC6 routines divide each electron track into many "steps". The step size is chosen so that each step reduces the electron energy from its current group to the next group. Each step is subdivided into ISUB equal "short steps". The DATAPAC6 expansion coefficients for multiple elastic scattering are based upon one scatter per "short step", so that

$$\Sigma_{\text{Datapac}}(g) = \frac{1}{\Delta y\,(g)} \qquad (4.16)$$

where $\Sigma_{Datapac}$ (g) is the equivalent DATAPAC6 cross-section for energy group g, and $\Delta y(g)$ is the length of "short step" for group g.

In order to produce one in-group scatter per "short step", there must be ISUB number of scatters per step, since the length of a step is equivalent to ISUB number of in-group scattering mean-free-paths. Thus,

$$\Sigma_{ing} (g) = \frac{1}{\Delta y (g)} = \frac{ISUB}{\Delta Y(g)} \qquad (4.17)$$

where $\Delta Y(g)$ is the length of a step for energy group g.

Meanwhile, in the definition of the moderate collision cross-section, we have required that there be one moderate collision per step, thus

$$\Sigma_{mod}(g) = \frac{1}{\Delta Y (g)} \quad . \qquad (4.18)$$

The in-group scattering cross-section in our model may be obtained as

$$\Sigma_{ing} (g) = ISUB \cdot \Sigma_{mod}(g) \quad . \qquad (4.19)$$

4. Absorption Cross-Section

Since electrons are scattered but not absorbed by the transport medium, it is reasonable to define the electron absorption cross-section to be zero for all but the final energy group. A non-zero absorption cross-section for the last energy group is appropriate and necessary in order to stop following low energy electrons which cannot transport away from the immediate neighborhood of their originating locations. Hence, the absorption

cross-section may be represented by

$$\Sigma_a(g) = 0 \qquad \text{for } g = 1,2,\ldots\ldots\ , \text{IGM-1.}$$

and $\Sigma_a(\text{IGM}) = \Sigma_{tot}(\text{IGM}) - \Sigma_{ing}(\text{IGM})$.

where $\Sigma_{tot}(\text{IGM})$ is the total cross section of the final energy group.

All electrons that have been deenergized to the final energy group in the transport medium are assumed to deposit all of their remaining energy. The magnitude of $\Sigma_{tot}(\text{IGM})$ can be set much larger than that of $\Sigma_{ing}(\text{IGM})$, so no computer time is wasted to transport electrons of the final energy group.

5. Total Cross-Section

It is the characteristic of the group-skipping model that all elastic and inelastic collisions are represented by the in-group scattering, moderate collision and catastrophic collision cross-sections. The rest of the group-to-group scattering cross-sections are all zero. Therefore, the total cross-section of energy group g may be obtained from

$$\Sigma_{tot}(g) = \Sigma_{ing}(g) + \Sigma_{mod}(g) + \Sigma_{cat}(g) + \Sigma_a(g) \ . \qquad (4.20)$$

6. Energy Absorption Cross-Section

The macroscopic energy absorption cross-section, which is called activity cross-section in ANISN and response function in MORSE, provides the results of electron energy deposition in the following way:

$$R = \sum_{g=1}^{IGM} \phi(g) \cdot \Sigma_{act}(g) \qquad , \qquad (4.21)$$

where R = energy deposition per unit volume per unit time;

$\phi(g)$ = electron flux of energy group g, calculated by ANISN or MORSE;

$\Sigma_{act}(g)$ = activity (energy absorption) cross-section of group g.

It may be seen that in the group-skipping model the electron energy deposition per unit path length is equal to the difference between total stopping power and catastrophic stopping power. This is due to the fact that a catastrophic collision produces a delta ray which does not deposit its energy at its generating place. Thus, it is obvious that the macroscopic energy absorption cross-section is given as

$$\Sigma_{act}(g) = S_{tot}(g) - S_{cat}(g) \quad , \tag{4.22}$$

where $S_{tot}(g)$ and $S_{cat}(g)$ are the total and catastrophic stopping power, respectively. It should be noted that for energy groups beyond IGM-n the catastrophic stopping powers are equal to zero, that is

$$\Sigma_{act}(g) = S_{tot}(g) \quad , \qquad \text{for IGM-n} \lesssim g \leqq \text{IGM} \quad .$$

When an electron reaches the final energy group in the transport medium, the group-skipping model terminates its history by introducing a relatively large particle absorption cross-section which was discussed earlier in this section. Thus, the energy absorption cross-section for the final group should also be defined in such a way that an electron of the final energy group deposits all its remaining energy. The activity cross-section for the last group may be given as

$$\Sigma_{act}(\text{IGM}) = \Sigma_{a}(\text{IGM}) \cdot E(\text{IGM}) \quad , \tag{4.23}$$

where E(IGM) is the mean energy of the final group.

D. Angular Distribution Model

Theoretically, anisotropic scattering cross-section may be expanded in terms of the scattering angle cosine $\mu = \vec{\Omega} \cdot \vec{\Omega}'$ as

$$\Sigma_s(\vec{r}, E' \to E, \mu) = \sum_{\ell=0}^{\infty} \left(\frac{2\ell+1}{4\pi}\right) \Sigma_{s,\ell}(\vec{r}, E' \to E)\, P_\ell(\mu), \quad (4.24)$$

where $P_\ell(\mu)$ is the Legendre polynomial of order ℓ and

$\Sigma_{s,\ell}(\vec{r}, E' \to E)$ is the ℓ^{th} expansion coefficient which may be obtained by

$$\Sigma_{s,\ell}(\vec{r}, E' \to E) = 2\pi \int_{-1}^{1} d\mu \Sigma_s(\vec{r}, E' \to E, \mu)\, P_\ell(\mu). \quad (4.25)$$

Thus, the multigroup anisotropic scattering cross-sections of the group-skipping model may be expanded by

$$\Sigma_{ing}(g,\mu) = \sum_{\ell=0}^{\infty} \left(\frac{2\ell+1}{4\pi}\right) \Sigma_{ing}(g,\ell) \cdot P_\ell(\mu), \quad (4.26)$$

$$\Sigma_{mod}(g,\mu) = \sum_{\ell=0}^{\infty} \left(\frac{2\ell+1}{4\pi}\right) \Sigma_{mod}(g,\ell) \cdot P_\ell(\mu), \quad (4.27)$$

and

$$\Sigma_{cat}(g,\mu) = \sum_{\ell=0}^{\infty} \left(\frac{2\ell+1}{4\pi}\right) \Sigma_{cat}(g,\ell) \cdot P_\ell(\mu), \quad (4.28)$$

where $\left(\frac{2\ell+1}{4\pi}\right)\Sigma_{ing}(g,\ell)$, $\left(\frac{2\ell+1}{4\pi}\right)\Sigma_{mod}(g,\ell)$, $\left(\frac{2\ell+1}{4\pi}\right)\Sigma_{cat}(g,\ell)$ are the in-group scattering, moderate collision and catastrophic collision ℓ^{th} order expansion coefficients for energy group g, respectively. The zeroth order of these expansion coefficients are the macroscopic scattering cross-sections defined in section C. The higher order of the expansion coefficients are corrections for anisotropy of scattering.

An absolutely forward distribution requires an infinite number of terms in the Legendre polynomials expansion. Thus

strongly forward scattering can require large computer storage space and running time. Such a problem does not exist in the group-skipping model, since those very low energy transfer scatterings that generate the extremely forward collision are not retained in the calculations of the group-skipping model. Therefore, the anisotropic scattering cross-sections may be approximated with a finite appropriate expansion order, LMAX.

The order of Legendre expansions required for in-group scattering can be reduced by the extended transport correction [13,53,54]. The order of Legendre coefficients for the catastrophic collisions is less than that for the moderate collisions since the latter is more forwardly distributed. Therefore, the order of Legendre expansions required for the group-skipping model is determined by the moderate collisions. For moderate collisions, a cut-off value of fractional energy transfer, x_1, is defined to exclude those extremely low energy transfer collisions. Both the moderate collision cut-off, which reduces the order for moderate collision cross-section, and the extended transport correction, which reduces the order for in-group scattering cross-section, approximate strongly forward collisions by allowing the electron to continue forward without colliding. For the group-skipping model, the required order of Legendre coefficients, LMAX, is limited by x_1.

In this section, the angular expansion coefficients for in-group scattering, moderate collision and catastrophic collision cross-sections are defined so that a complete set of

multigroup cross-section data is available for the group-skipping electron transport model.

The angular expansion coefficients of the macroscopic in-group scattering cross-sections can be produced by the DATAPAC6 code. As discussed earlier, at the end of each "short step" the distribution of the direction of motion can be determined from the multiple scattering coefficients, $H(g,\ell)$, which were calculated from the Goudsmit and Saunderson theory in DATAPAC6. The normalized expansion coefficients of the in-group scattering cross-section, $\Sigma_{ing}(g,\ell)$ are obtained from the multiple scattering coefficients by the relationship

$$\frac{\Sigma_{ing}(g,\ell)}{\Sigma_{ing}(g,0)} = H(g,\ell) \quad , \tag{4.29}$$

for $g = 1, 2, \ldots\ldots, IGM$

$\ell = 0, 1, \ldots\ldots, LMAX$.

where $\Sigma_{ing}(g,0)$ is the in-group scattering cross-section for group g as defined in the model.

The normalized Legendre expansion coefficients for catastrophic collision of the group g may be defined as follows:

$$Y(g,\ell) = \frac{2\pi NZ}{C_{cat}(g,0)} \int_{\mu(x_c)}^{\mu(1/2)} \frac{d\sigma}{d\mu} \cdot P_\ell(\mu)\, d\mu \tag{4.30}$$

where $\mu(1/2)$ and $\mu(x_c)$ are the cosine of the scattering angles at the fractional energy losses of 1/2 and x_c , respectively. Their values are determined by Eq. (4.3).

The angular-dependent differential inelastic cross-section $d\sigma/d\mu$ can be derived from equations (4.1) and (4.3) and expressed as

$$\frac{d\sigma}{d\mu} = -8\pi r_o^2 \left(\frac{T+1}{T}\right)^2 \left(\left(\frac{1}{(T+2)(1-\mu^2)} \right)^2 - \frac{1}{2\mu^2(1-\mu^2)} \cdot \frac{2T+1}{(T+2)(T+1)^2} + \left(\frac{1}{2\mu^2}\right)^2 + \left(\frac{T}{T+1}\right)^2 \cdot \frac{1}{(T+2-T\mu^2)^2} \right) \cdot \mu \qquad (4.33)$$

In Eq. (4.30), $C_{cat}(g,0)$ is the physical catastrophic collision cross-section of energy group g, $\Sigma_{cat}(g)$. This may also be called the first unnormalized expansion coefficient of group g. It should be noted that

$$Y(g,0) = 1, \qquad (4.34)$$

in analogy with $H(g,0)$.

The normalized Legendre expansion coefficients for moderate collisions of group g may be defined in a similar way to those of catastrophic collisions and presented by

$$V(g,\ell) = \frac{2\pi NZ}{C_{mod}(g,0)} \int_{\mu(x_1)}^{\mu(x_c)} \frac{d\sigma}{d\mu} P_\ell(\mu)\, d\mu \qquad (4.35)$$

where $\mu(x_1) = \left(\frac{(1-x_1)(T+2)}{(1-x_1)T+2} \right)^{1/2}$,

$C_{mod}(g,0)$ = the physical moderate collision cross-section of group g, $\Sigma_{mod}(g)$.

It is obvious that, like $H(g,0)$ and $Y(g,0)$, $V(g,0) = 1$.

There is an approximation inherent in the group-skipping model in the treatment of angular distribution. Since $\Sigma_{mod}(g)$

includes some small-collision (below cut off) and Bremsstrahlung energy loss, Eq. (4.35) gives these collisions the same angular distribution as the slowing-down collisions.

In summary of the above discussions, the matrix of multi-group scattering cross-section for the group-skipping model may be represented in the following well-known ANISN forms:

(1) in-group scattering cross-section

$$(2\ell+1) \cdot H(g, \ell) \cdot \Sigma_{ing}(g)$$

(2) moderate collision cross-section

$$(2\ell+1) \cdot V(g, \ell) \cdot \Sigma_{mod}(g)$$

(3) catastrophic collision cross-section

$$(2\ell+1) \cdot Y(g, \ell) \cdot \Sigma_{cat}(g)$$

where $g = 1, 2, \ldots\ldots\ldots, IGM$

$\ell = 0, 1, 2, \ldots\ldots, LMAX$.

CHAPTER V

COMPARISONS AND DISCUSSION

In this chapter, the electron transport cross-sections of the group-skipping model developed in Chapter IV will be tested with two neutral particle transport codes: ANISN and MORSE-E. The calculated results from the group-skipping model and the continuous-slowing-down model are presented, along with the experimeatally measured data. For additional comparison, the calculational results from the Monte Carlo electron transport code ETRAN18G, where available in appropriate form, are also presented. The cases chosen for comparison are generally those for which experimental results are available. Many of these cases were also used by Özdemir for testing his ANISN-CSDM model. Özdemir's comparisons were repeated and reported here with some difference in results, due to inconsistencies discovered in Özdemir's use of the model.

A. 10 MeV Electrons Incident on a Water Phantom

The experimental data presented here are taken from the measurements by Anderson [7] at the University of Oklahoma Health Sciences Center. The measurements were performed using a Sagittaire clinical linear accelerator with a scanning electron beam operating at 10 MeV for various field areas.

1. One Dimensional Irradiation Geometry

The calculated results presented in this subsection are obtained with one dimensional irradiation geometry. The 10 MeV monoenergetic electron point beam is normally incident on the water slab which is of finite thickness in the z-axis and is infinite along the x- and y-axes. The energy deposition are computed over a layer perpendicular to the incident beam direction and of infinite laternal extent. This is also the geometry used by other investigators [12, 13, 57]. In practice, this geometry would correspond to an infinite plane detector. Therefore, no particle leakage is observable from the sides.

Alternatively, this geometry model can be interpreted as that of an infinitely broad, parallel beam incident on the water phantom with a small detector. The latter corresponds approximately to the practical situation in which the experimental data were measured. Normally, the beam is slightly diverging, but has a considerably larger beam area than the detectors placed along the central axis. This model reversal, however, requires that the radius of the beam field to be greater than the maximum range of the incident electrons. The validity of this model reversal has been tested by comparison with the two dimensional geometry calculations presented in the next subsection.

The total energy depositions, as a function of the penetration depth in a water phantom, predicted by various codes using continuous-slowing-down models, are given in Figure 5.1. The solid histograms in Fig. 5.1 represent the Monte Carlo calculations

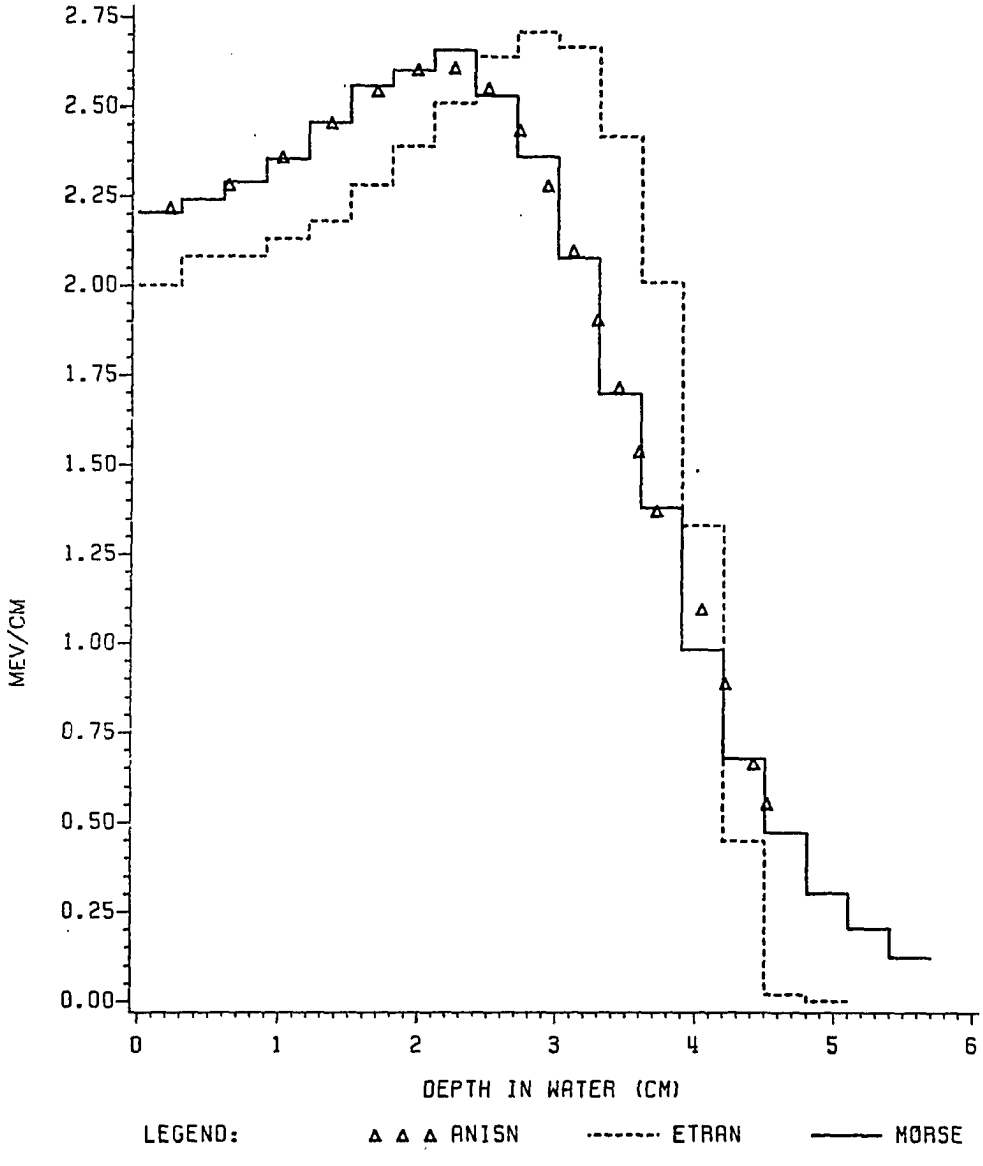

Figure 5.1. Total unnormalized energy deposition in a water phantom irradiated with a 10 MeV electron beam. (Continuous slowing down model is used in all calculations.)

by following 2500 electron histories using the MORSE-E code with the multigroup cross-section data developed by Özdemir for use with ANISN. The triangles plotted in the figure show the results from the discrete ordinates ANISN calculations using the same cross-section data. The dashed histograms represent the Monte Carlo ETRAN results of transporting 2500 electrons whose energy losses are determined by the continuous-slowing-down approximation. The electron transport cross-section data used in ANISN and MORSE-E has 34 energy groups, 44th order of Legendre expansions and a 48th order of angular quadrature.

While the ANISN-CSDM results are almost indistinguishable from the MORSE-E calculations in Figure 5.1, they are significantly different from the ETRAN18G predictions. Similar ETRAN results have been reported by Berger and Seltzer [57]. Compared to the ANISN-CSDM or MORSE-E results, the ETRAN18G prediction of the depth dose distribution has a lower surface dose, deeper position of the maximum dose, and a sharper fall-off after the peak. The reason for these differences will be discussed later in this subsection.

These calculated results are compared with experimental results in Figure 5.2. This figure shows the normalized depth dose distributions calculated by ANISN-CSDM, MORSE-E and ETRAN18G, together with the experimentally measured data by Anderson. The solid curve represents the measured data from a 15 cm x 15 cm field, which has a beam radius larger than the range of 10 MeV incident electrons. The calculated results are obtained by

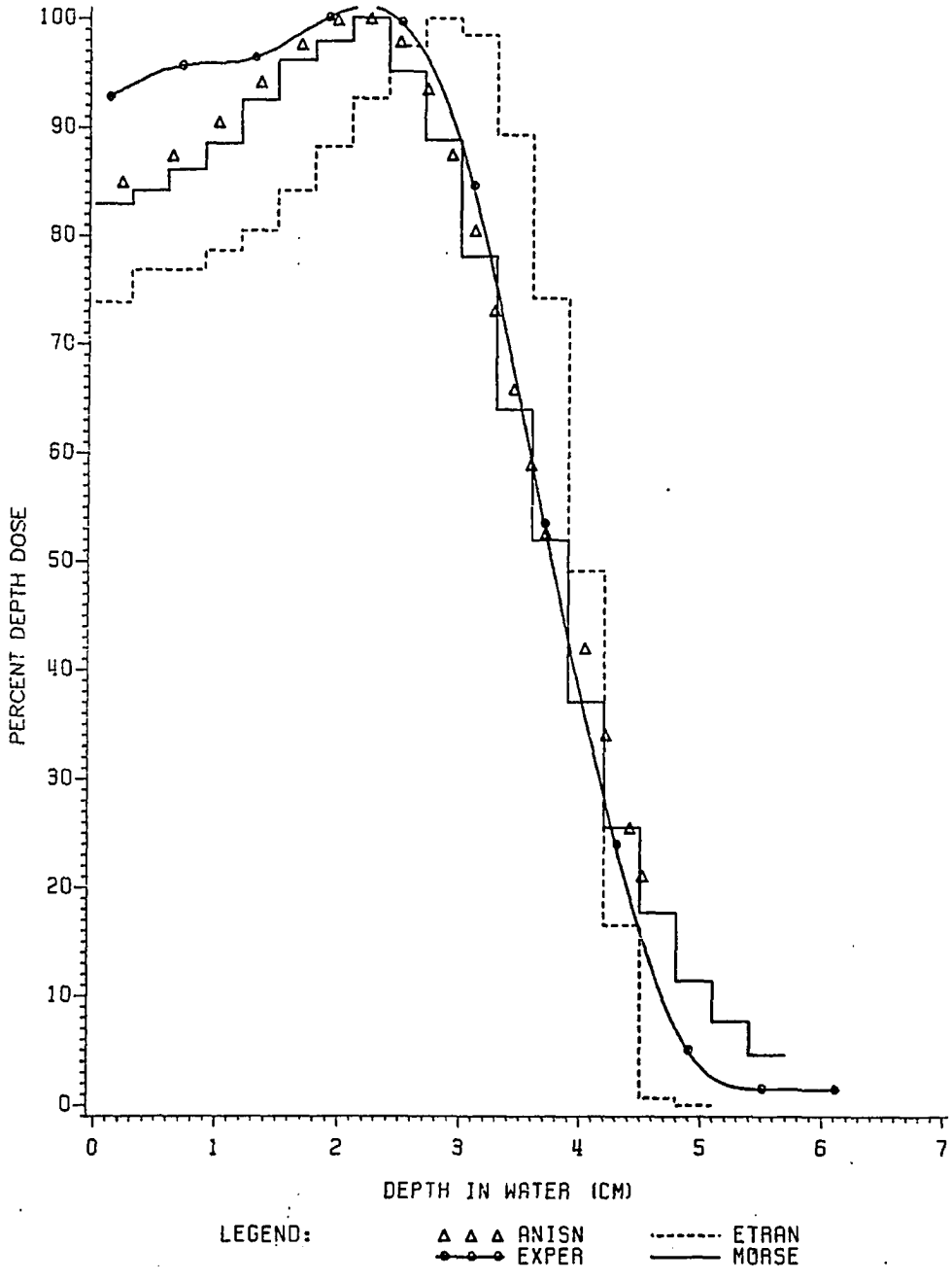

Figure 5.2. Normalized energy deposition in a water phantom irradiated with a 10 MeV electron beam. (Continuous slowing down model is used in all calculations.)

normalizing each curve in Figure 5.1 to 100 at its peak. This is necessary since absolute dose is not available in the measured values. The solid histograms, dashed histograms and triangles plotted in Figure 5.2 are normalized energy deposition distributions calculated by using MORSE-E, ETRAN18G, and ANISN, respectively.

For the case of 10 MeV electron incident on water, it is observed from Fig. 5.2 that the ANISN and MORSE-E results agree well with the experimental data in the central region of the depth dose distribution. The ANISN-CSDM results have a surface dose to maximum dose ratio of 83%, while the measured ratio is about 92%. The MORSE-E calculations show a higher dose beyond the electron range than that of the measured data. The ETRAN-CSDA calculations, when compared to the experimental data, display a much lower surface dose to peak dose ratio, 74%, a more prominent peak at a greater depth, and a faster dose fall-off beyond the peak. It is also noted in Fig. 5.2 that the experimentally measured dose at depth beyond the incident electron range falls within those predicted by MORSE-E and ETRAN18G.

The effect of energy-loss straggling on the results of energy deposition distribution can be studied in Figures 5.3, 5.4 and 5.5. The total depth dose distributions calculated by ANISN, MORSE-E, and ETRAN are plotted in Figure 5.3. ANISN and MORSE-E use the group-skipping model for electron transport cross-sections developed in this study as an extension of Özdemir's continuous-slowing-down model. The ETRAN energy-straggling option was used in which catastrophic collisions are sampled from a distribution

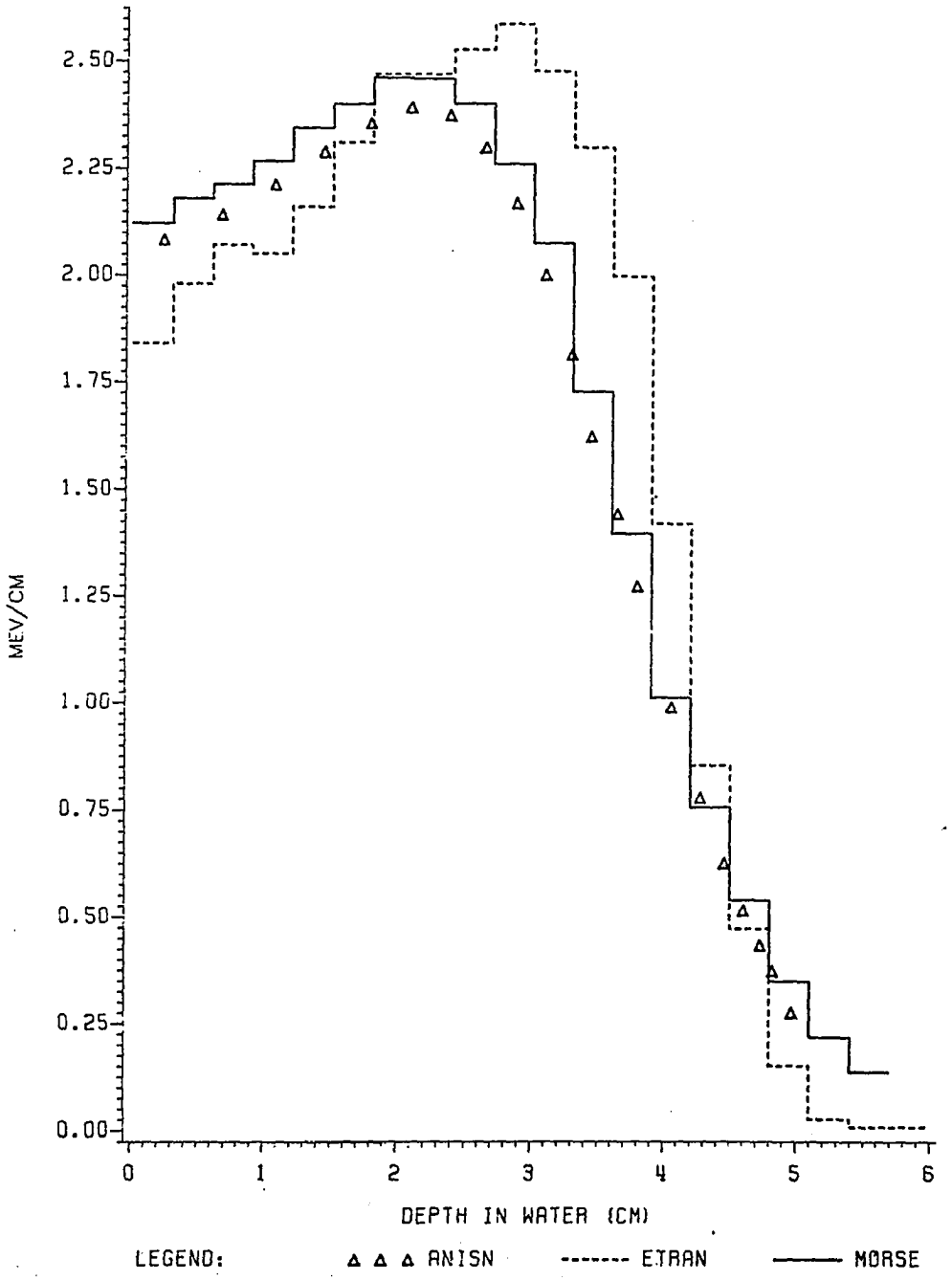

Figure 5.3. Total unnormalized energy deposition in a water phantom irradiated with a 10 MeV electron beam. (Energy loss straggling model or group-skipping model is used in calculations.)

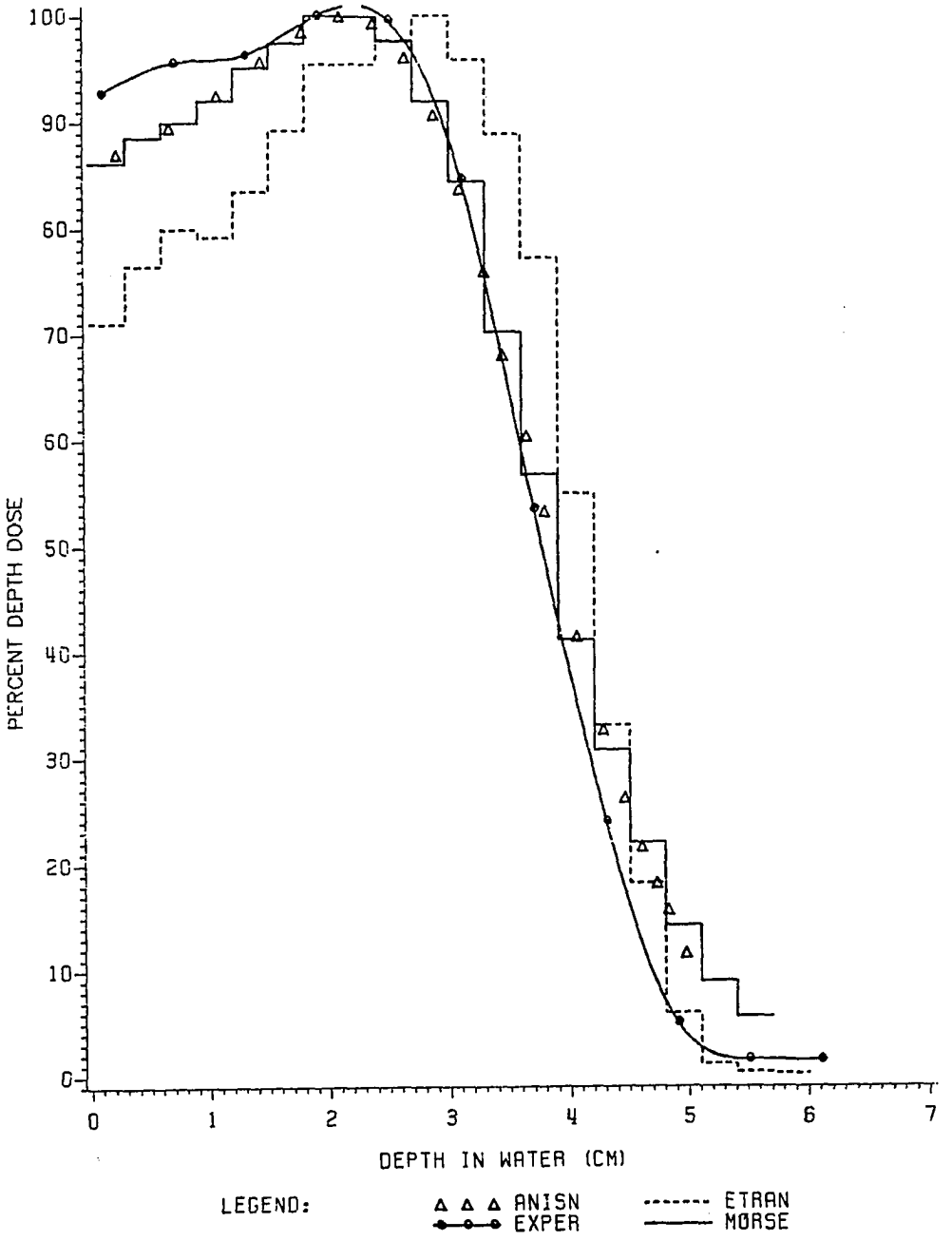

Figure 5.4. Normalized energy deposition in a water phantom irradiated with a 10 MeV electron beam. (Energy loss straggling model or group-skipping model is used in calculations.)

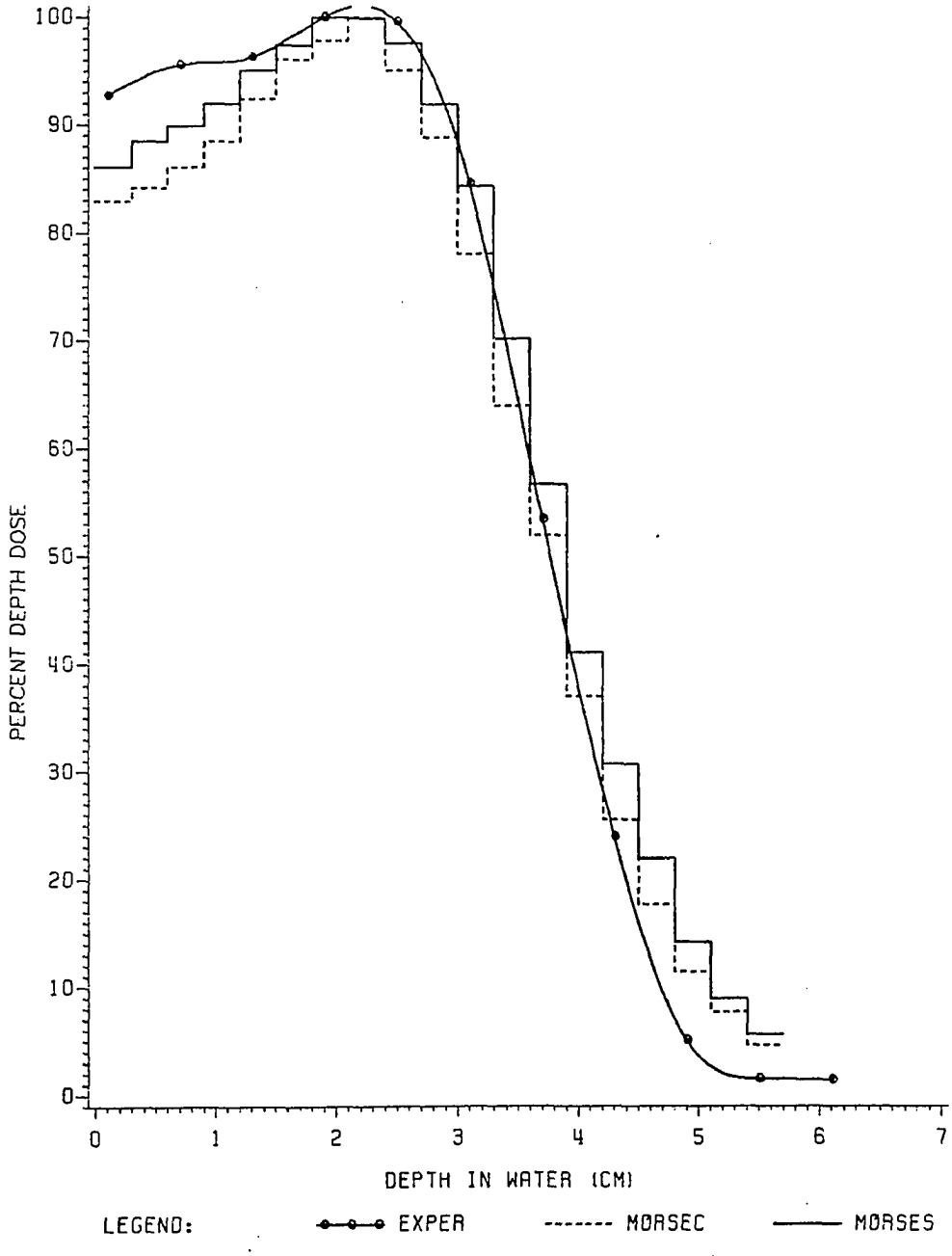

Figure 5.5. Normalized energy deposition in a water phantom irradiated with a 10 MeV electron beam. (Results from c-s-d-a and group-skipping model are compared to measured data.)

and small energy-loss collisions use the continuous-slowing-down approximation. As in previous figures, the MORSE-E results are represented in solid histogram form, the ETRAN values are shown by dashed histogram, and the ANISN predictions are plotted in triangles. The group structure parameters used to obtained the results on Fig. 5.3 are m = 7 and n = 3, where m is the number of groups required to reduce the electron energy by half, and n is the number of groups skipped by a catastrophically collided electron. The ETRAN results are obtained by use of energy-loss straggling resulting from collisions with atomic electrons and from bremsstrahlung events and by following secondary particles. Both ETRAN and MORSE-E calculations represent the Monte Carlo simulation of 2500 randomly generated electron histories. The cross-section data used in ANISN and MORSE-E have 34 energy groups, and a 48 quadrature order. An expansion order greater than 29 is necessary for converged results, and a P-order of 44 is used in the calculations. In Fig. 5.3, while the ANISN and MORSE-E calculated results agree very well, they differ from the ETRAN values significantly. Berger and Seltzer [57] have published similar ETRAN results. As expected, the inclusion of energy-loss straggling or group-skipping adds a straggling tail to the depth dose distributions at large depths and leads to a compensating decrease of energy deposition at small depths. In Fig. 5.3, the ETRAN results have a lower surface dose, greater depth of the maximum dose and a quicker fall-off after the peak in comparison with the ANISN or MORSE-E predictions. As in the earlier comparison

with experimental data, the experimental energy deposition data for water at 10 MeV is available only in a normalized form. Therefore, each energy deposition distribution in Fig. 5.3 is normalized to 100 at its peak and plotted in Figure 5.4 together with the experimentally measured values.

The solid curve in Fig. 5.4 is measured values from a 15 cm x 15 cm field which has a radius large enough to satisfy the condition for model reversal used in the calculations. It can be seen from Fig. 5.4 that the MORSE-E results (solid histogram) and ANISN values (triangles) agree very well with the measured data except at the surface and at depths comparable with the range. The ETRAN results (dashed histogram) show a considerably lower surface dose to peak dose ratio and a greater depth of peak dose than the measured data. ETRAN results appear to agree relatively well with measured values at greatest depths, however.

Before going into the discussions of the previous figures, a comparison of using the group-skipping model and the continuous-slowing-down model on the depth dose distribution in water is shown in Figure 5.5. The solid curve is the measured data for a 15 cm x 15 cm field. The dashed histogram, taken from the MORSE-E results on Fig. 5.2, represents the Monte Carlo simulation of electron transport by MORSE-E code using the continuous-slowing-down model cross-section data developed by Özdemir. The solid histogram, adapted from the MORSE-E results on Fig. 5.4, corresponds to the Monte Carlo technique of electron transport by MORSE-E code employing the group-skipping model cross-section data

originated in this work. Both the continuous-slowing-down model and the group-skipping model predict the same maximum dose position as that of the measured peak. Both models agree well but not perfectly with the measured data on the fall-off rate beyond the peak. The group-skipping model in general, broadens the peak slightly from that predicted by the continuous-slowing-down model. This appears to be in better agreement with experimental results in the region of the maximum dose. The apparently better agreement of the group-skipping model over the continuous-slowing-down model comes from the more accurate representation of the probabilistic energy losses of the primary electrons. As discussed in Chapter IV, the use of the continuous-slowing-down model requires that each inelastic collision of the electron lose the amount of energy necessary to reach the next lower energy group, while the use of the group-skipping model allows the inelastically collided electron to skip beyond the next lower energy group. The group-skipping cross-section corresponds to the probability, per unit path length, of a catastrophic collision. While the continuous-slowing-down model deposits all the energy lost by the inelastically collided electron at the collision position, the group-skipping model, however, permits the energy lost by a catastrophically collided electron be transferred to a secondary electron (delta-ray) and then transports the delta-ray. This refining by the group-skipping model cross-section data offers an improved simulation of electron transport and thus provides improved agreement with the measured depth dose distribution.

Since lower energy particles deposit their energy in material in a shorter distance, the differences for small depths observed in Fig. 5.5 imply that the measured beam may be contaminated by electrons with energies less than 10 MeV or by other radiations. The contamination might come from the scattered radiation from the electron beam-defining equipment attached to the SAGITTAIRE clinical linear accelerator. The trimmers are relatively near the dose material and are exposed to direct beam radiation. Hence, it is reasonable to expect that they could contribute to the dose received at the center-line detector. The collimator assembly (lead) placed early in the beam is struck by a much larger electron density than the trimmers. Some small-angle scattering from the collimators may also reach the center-line detector. Preliminary analyses of the details of these beam-defining equipment indicate that up to 5% of the electron beam is "contaminating" radiation produced by scattering with trimmers and collimators. According to the ICRU Report 21 [8], the actual absorbed dose at the surface of a water equivalent medium usually is about 85% of the maximum in the absence of contamination of the beam. Therefore, the 86% predicted by MORSE-E using the group-skipping model cross-section data may be very good agreement with the measured values when the contamination of the beam is eliminated.

As an electron beam penetrates the transport medium, it changes direction and loses energy through interactions with matter, degrading the original electrons to lower energies. In addition, the range of energy spectrum widens and the angular redistribution broadens as the beam penetrates to greater depths. The gross

differences displayed on Figure 5.1 for continuous-slowing-down models and on Figure 5.3 for energy-loss straggling models used in ETRAN and neutral particle codes should be traced to the differences in anqular spread or energy spectra predicted by ETPAN and the neutral particle codes. Figures 5.6 and 5.7 show the electron angular distribution at 1 cm and 2 cm depth, respectively. These are the depths prior to the peak where substantial differences of depth dose distribution are noticed. The angular distribution calculated from ANISN-CSDM (triangles), ANISN-Group-Skipping (solid curve), ETRAN-CSDA(starts), and ETRAN-Straggling (dashed histogram) are all plotted for comparison. In general, the ANISN results are in good but not perfect agreement with those calculated from ETRAN. The ANISN results have slightly smaller angular half-width than the ETRAN's. The significant differences shown on Figures 5.1 and 5.3 are unlikely come from such small differences in angular distribution.

Figures 5.8 and 5.9 show the energy spectra of the transmitted electrons in water at depths of 1 cm and 2 cm, respectively. As in the previous angular distribution figures, the ANISN-CSDM results are shown in triangles, the ETRAN-CSDA values are plotted in stars, the ANISN group-skipping calculations are represented by a solid line, and the ETRAN-straggling predictions are exhibited by a dashed histogram. As expected, the ETRAN-CSDA results show a narrower and sharper peak than those calculated by the rest. In the ETRAN-CSDA electron transport calculation any spatial displacement of electrons in the medium must degrade the

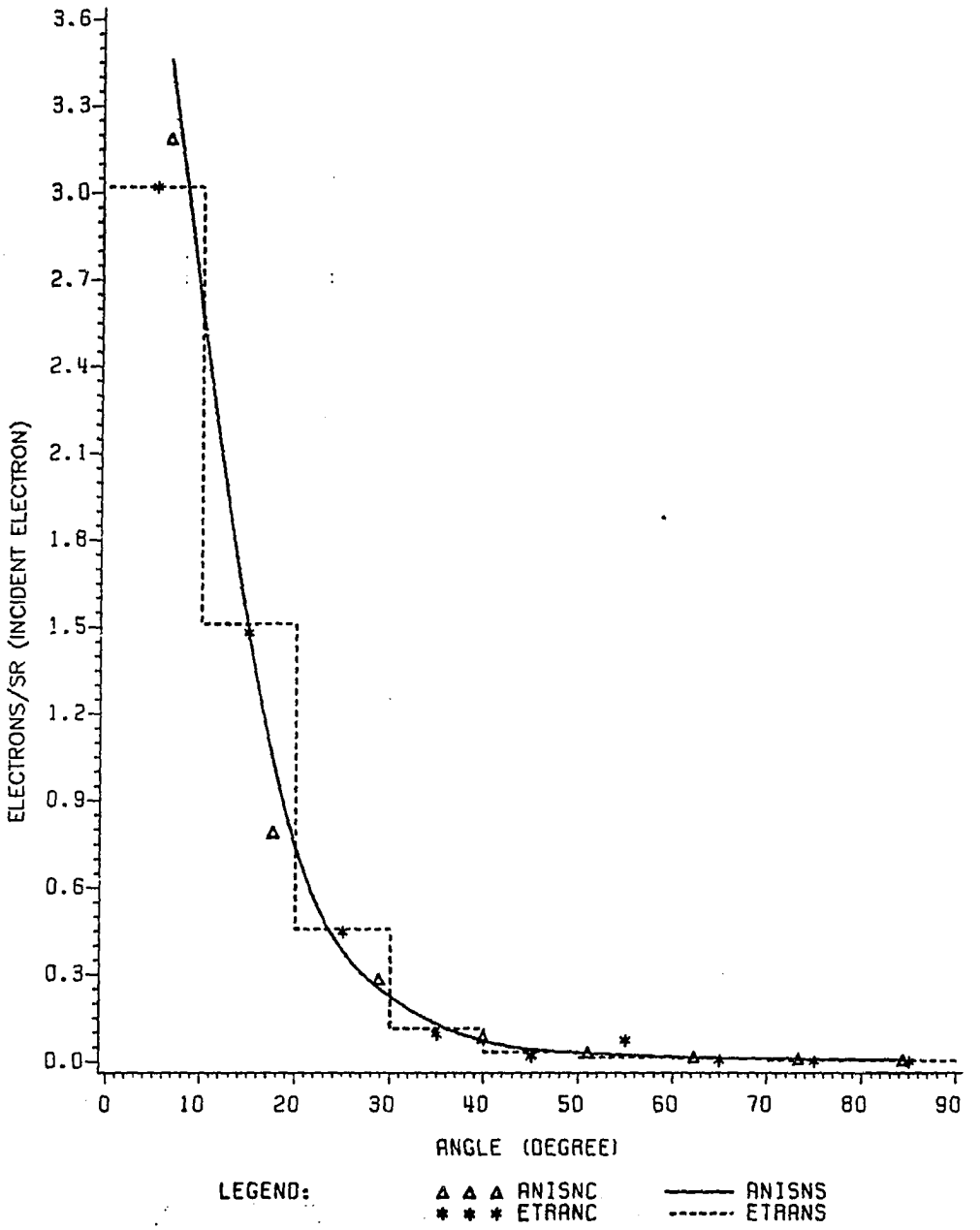

Figure 5.6. Angular distribution of the transmitted electron current for 10-MeV electrons normally incident on a water slab with 1 cm thickness.

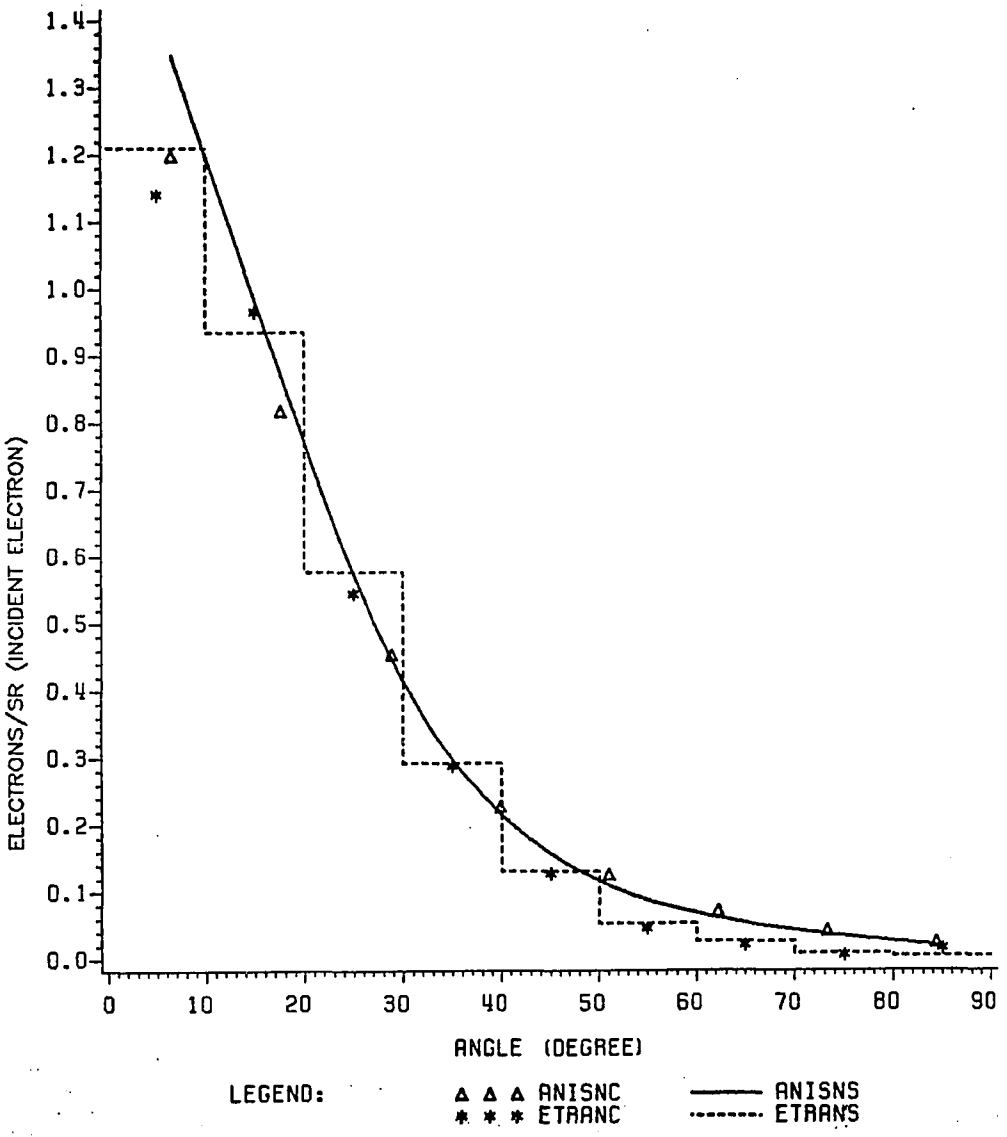

Figure 5.7. Angular distribution of the transmitted electron current for 10-MeV electrons normally incident on a water slab with 2 cm thickness.

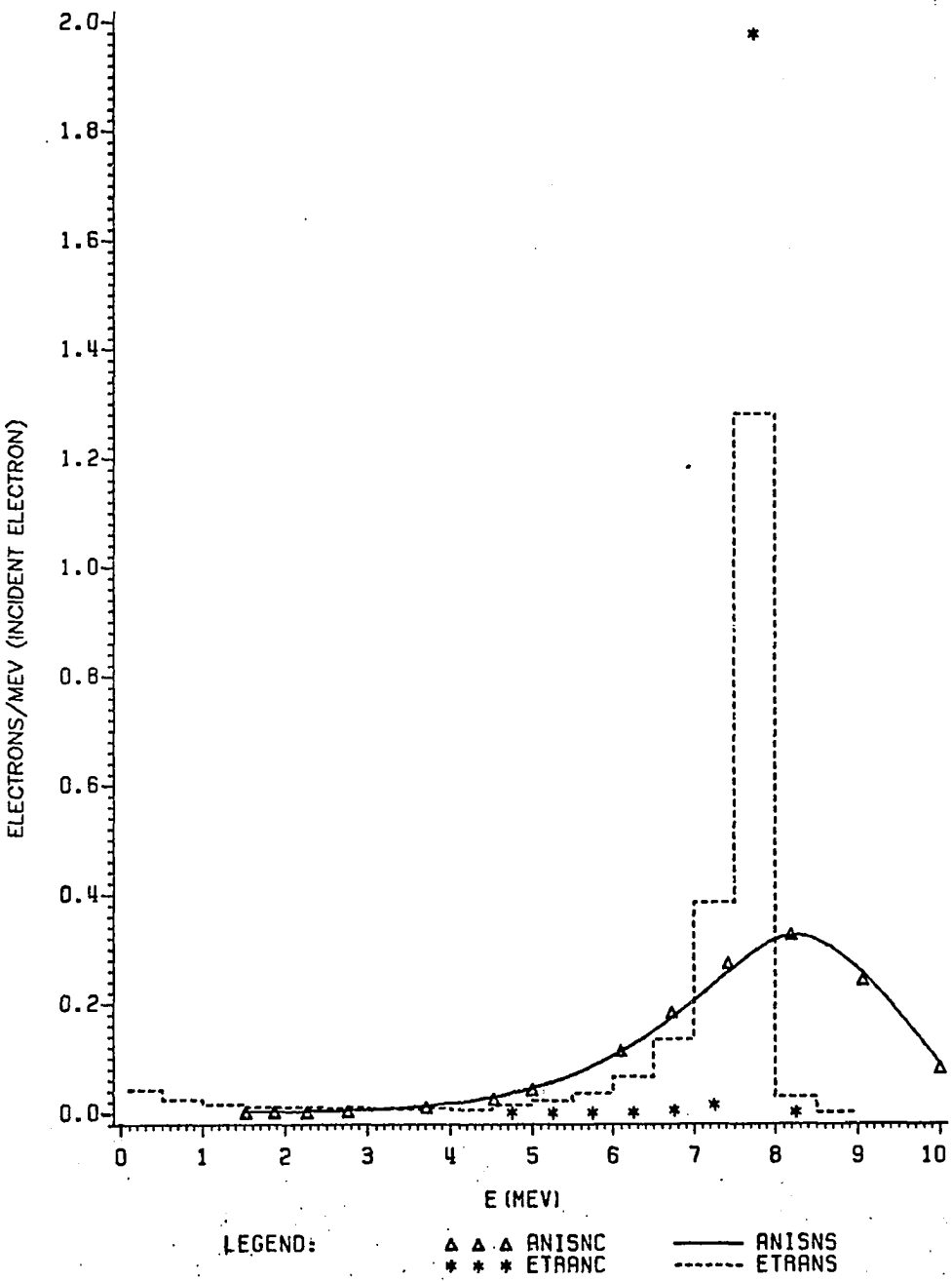

Figure 5.8. Transmitted electron current per unit energy per incident electron for 10-MeV electrons normally incident on a water slab with 1 cm thickness.

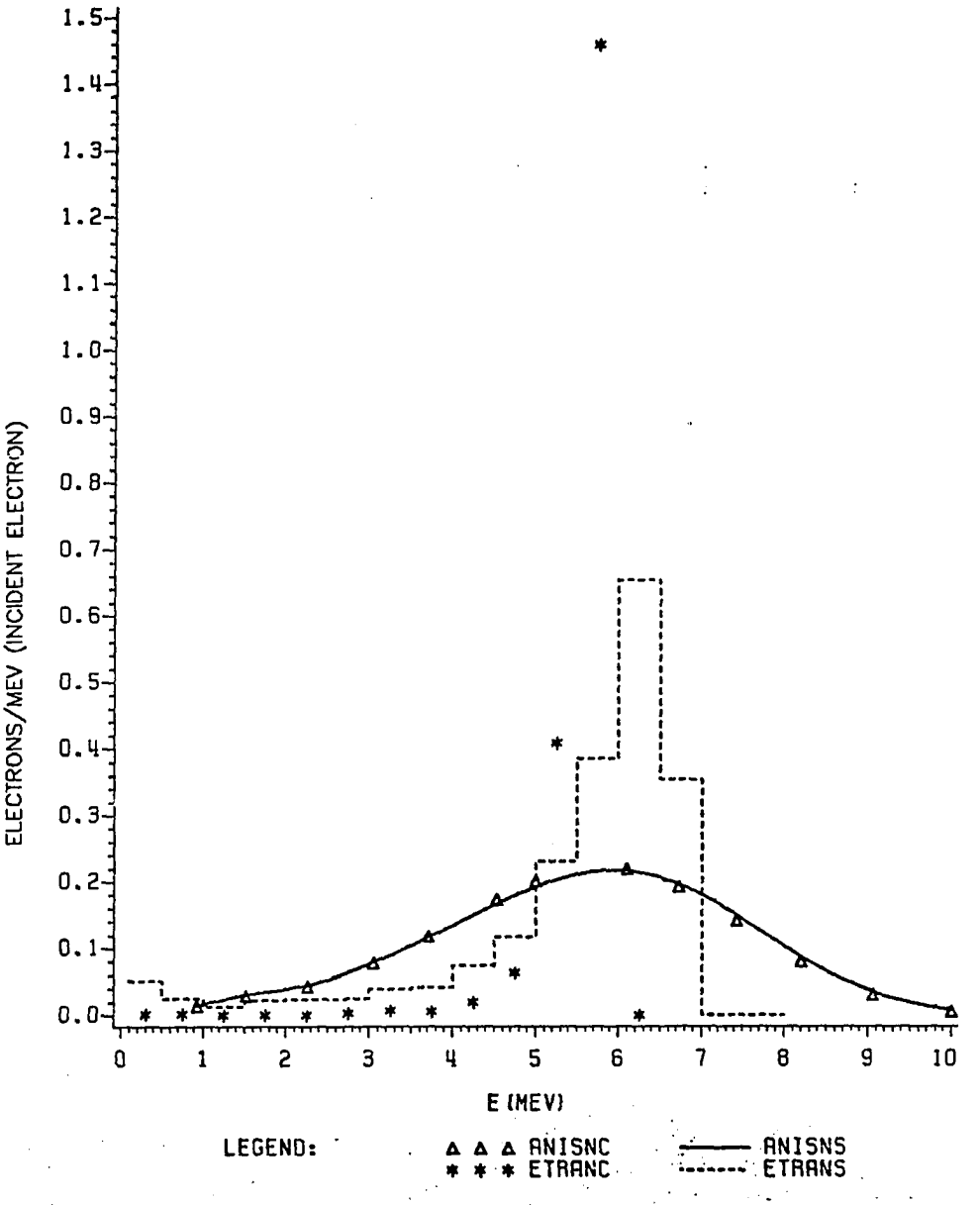

Figure 5.9. Transmitted electron current per unit energy per incident electron for 10-MeV electrons normally incident on a water slab with 2 cm thickness.

electrons to a lower energy predicted by the stopping power. This deterministic energy loss model results in the -function shape of the energy spectra of transmitted electrons and a clear range in the depth dose distribution. The ETRAN-straggling results also show a narrower peak even compared to the ANISN-CSDM values. This is because of ETRAN-straggling model uses a partially deterministic energy loss model which is basically similar to the continuous-slowing-down approrimation. As discussed in Chapter IV, the electron history is divided into sections in the ETRAN energy-loss straggling model. Each section is ended by a catastrophic collision. Within each section no catastrophic collisions occur and continuous-slowing-down is assumed. Since the magnitude of the catastrophic collisions at the end of each section is sampled from a distribution, it produces energy straggling. The inclusion of energy-loss straggling widens the transmitted electron energy spectra of continuous-slowing-down model. It also adds a straggling tail to the energy deposition distribution at large depths and causes a compensating decrease of dose deposition at small depths, therefore, further reduces the surface dose to maximum dose ratio. From Figures 5.8 and 5.9 it is observed that the ANISN-CSDM and group-skipping model show much wider energy spectra of transmitted electrons than their ETRAN counterparts. The major reason for this difference lie in that the ANISN code employs a probabilistic energy loss model between energy degradation steps. The probability of group-to-group energy transfer is governed by the cross-section data. In other words, the ANISN-CSDM and group-skipping model do not require an energy loss in each spatial interval, but

allows moderate or catastrophic energy loss according to the probability of a moderate inelastic collision or a catastrophic collision.

The depth dose distributions shown in Fig. 5.1 and Fig. 5.3 are related to the energy spectra widths displayed in Figures 5.8 and 5.9. Using a deterministic energy loss model which results in relatively narrow energy spectra at depth, the ETRAN calculations have a sharp fall-off in dose beyond the peak and a definite range. On the other hand, the ANISN code, using a probabilistic energy loss model which results in wide distribution at depth, has a more gradual fall-off in dose beyond the peak.. The broad and flat dose maximum predicted by ANISN code can also be identified with the broad energy spectra at depth since the energy loss straggling effects would be enlarged. The better agreement of ANISN results to the measured data implies that the probabilistic energy loss model is closer to reality than the deterministic energy loss model of ETRAN.

In the group-skipping model developed by this study, energy loss from primary and secondary electrons (delta rays) is treated explicitly, but the energy loss by bremsstrahlung is treated approximately. This approximation does not influence the results of depth dose distribution in the energy range of interest in this study. Figures 5.10A and 5.10B show the breakdown of the total energy deposition in a water phantom irradiated with electron beam of 10 MeV and 20 MeV, respectively, as calculated by ETRAN18G using the energy-loss straggling model. The solid curve is the total energy deposition which is the sum of

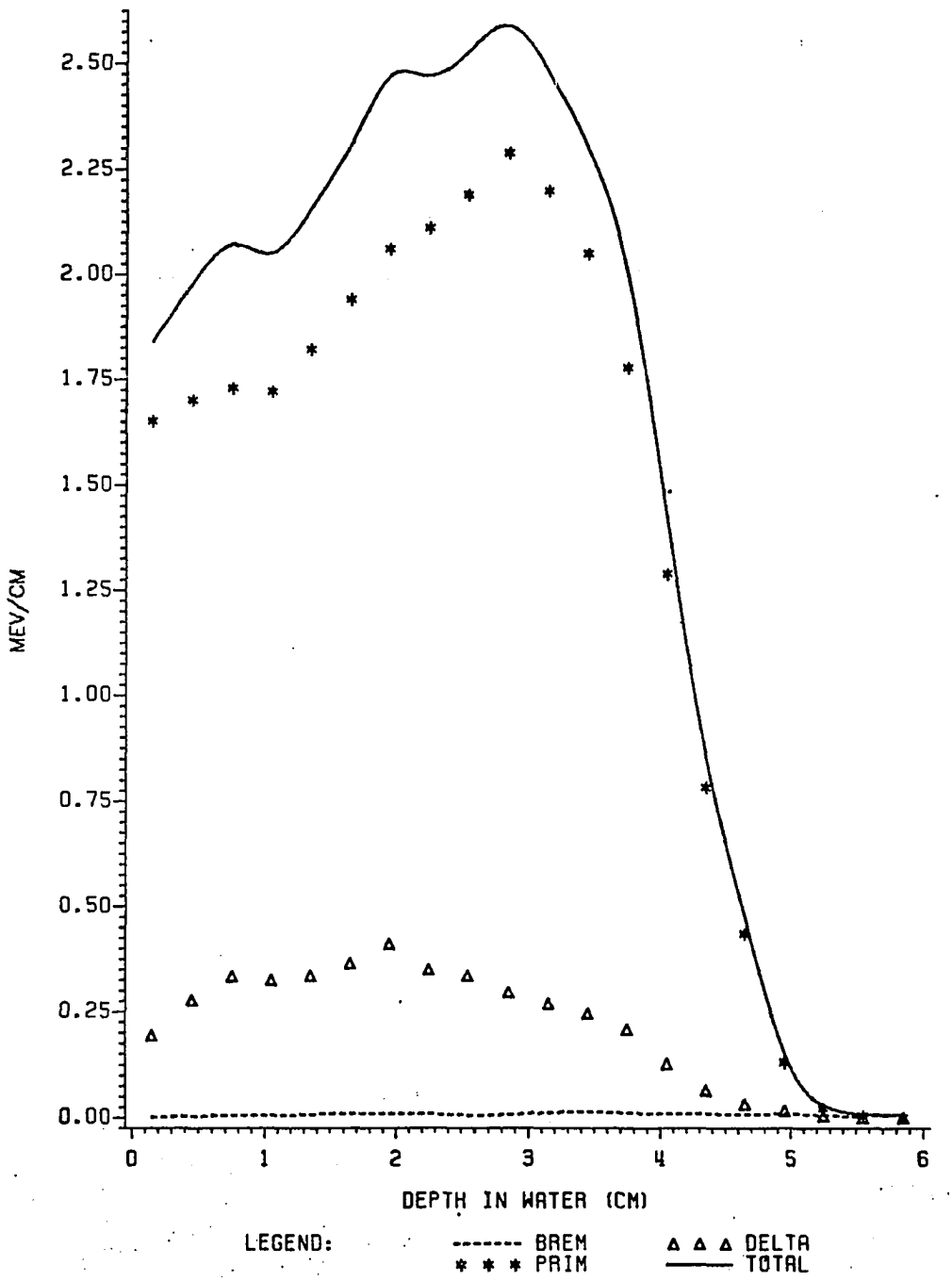

Figure 5.10A. Breakdown of the total energy deposition in a water phantom irradiated with a 10 MeV electron beam.

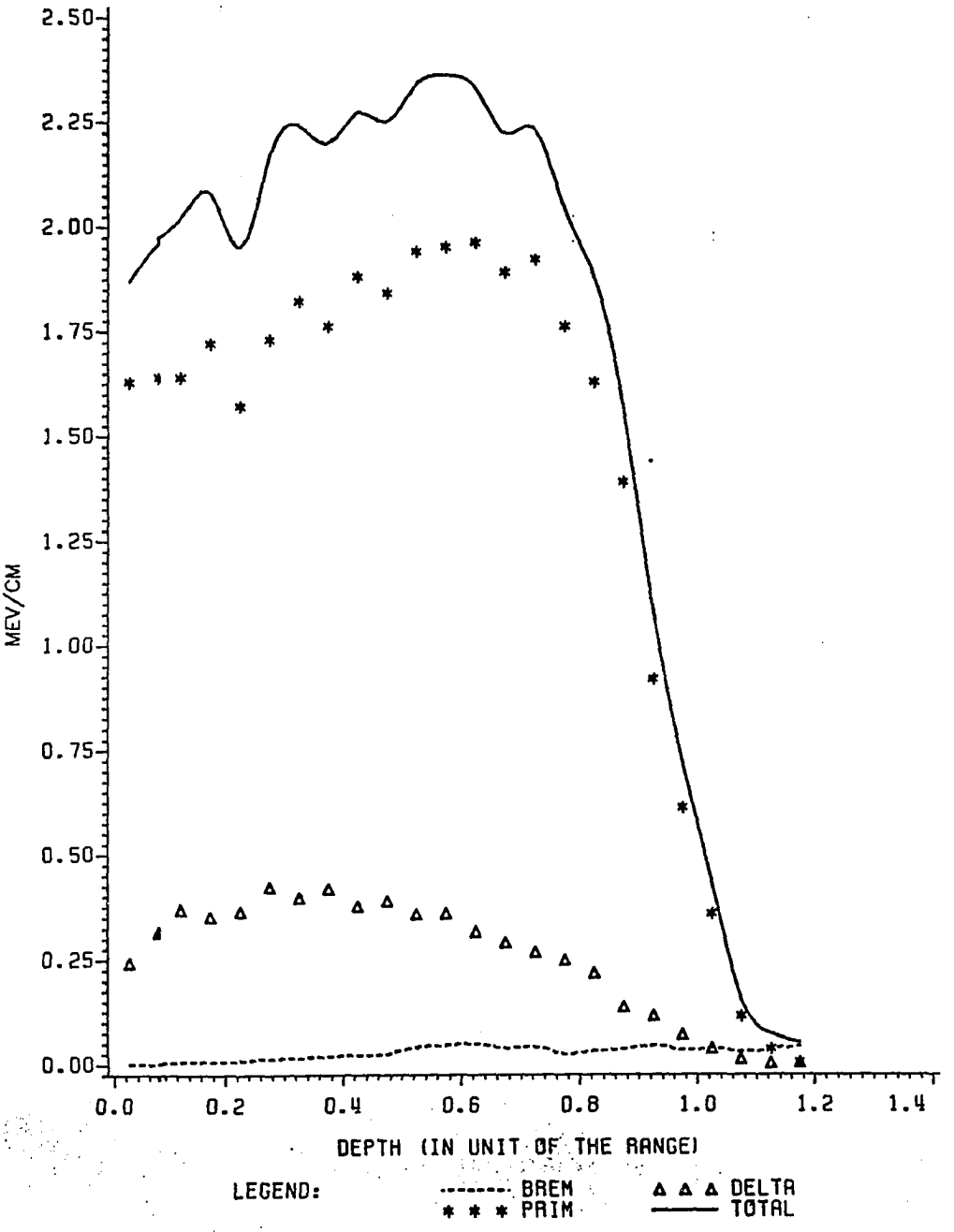

Figure 5.10B. Breakdown of the total energy deposition in a water phantom irradiated with a 20 MeV electron beam.

depositions of primary electrons (stars), delta-rays (triangles) and bremsstrahlung (dashed line) based upon a sample of 1000 Monte Carlo histories. It is obvious from these two figures that noticeable contributions of the bremsstrahlung energy deposition to the total energy deposition distribution are found only at depths beyond the range. For a beam with energy up to 20 MeV, the depth dose distribution within the beam range is determined by the energy degradation of primary electrons and delta-rays. From the point of view of radiation therapy, some uncertainty of the radiation dose deposition at depths beyond the range is tolerable since the dosage is too low to harm the tissue significantly. Since the absorbed dose beyond the electron range due to bremsstrahlung is only significant at high energy, not following the bremsstrahlung in the group-skipping model is justified for the energy range of interest in this study.

2. Two-Dimensional Irradiation Geometry

The experimental data obtained at the University of Oklahoma Health Sciences Center were measured using a SAGITTAIRE clinical linear accelerator with a scanning electron beam operating at 10 MeV for various field sizes defined by collimators and trimmers. Relative center-line depth dose was obtained from irradiated radiographic films inserted into a slab phantom. Therefore, the practical situation in which the experimental data were measured is a large beam with small center-line detectors. It is generally assumed that if the beam radius is greater than the particle range, the relative dose measured for a large beam with small

center-line detectors is equivalent to that measured for small center-line beam with large detectors. The calculated results reported in the previous subsection were obtained, in part, using this irradiation geometry model reversal and compared with experimental results for 15 cm x 15 cm field which has a beam radius greater than the 10 MeV electron range. A multi-dimensional transport code, such as MORSE-E or ACCEPT, can be used to calculate the depth energy distribution for the practical irradiation geometry of large beam with small center-line detectors. This kind of calculation is valuable for two reasons. First, when the beam radius is greater than the beam range, the two-dimensional irradiation geometry calculation can check the validity of the conventionally-used model reversal. Second, when the beam radius is smaller than the beam range, the two-dimensional calculation is the only approach available for depth dose distribution. In addition, the two-dimensional calculation is required if off-axis doses are to be predicted.

In this subsection, the three-dimensional Monte Carlo code MORSE-E is used to simulate the irradiation geometry of a large beam with small center-line detectors. Two kinds of boundary conditions were tested and reported in this subsection. One boundary condition is that of a parallel uniform beam perpendicularly incident on the water surface. The other is that of an external point source, SSD away from the water surface on the center-line, which irradiates electrons uniformly distributed in the solid angle subtended by the irradiated surface. In the

latter boundary condition the value of SSD (Source Surface Distance) controls the geometrical divergence of the beam. The experimental case is expected to be somewhere between parallel and uniformly distributed in solid angle. MORSE-E Code was slightly modified to enable it to handle the nonparallel beam.

Figure 5.11 shows the depth dose distribution for 15 cm x 15 cm field. The MORSE-E results were obtained with beam radius of 7.5 cm and center-line detector radius of 0.75 cm. The results reported are based on a sample of 160,000 Monte Carlo histories using the group-skipping model. This is approximately equivalent to a sample of 1,600 electron histories in the center-line detector region, since the detector radius is only one-tenth of the beam radius. The reported two-dimensional results thus include a statistical uncertainty about 2.5%. In Figure 5.11, the solid curve is the measured depth dose distribution for a 15 cm x 15 cm field. Results for a two-dimensional parallel beam are plotted as a solid histogram while predictions by point diverging beam are represented by a dashed histogram. The one-dimensional geometry model reversal results calculated by MORSE-E are plotted in stars. Within the statistical uncertainties of the Monte Carlo simulations, the one-dimensional geometry results should be expected to be equivalent to the two-dimensional parallel beam results. This appears to be true at depths less than the point of maximum dose, but may not be so at greater depths, especially where the dose drops sharply. This may represent an unresolved uncertainty in the methods. The surface dose to peak dose ratio calculated by both the two-dimensional parallel

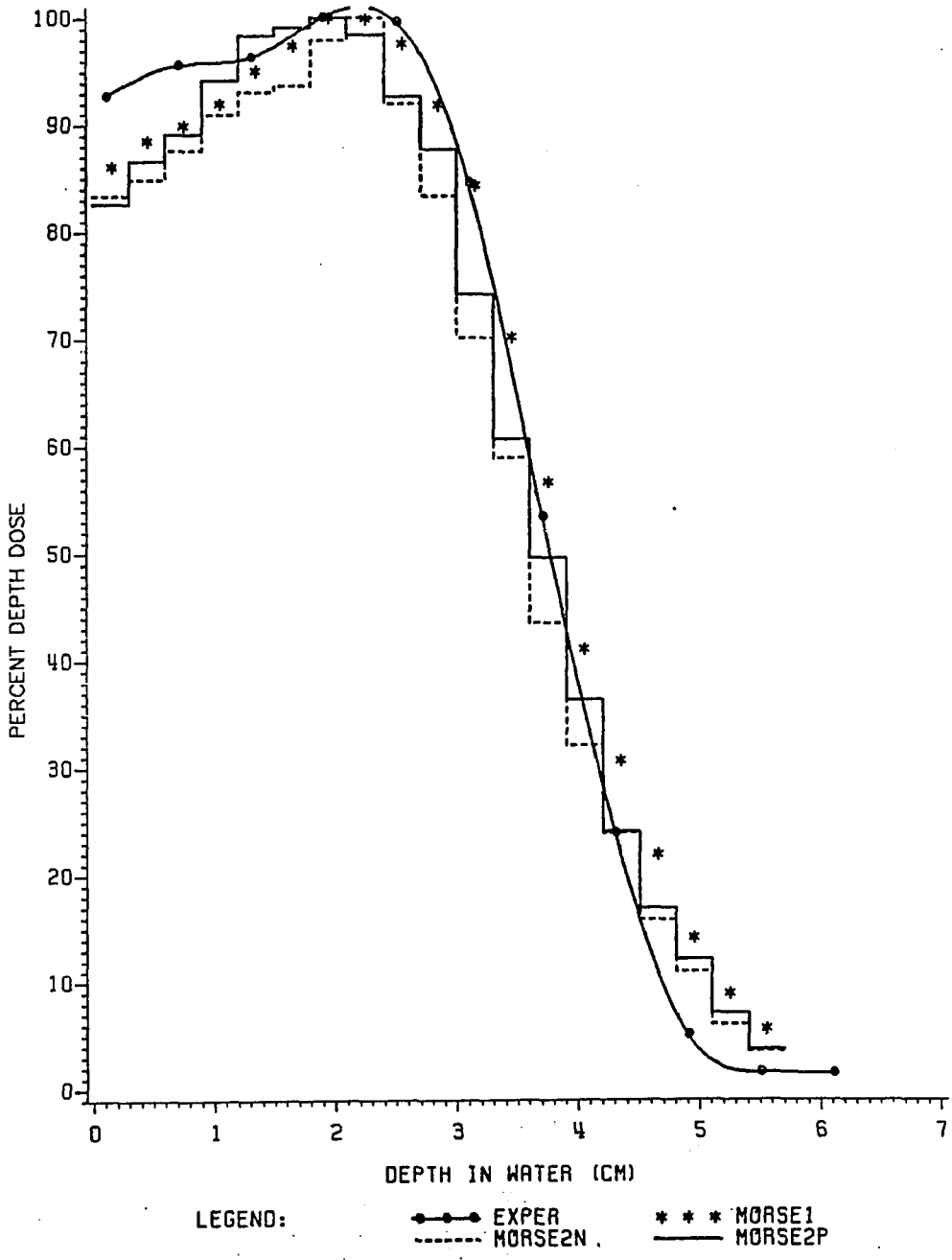

Figure 5.11. Normalized energy deposition in a water phantom irradiated with a 10 MeV electron beam. (Two dimensional irradiation geometry results from group-skipping model are compared to measured data with 15cm x 15cm beam area.)

beam and diverging beam is smaller than the measured data but very close to that predicted by one-dimensional geometry model reversal. The parallel beam result seems to have a slightly earlier peak than the measured data. Since the MORSE-E calculation uses the group-skipping cross-section inherited with the probabilistic energy loss property, all results calculated by MORSE-E show a prominent tail beyond the electron range. Following a sample of 2,500 Monte Carlo histories with MORSE-E code using group-skipping cross-section and one-dimensional geometry model takes about 1.5 minutes running time on an IBM 3081 computer. To obtain similar results using two-dimensional geometry model, the MORSE-E code has to follow more than 160,000 electron histories and takes at least 45 minutes of computer running time. Therefore, it is reasonable to employ the geometry model reversal when the radius of the incident beam is greater than the electron range.

Figures 5.12 through 5.16 display the depth dose distribution for various field sizes. The solid curves on these five figures represent the relative energy distribution measured using an accelerator operating at 10 MeV for a field size of 12 cm x 12 cm, 10 cm x 10 cm, 8 cm x 8 cm, 6 cm x 6 cm, and 4 cm x 4 cm, respectively. In these figures, the solid histograms are results of two-dimensional MORSE-E calculations with parallel uniform beams, while the dashed histograms are those results with diverging beams (uniformly distributed in solid angle). Each histogram plotted in these figures are based on sampling 160,000 electron histories. The radius of the beam for MORSE-E calculations in these figures

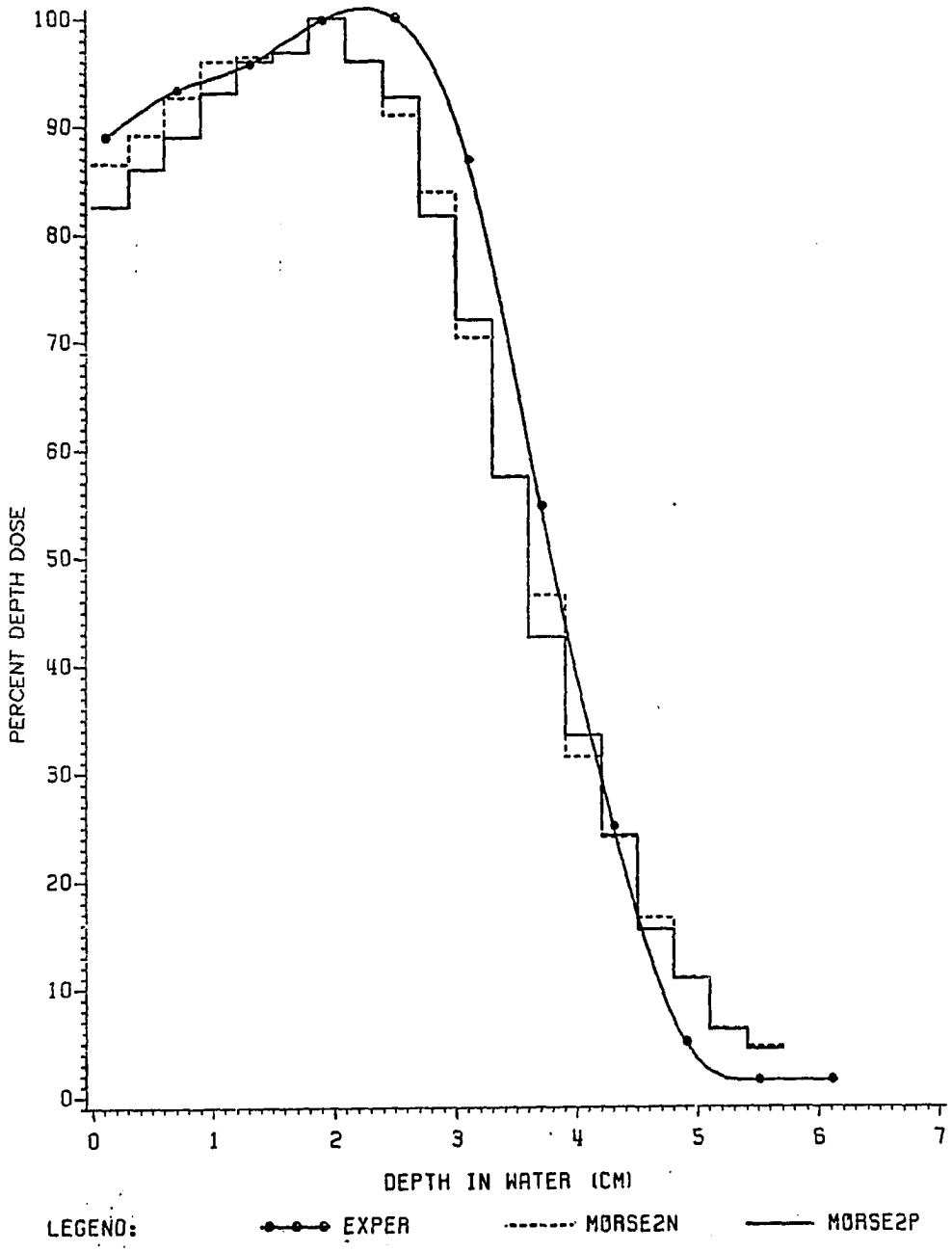

Figure 5.12. Normalized energy deposition in a water phantom irradiated with a 10 MeV electron beam. (Two dimensional irradiation geometry results from group-skipping model are compared to measured data with 12cm x 12cm beam area.)

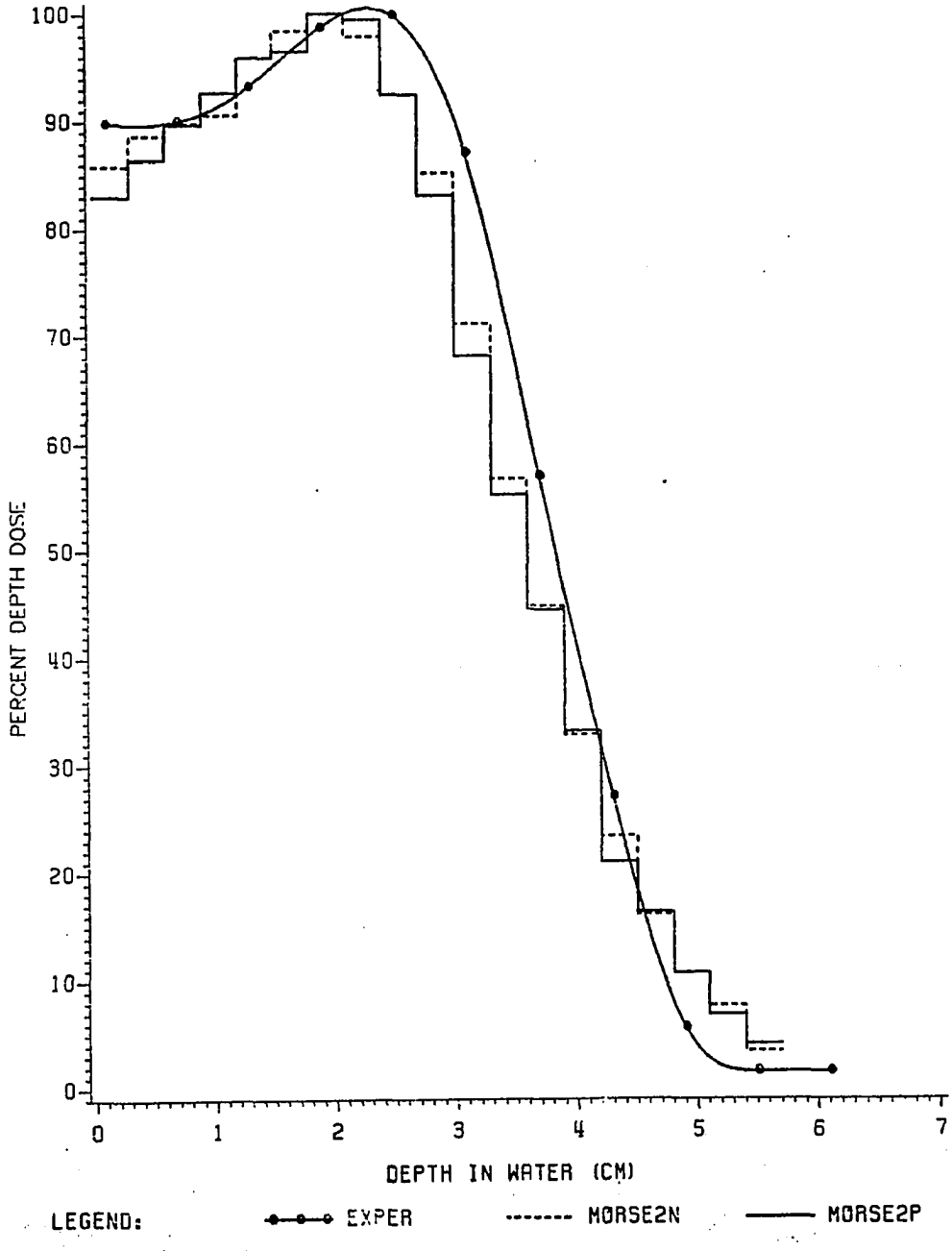

Figure 5.13. Normalized energy deposition in a water phantom irradiated with a 10 MeV electron beam. (Two dimensional irradiation geometry results from group-skipping model are compared to measured data with 10cm x 10cm beam area.)

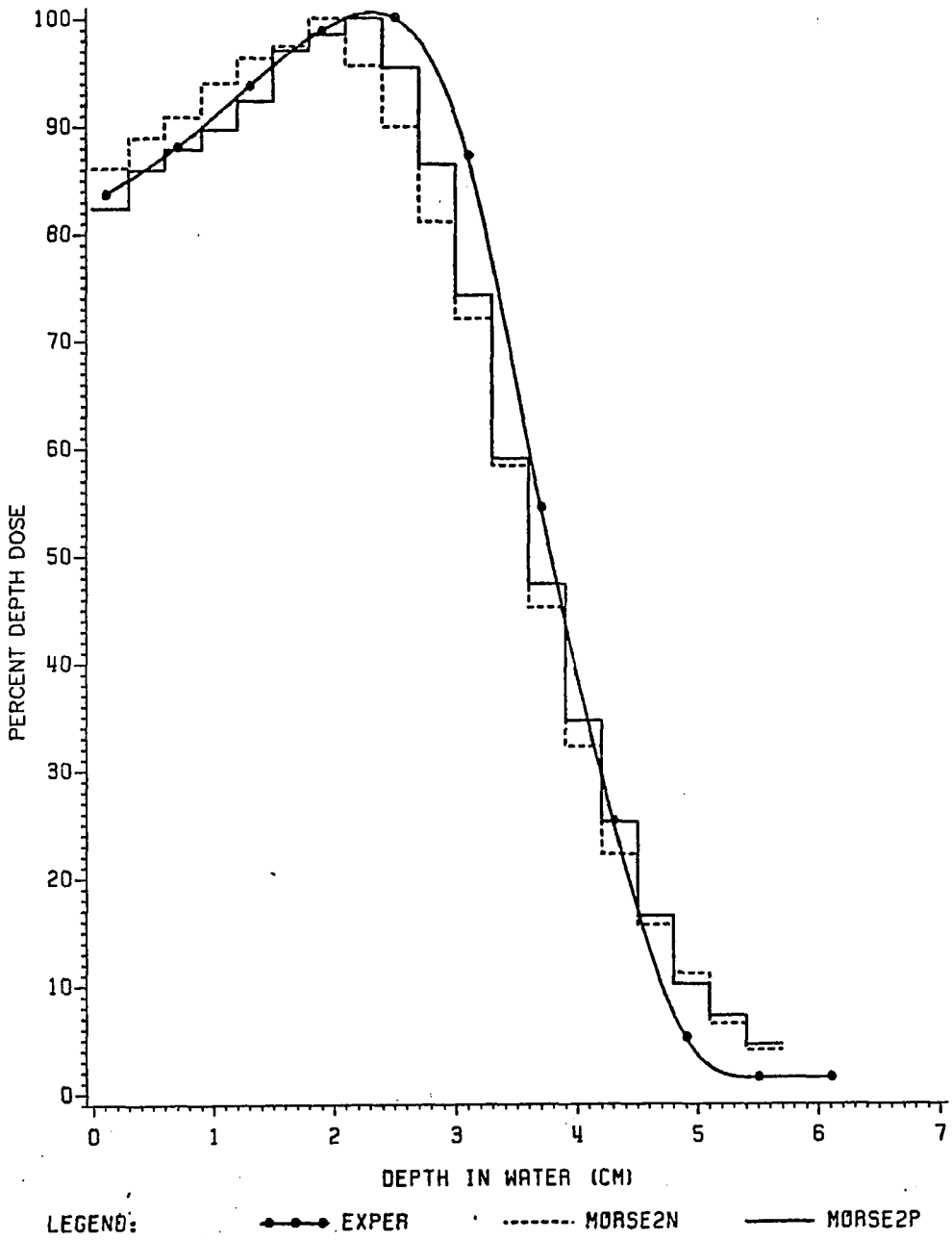

Figure 5.14. Normalized energy deposition in a water phantom irradiated with a 10 MeV electron beam. (Two dimensional irradiation geometry results from group-skipping model are compared to measured data with 8cm x 8cm beam area.)

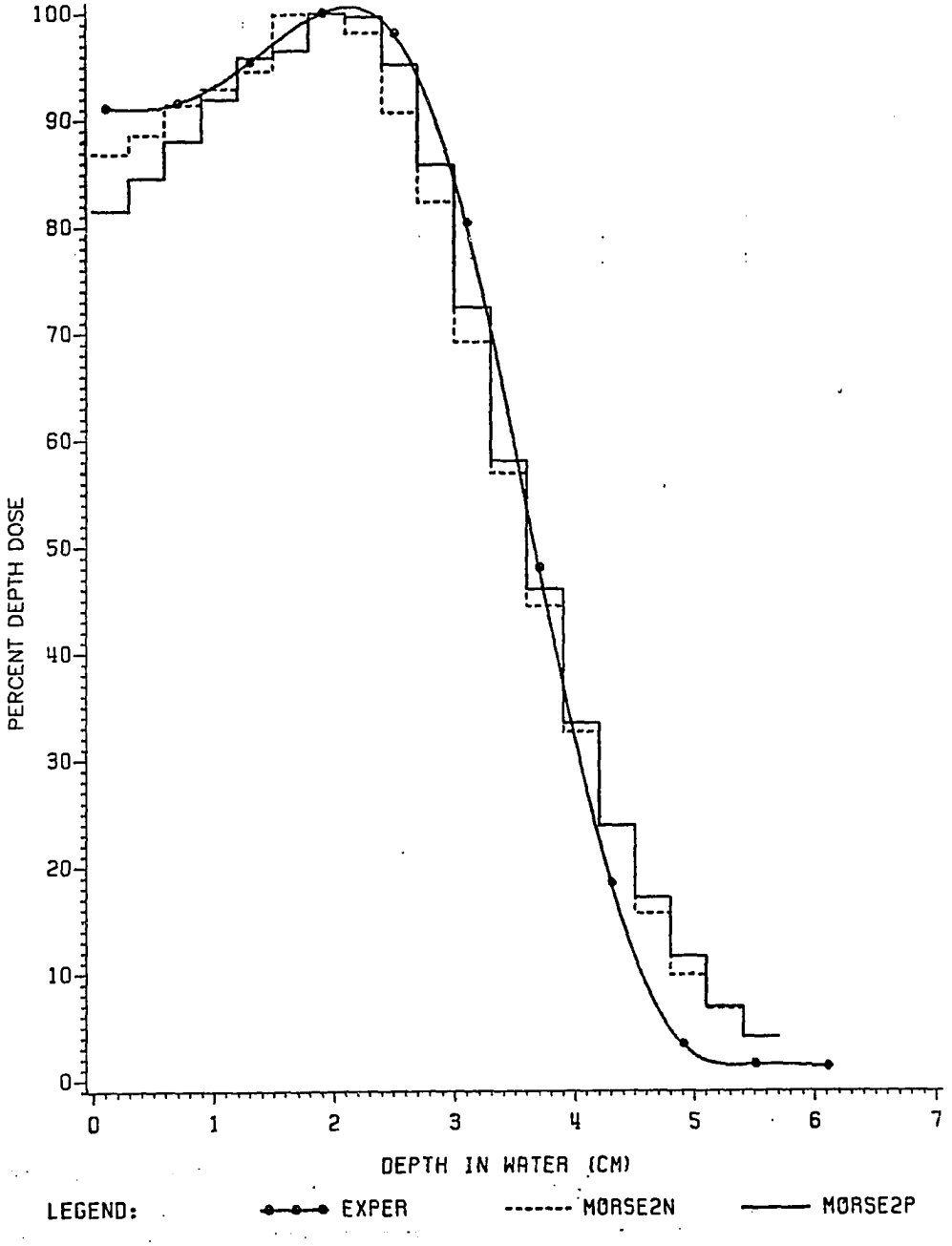

Figure 5.15. Normalized energy deposition in a water phantom irradiated with a 10 MeV electron beam. (Two dimensional irradiation geometry results from group-skipping model are compared to measured data with 6cm x 6cm beam area.)

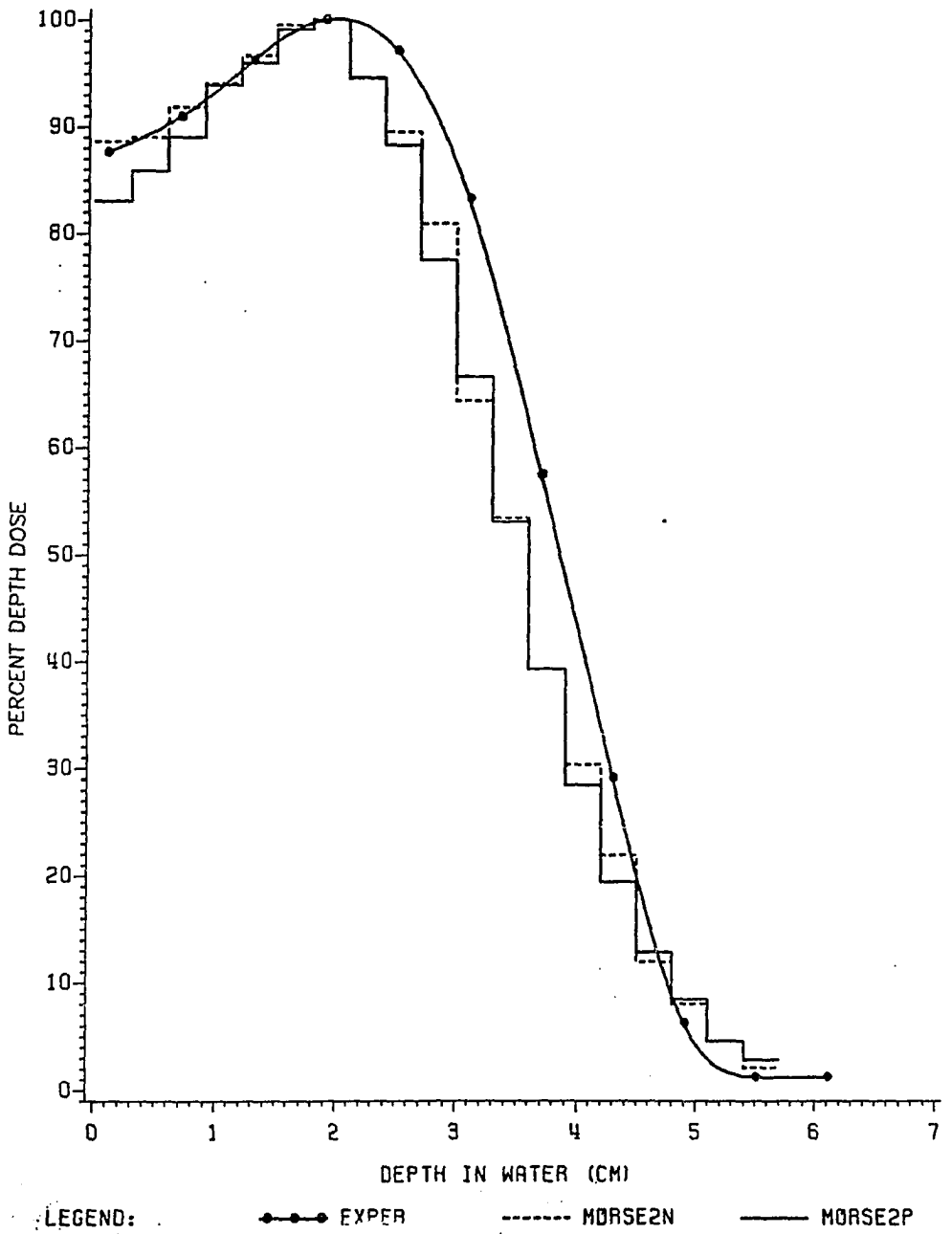

Figure 5.16. Normalized energy deposition in a water phantom irradiated with a 10 MeV electron beam. (Two dimensional irradiation geometry results from group-skipping model are compared to measured data with 4cm x 4cm beam area.)

is 6 cm, 5 cm, 4 cm, 3 cm, and 2 cm, respectively, while the radius of the small center-line detector is 0.6 cm, 0.5 cm, 0.4 cm, 0.3 cm and 0.2 cm in the corresponding figure. Therefore, each histogram is associated with a 2.5% statistical uncertainty of the Monte Carlo calculation. For each field size, the calculated total dose deposition in the surface detector is about the same under two different boundary conditions. However, the parallel beam boundary condition results in a peak dose higher than that calculated by the diverging beam boundary condition. Therefore, the normalized surface dose to peak dose ratio calculated with parallel beam is usually smaller than that predicted by the diverging beam. Generally speaking, the two-dimensional MORSE-E results for the depth dose distribution agree well (but not perfectly) with the measured depth dose data in depth of peak dose, rate of dose fall-off beyond the peak and, in some cases, the surface dose to maximum dose ratio. For most cases the predicted dose appears to be less than the measured dose for depths greater than the maximum dose. Some other normalization scheme (than 100 at the peak) might alter this view, but without an absolute measurement, it is a reasonable standard for comparison. This two-dimensional irradiation geometry model should not be used in particle transport calculations due to the long computer running time unless the beam radius is smaller than the beam range.

Recently, a three-dimensional electron transport Monte Carlo code ACCEPT, [58] has become available to simulate the two-dimensional irradiation geometry model used with the MORSE-E code.

The ACCEPT code employs a volume detector to calculate particle fluxes and reaction rates. This requires following as many Monte Carlo histories as MORSE-E code does in order to obtain statistically acceptable results. The ACCEPT code uses the same mathematical models as ETRAN, so the depth dose distribution calculated by ACCEPT is expected to be similar to that obtained by ETRAN, the widely used one-dimensional electron transport code. The ACCEPT code was obtained, but attempts to make it operable on the IBM 3081 computer were unsuccessful. The ACCEPT code, which is currently operable on CDC-7600 computers, contains some programming not acceptable by the IBM computer. Since not much difference would be expected on the depth dose distribution calculated by ETRAN and ACCEPT and a large effort would be required to make ACCEPT operable on the IBM computer, further attempts were abandoned with some reluctance.

One option available from the MORSE code to eliminate the problem of statistical uncertainty inherited from the large-beam, small-detector geometry model, is the "point detector estimator." This option is used when it is desirable to employ Monte Carlo techniques to estimate particle fluence or fluence-like quantity, at a point in space. The basic method is the "next-event" estimator which scores, from each collision point, the probability of the next event being at the detector. Test runs of the "point detector estimator" option using the MORSE cose, however, produce a depth dose distribution that is monotonously decreasing from the surface. This result is unacceptable since the measured depth dose distribution shows a gradual build-up,

followed by a sharp fall-off.

B. 1 MeV Electrons Incident on Aluminum

In this section, the group-skipping model will be used in the discrete ordinates code, ANISN, to study the energy spectra and angular distributions of transmitted electrons through aluminum slabs. The experimental data presented here for comparison are taken from the work of Rester and Derrickson [59]. In addition, the Monte Carlo results of ETRAN18G are also included. Results are given for normal incidence of 1 MeV electrons on aluminum targets.

The solid curves plotted in Figures 5.17 and 5.18 show the experimental data of the transmitted electron current per unit energy for 1 MeV electrons normally incident on aluminum slabs of thicknesses of 0.22 g/cm^2 and 0.32 g/cm^2, respectively. These thicknesses roughly correspond to 0.4 and 0.6, respectively, of the range of the incident electrons. The dotted curves in the figures represent the results from ANISN calculations using the group-skipping model cross section data. The triangles plotted in the figures represent the ANISN results using the continuous-slowing-down model cross section data. The solid histograms represent the results from ETRAN18G calculations using the energy-loss straggling and with the secondary particles followed. The stars plotted in the figures represent the ETRAN18G results using the continuous-slowing-down approximation. In Figures 5.17 and 5.18, the ANISN-CSDM results are quite similar to those of the ANISN calculations using the group-skipping model, but the spectra of the latter are shifted to a slightly higher

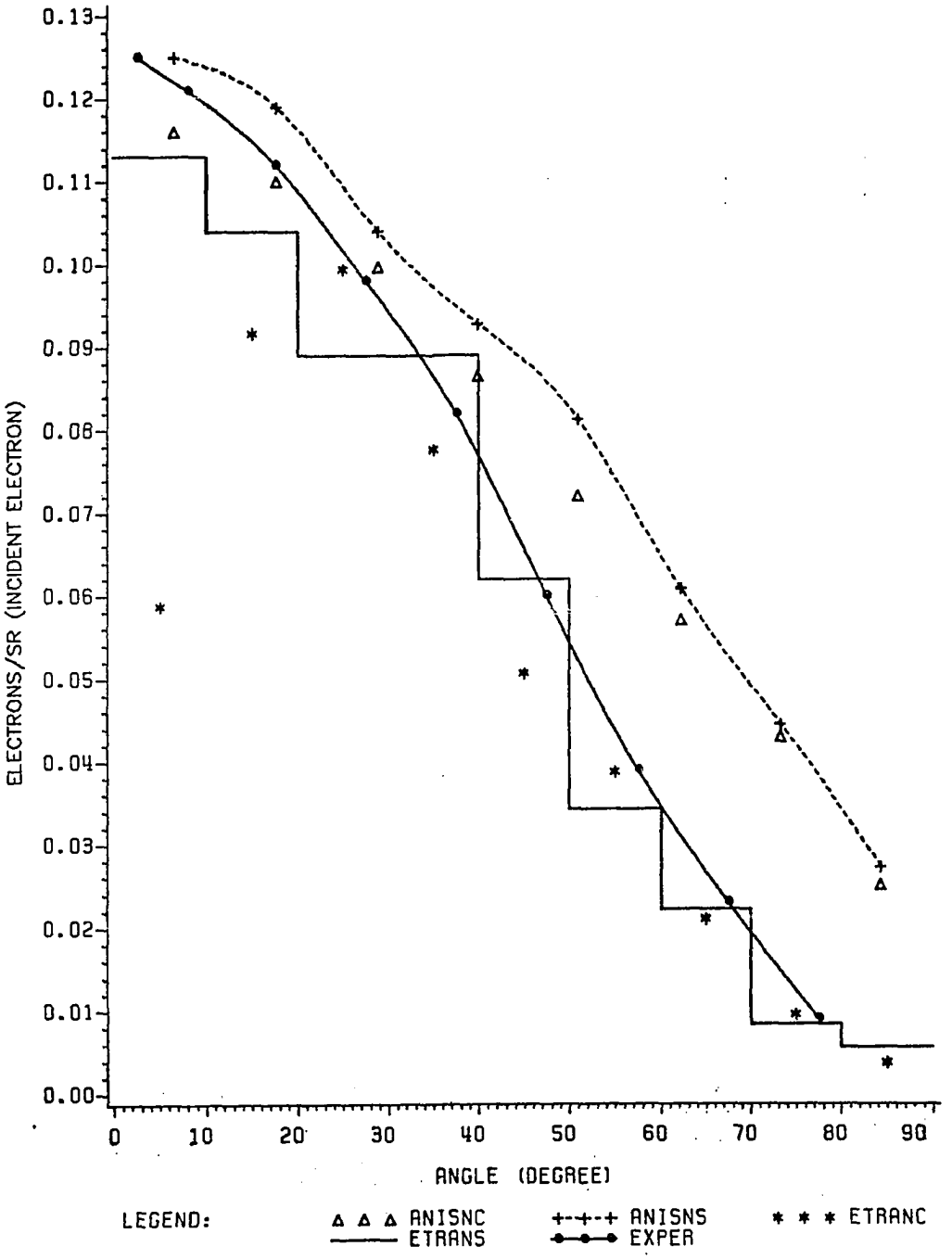

Figure 5.17. Transmitted electron current per unit energy per incident electron for 1-MeV electrons normally incident on a aluminum slab with 0.22 g/cm^2 thickness.

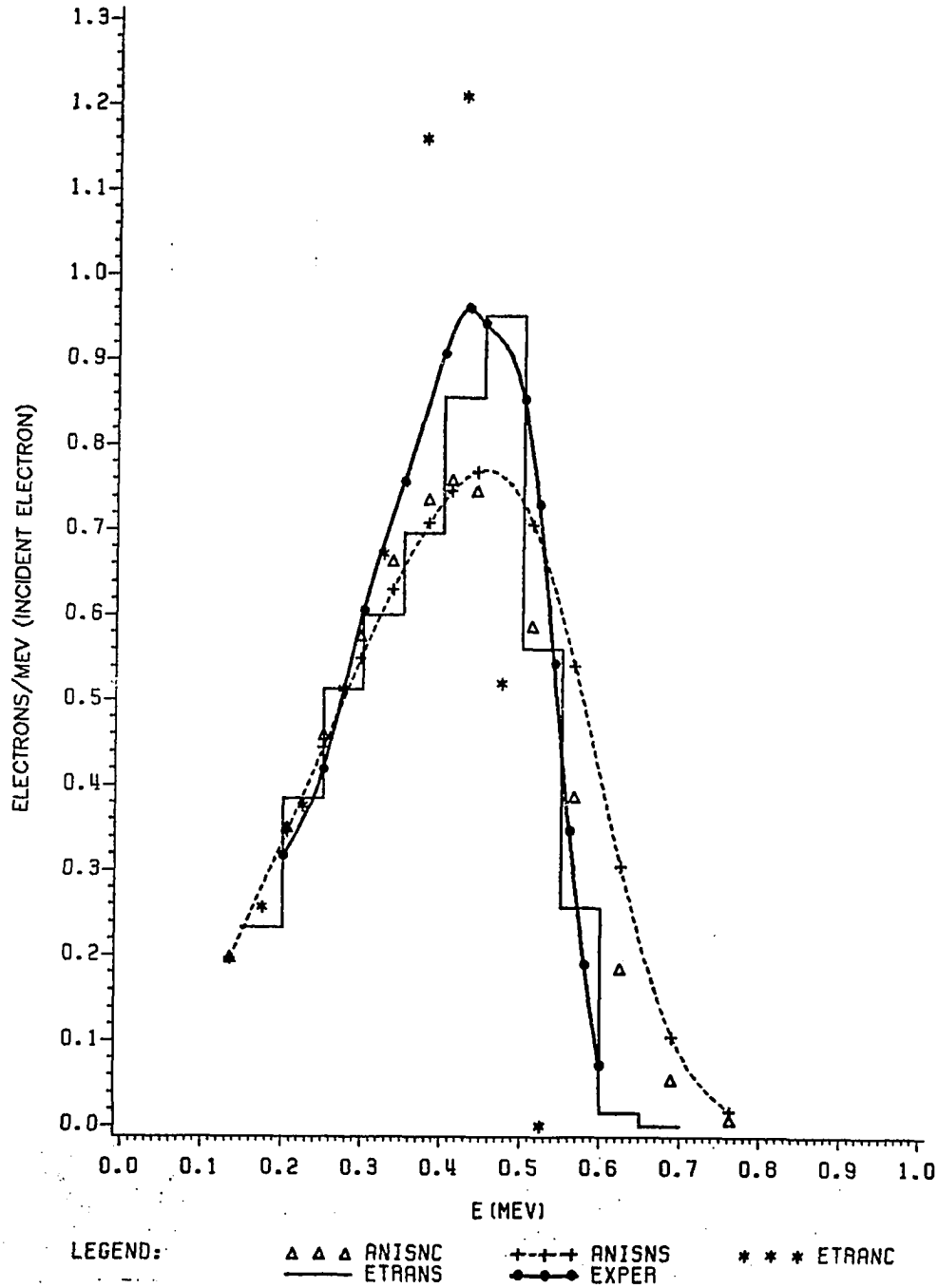

Figure 5.18. Transmitted electron current per unit energy per incident electron for 1-MeV electrons normally incident on a aluminum slab with 0.32 g/cm^2 thickness.

energy. The energy spectra calculated by ANISN are wider than the results predicted by ETRAN18G. This is probably due to the probabilistic energy-loss property of ANISN and the deterministic energy-loss property of ETRAN. In the figures, the ANISN results agree quite well with the experimental data at the low energies. Also, there exists a good agreement in predicting the location of the peak of the transmitted energy spectra. However, the experimental results are greater than the ANISN results at the peak of the distribution and lower at the high-energy edge. Overall, it appears that the ETRAN18G, with straggling, predicts the measured results somewhat better than either of the ANISN calculations. The ETRAN18G predictions using the continuous-slowing-down approximation (stars) appear less valid.

The angular distributions of the transmitted electron current per unit solid angle for 1 MeV electrons normally incident on 0.22 g/cm^2 and 0.32 g/cm^2-thick aluminum slabs are shown on Figures 5.19 and 5.20. The solid curves represent the experimental data. The ANISN results are plotted in dashed lines (group-skipping cross section) and triangles (continuous-slowing-down model). The values calculated by the discrete code ANISN are based on a 44th order Legendre expansion coefficients, a 48 quadrature order and 85 energy groups. The group structure reduces the electron energy by half in 28 groups. In the group-skipping model, the catastrophically-collided electron will skip 10 energy groups. The ETRAN18G results are plotted in solid histograms (energy-loss straggling model) and stars (continuous-slowing-down approximation). The ETRAN results reported here are based on

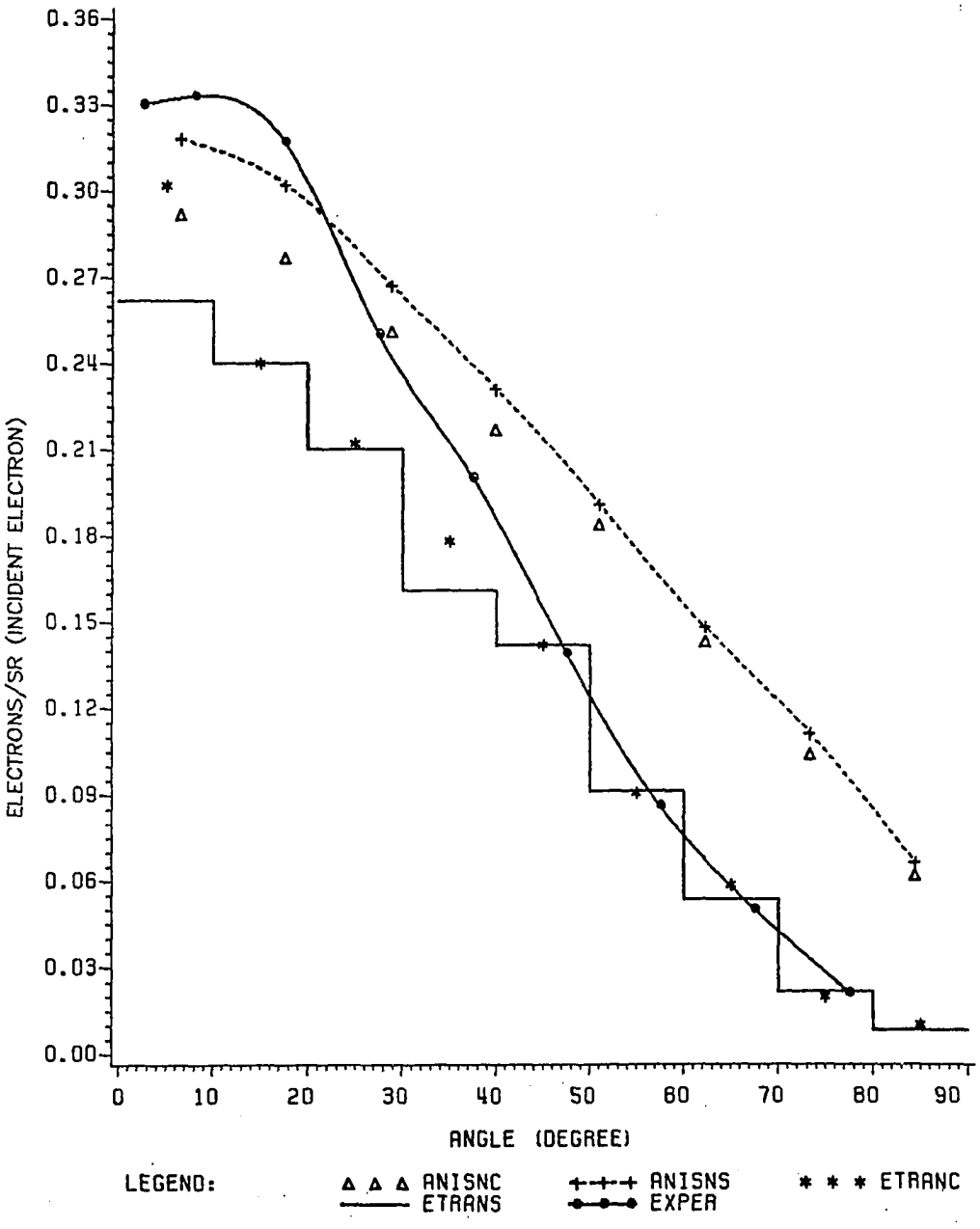

Figure 5.19. Angular distribution of the transmitted electron current for 1-MeV electrons normally incident on a aluminum slab with 0.22 g/cm^2 thickness.

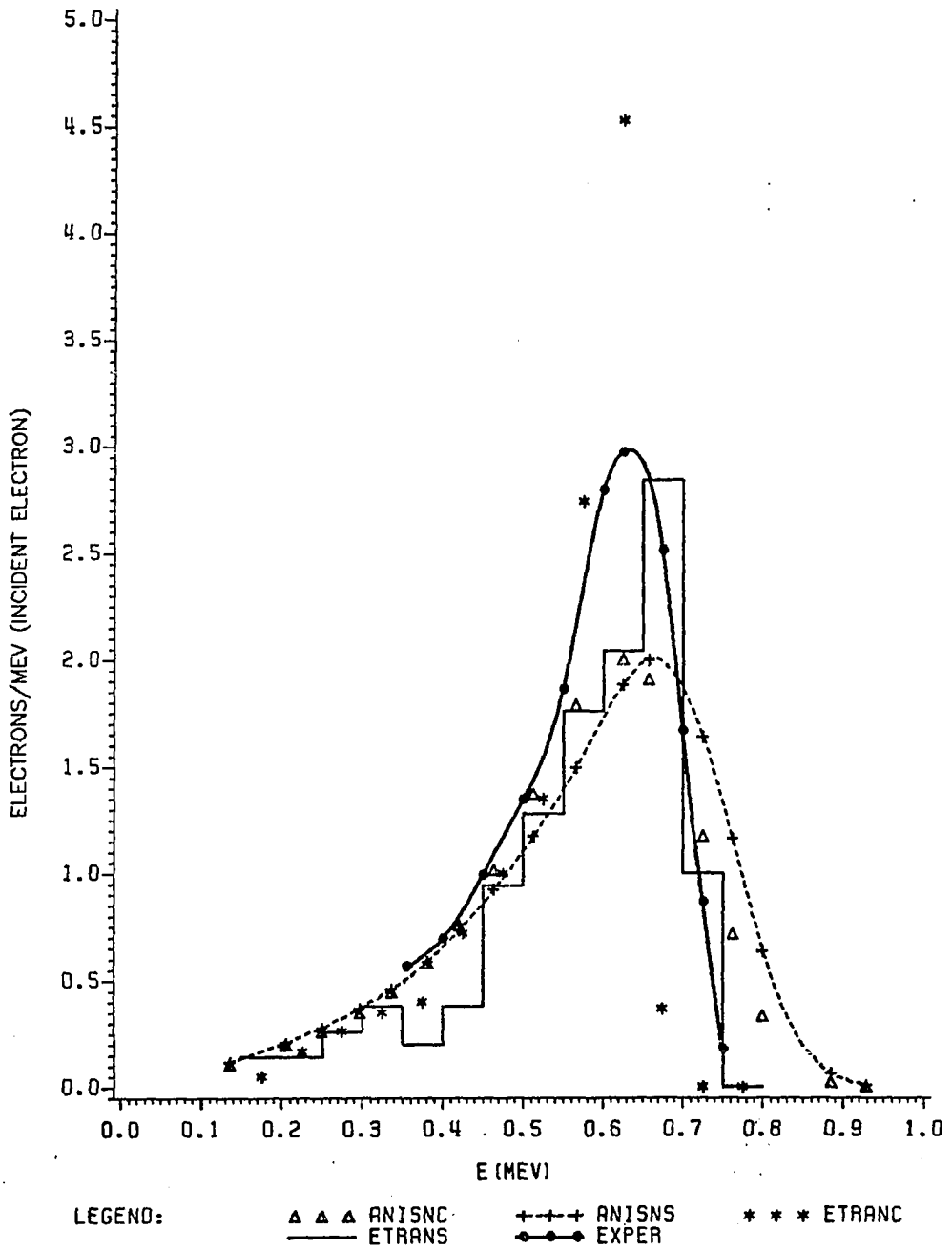

Figure 5.20. Angular distribution of the transmitted electron current for 1-MeV electrons normally incident on a aluminum slab with 0.32 g/cm^2 thickness.

sampling 2500 Monte Carlo histories. The values calculated by ANISN for the 0.22 g/cm^2 case are greater than the experimental measurements over much of the distribution, although the calculated values are slightly low at the forward angles. The results calculated by ETRAN are lower than the measured data at the forward angles, but are in reasonable agreement at large angles. For the 0.32 g/cm^2 case, the results of ANISN calculations using the group-skipping cross section are slightly higher than the measured data through all the distributions. The results of ANISN-CSDM also follow this general tendency, although the calculation is slightly low at forward angles. The values of ETRAN-straggling calculations are lower than the experimental measurement at the forward angles but good agreement is found through much of the distribution. The ETRAN-CSDA results are lower than the measured data throughout the distribution. Overall, the ANISN methods appear to agree with experimental results slightly better for smaller angles and ETRAN methods agree better for large angles, with trends generally correct for both codes.

C. 1 MeV Electrons Incident on Gold

In this section, the cross section data of the continuous-slowing-down model and the group-skipping model will be used in the standard ANISN code to investigate the energy spectra and angular distributions of transmitted electrons through gold slabs. The experimental measurements presented here are taken from the work of Rester and Derrickson. The Monte Carlo results calculated by widely used electron transport code ETRAN are also included for comparison.

The total transmitted electron current per unit energy resulting from 1 MeV electrons normally incident on 0.15 g/cm^2 and 0.31 g/cm^2-thick gold slabs are shown in Figures 5.21 and 5.22, respectively. These gold slab thicknesses represent approximately 0.2 and 0.4, respectively, of the range of the incident electrons. All the symbols, curves and histograms appearing in this section are similar to those used earlier for the aluminum cases. The ANISN results reported here are based on a 44th order Legendre polynomial expansion, a 48 quadrature order and 85 energy groups. The energy group structure uses a group parameter m = 28, which means that the mean energy of the energy group is reduced by half after 28 groups. In the group-skipping model, a primary electron skips 10 energy groups when it is catastrophically collided. The ETRAN18G results reported here are based upon a sample of 10,000 Monte Carlo histories. For the 0.15 g/cm^2-thick case, the best ETRAN results are slightly higher than the experimental measurements at low energies and less than the measured data at high-energy edge. Both of the ETRAN results and the ANISN-CSDM results predict a spectrum peak at an energy position slightly lower than that of the measured data. The energy spectrum calculated by ANISN with the group-skipping model shows generally good agreement with the measurements at all energies. Figure 5.22 represents the deep penetration of 1 MeV electrons through a gold slab. The ANISN group-skipping model produces a spectrum nearest to the measured one. It agrees in general shape with the measured spectrum but the magnitude is somewhat different. The ratio of the number of

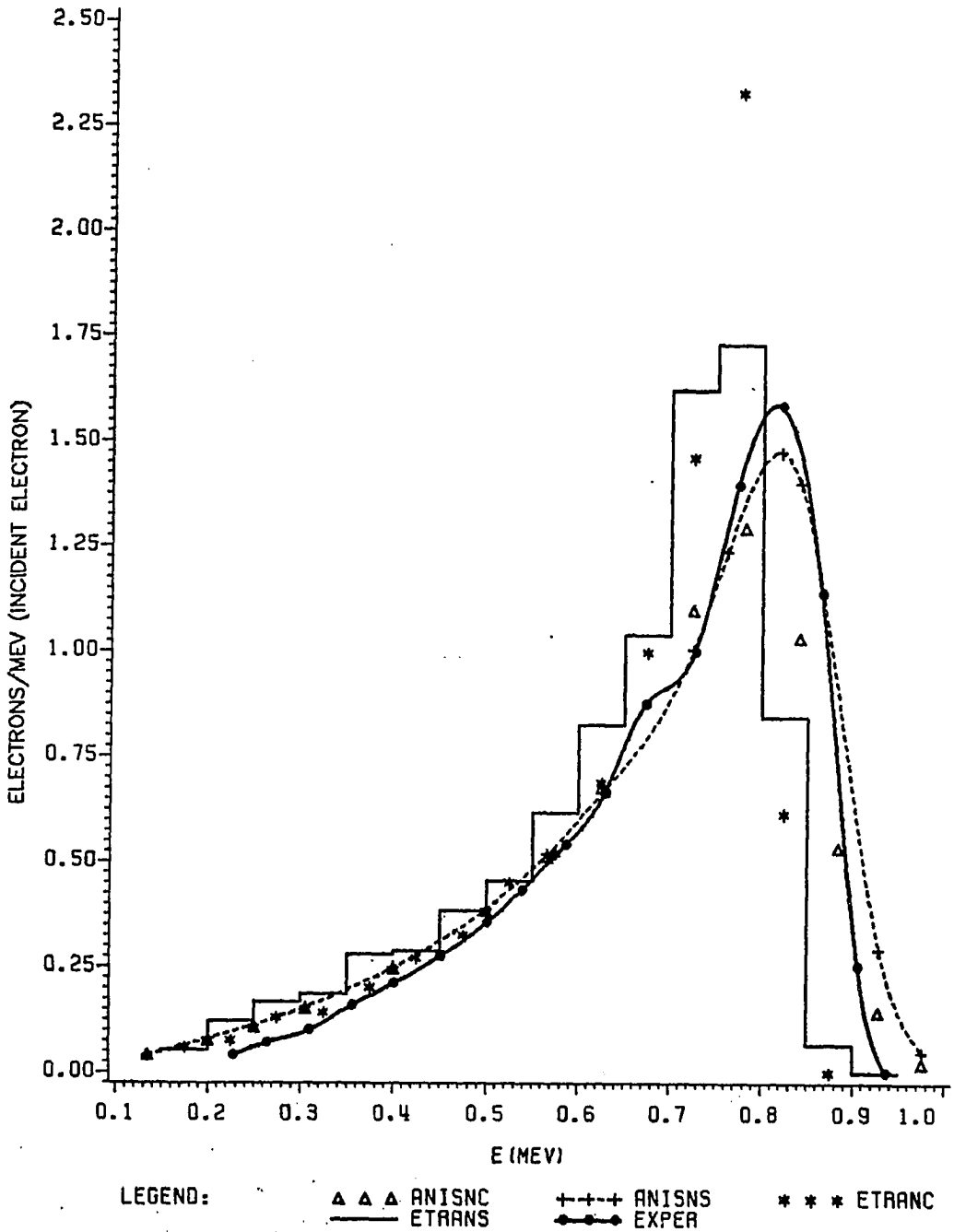

Figure 5.21. Transmitted electron current per unit energy per incident electron for 1-MeV electrons normally incident on a gold slab with 0.15 g/cm^2 thickness.

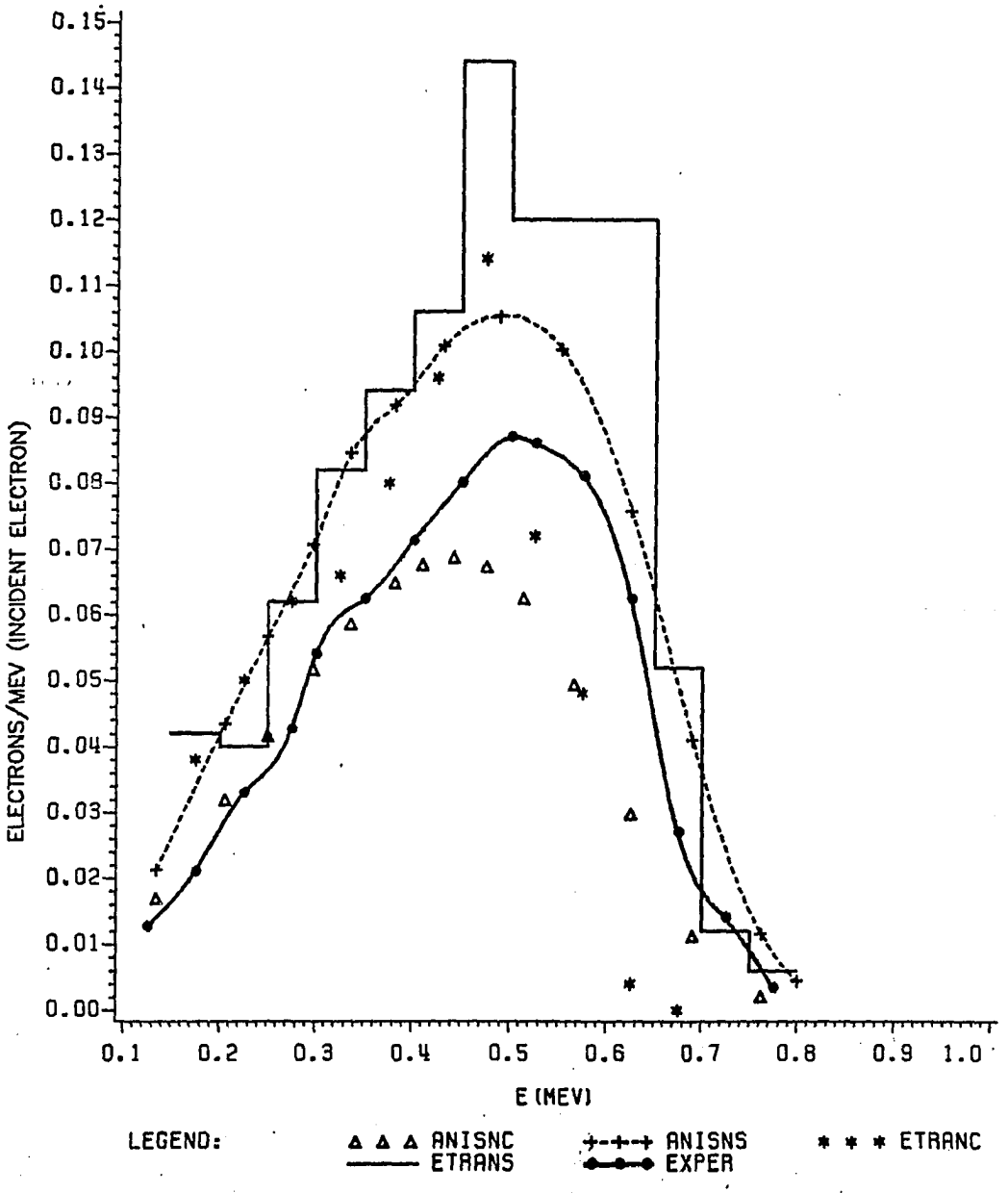

Figure 5.22. Transmitted electron current per unit energy per incident electron for 1-MeV electrons normally incident on a gold slab with 0.31 g/cm^2 thickness.

electrons which penetrate through the 0.31 g/cm^2-thick gold slab to the number of electrons incident on the slab surface, given by the area under the appropriate curve, is 5.0% as calculated by ETRAN-straggling and is 3.2% as calculated by ETRAN-CSDA. The area under the curve of the experimental spectra shows about 3% of the incident electron actually penetrate beyond 0.31 g/cm^2-thick gold slab. Because of the low transmission ratio, the statistical uncertainties of the counts in the individual energy bins of the Monte Carlo calculated spectra are large as might be judged in Figure 5.22 even though 10,000 incident electrons were considered. The ANISN group-skipping model shows about a 4% penetration of incident electrons. The seemingly large difference between the two spectra represents only about 1% of the total incident electrons, and matches the general distribution very well.

The angular distribution of the transmitted electron current per unit solid angle per incident electron for the cases of a 0.15 g/cm^2-thick and a 0.31 g/cm^2-thick gold slab are given in Figures 5.23 and 5.24, respectively. The distributions calculated by ANISN using group-skipping model has a wider angular half-width than the measured data and other calculated results. Thus, in spite of the generally better energy distributions predicted by ANISN, the angular distributions predicted by ETRAN appear to match measurements better for gold slabs.

D. Charge Deposition in Water

One of the advantages of the group-skipping model cross-section data is the potential it possesses to allow investigation

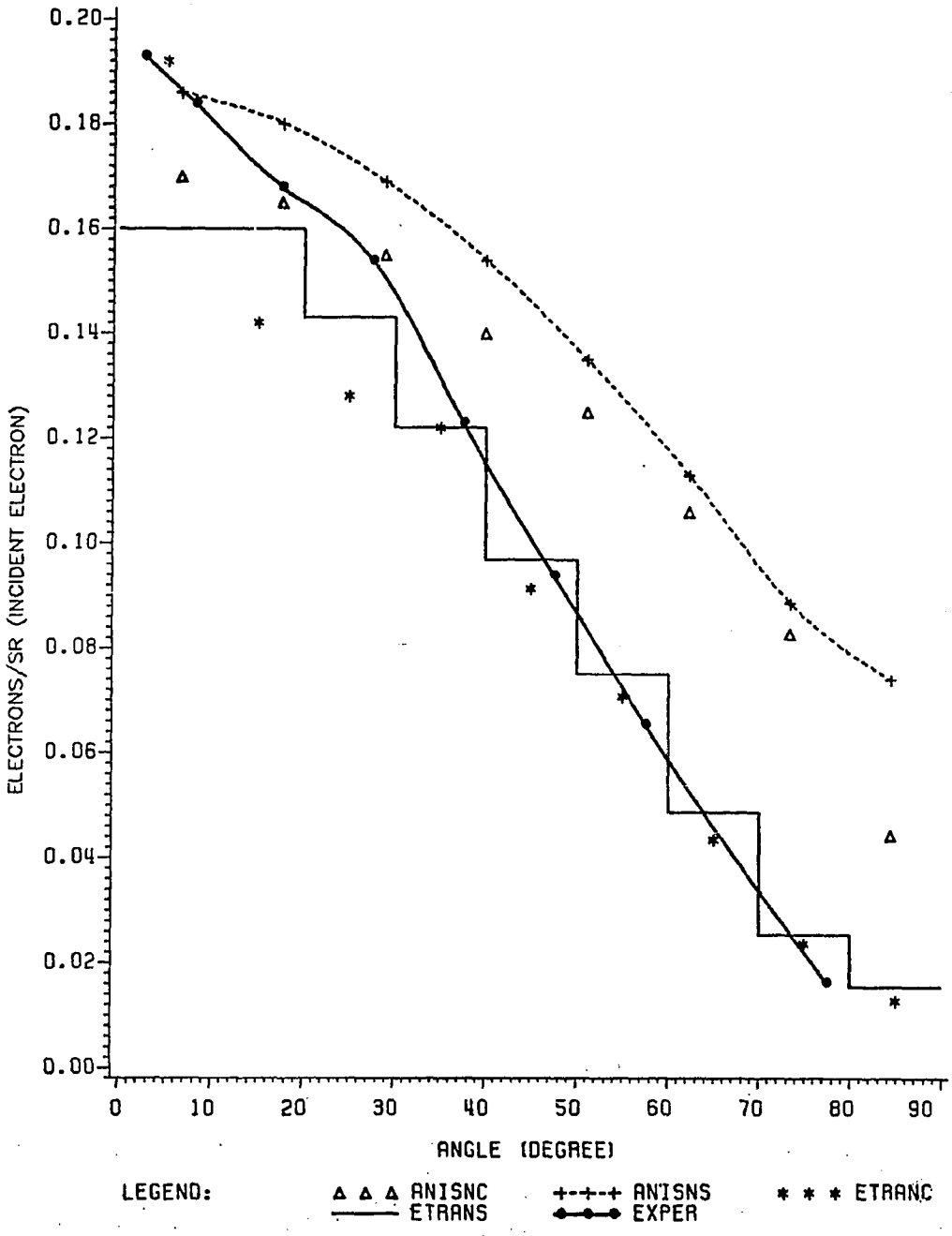

Figure 5.23. Angular distribution of the transmitted electron current for 1-MeV electrons normally incident on a gold slab with 0.15 g/cm^2 thickness.

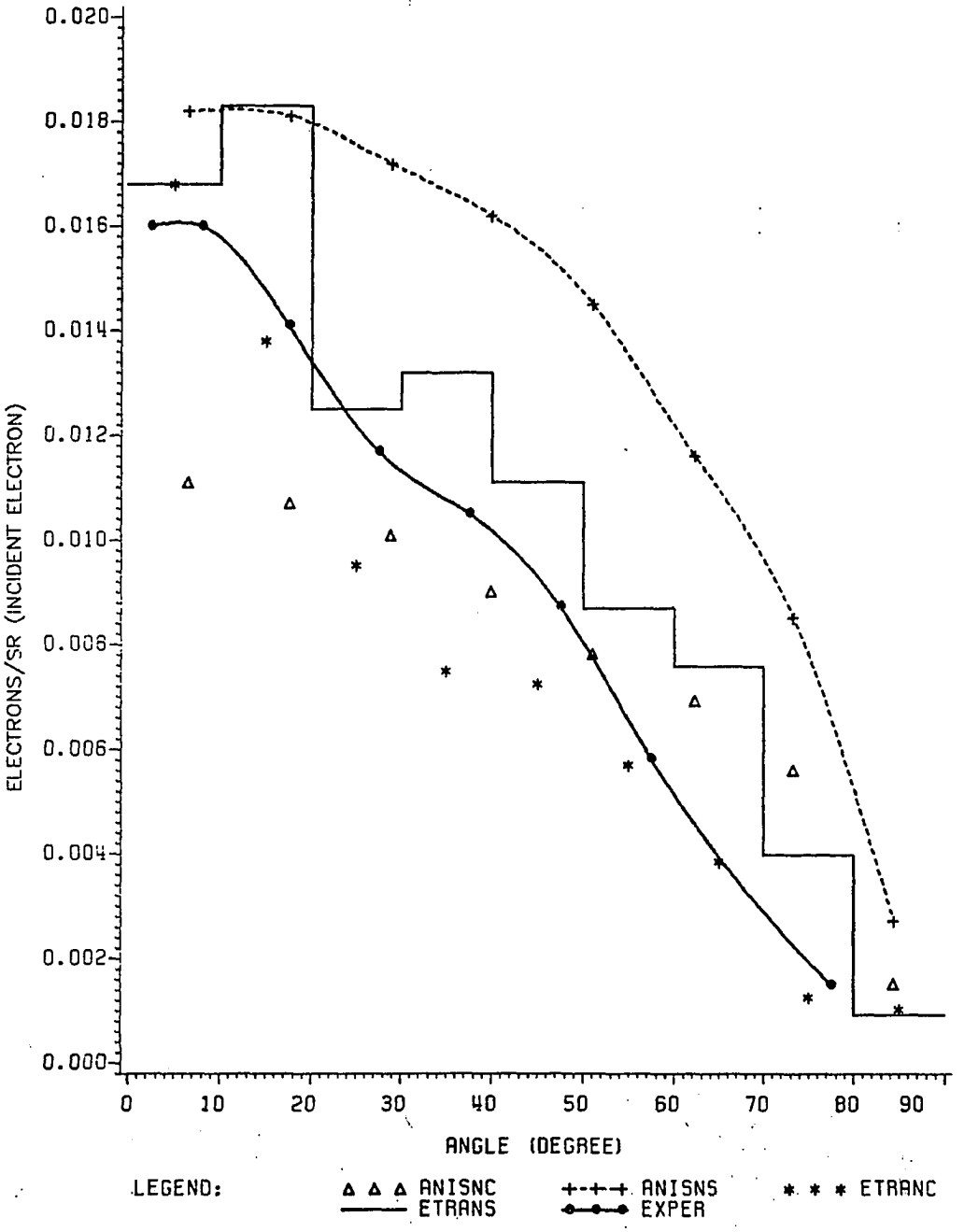

Figure 5.24. Angular distribution of the transmitted electron current for 1-MeV electrons normally incident on a gold slab with 0.31 g/cm^2 thickness.

of the charge deposition distribution (using a neutral particle transport code) in a medium bombarded by electrons. In this section a Monte Carlo approach to the prediction of the depth charge distribution using MORSE-E code has been applied to the case of 20 MeV electrons incident on a water target. The experimental data reported here are taken from the work of Alexander and associates [60].

The calculation of depth charge distribution follows a similar procedure to that used for energy deposition. The medium is divided into many sublayers perpendicular to the incident electron beam. The MORSE-E code was modified so that it can score a withdrawal of a charge from a sublayer in which a catastrophic collision occurs and a delta-ray is removed from an ionized atom. The MORSE-E code was also modified so that it scores a deposit of an electron charge in the sublayer in which the electron at the last energy group loses at Russian roulette and ends its track. The history of the delta ray generated in the catastrophic collision is followed in turn. The MORSE-E results reported on Figure 5.25 is an average of such withdrawals and depositions taken over a 10,000 history Monte Carlo sample. In Figure 5.25 the solid curve shows the experimental data obtained by Alexander and colleagues for charge deposition in water by a 20 MeV beam. The dashed histogram is the result of MORSE-E calculation while the solid histogram is a result of ETRAN18G-straggling with secondary particles followed. The MORSE-E results show fair agreement with the measured data. ETRAN results appear to be somewhat better. The MORSE-E calculation shows a slightly

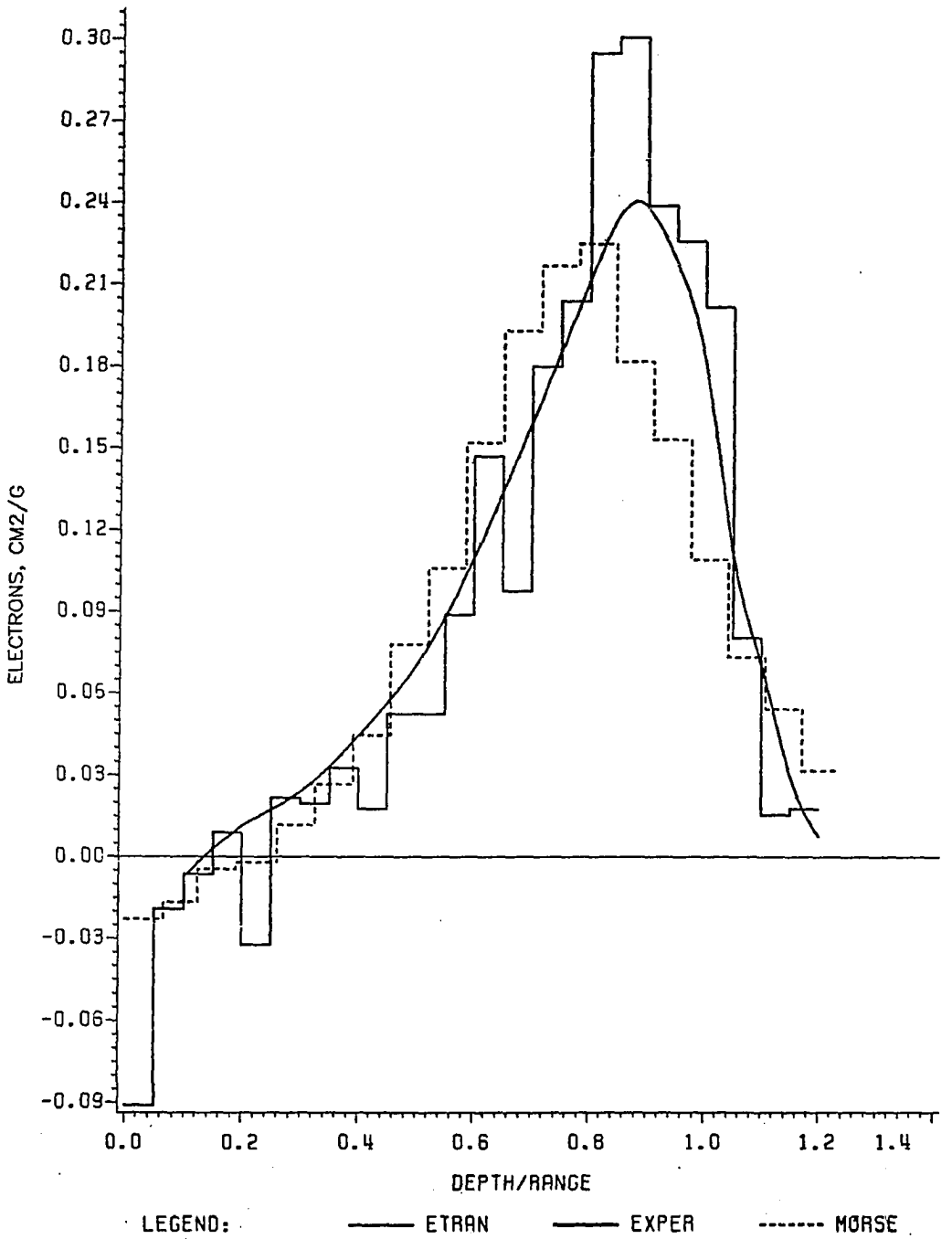

Figure 5.25. Depcsition of charge in a water phantom irradiated with a 20 MeV electron beam. Distribution is normalized to one incident electron.

earlier peak of the charge distribution than the experimental measurements. A more gradual charge fall-off beyond the peak is also shown by the MORSE-E calculation. However, the MORSE-E calculation clearly shows, as the experiments also indicate, a depletion of charge in the surface region. This is to be expected, since at small depths only a few primary electrons are stopped while quite a few energetic delta rays leave the region. A comparison of the experimental data and calculated charge distribution curves in respect to the peak position and FWHM (full width at half maximum) of the distribution is given in Table 5.1.

TABLE 5.1

CALCULATED AND EXPERIMENTAL PARAMETERS OF CHARGE DEPOSITION-DISTRIBUTION FOR 20 MeV ELECTROM BEAM INCIDENT ON WATER

	Peak Position in Units of Z/r_0	FWHM in Units of Z/r_0
MORSE-E	0.81	0.47
Measurements	0.88	0.43
ETRAN-Straggling	0.88	0.34

CHAPTER VI

SUMMARY, CONCLUSIONS AND RECOMMENDATIONS

The primary objective of this research is to employ advanced analytical methods of nuclear engineering to study electron beam therapy. Two computer codes which are quite well-known to nuclear engineers have been used to calculate the deposition of energy from an electron beam in a water phantom that simulates human tissue. One of the codes is a discrete ordinates program, ANISN. The other is a multi-dimensional Monte Carlo code, MORSE-E. Both codes use ANISN format multigroup cross-section data. It was necessary to develop a group-skipping model to prepare the ANISN format electron transport cross-section data. This group-skipping model is an extension of the stepwise continuous-slowing-down model originated by Özdemir [13].

For the case of a 10 MeV electron beam incident on a water phantom, the energy deposition distributions calculated by ANISN and MORSE-E using both the continuous-slowing-down model and the group-skipping model were compared with experimental measurements and predictions of ETRAN, which is the most widely used computer code for electron transport calculations. The principal findings obtained from these comparisons are summarized as follows:

1. The ANISN/MORSE-E results of the energy deposition

in water are generally better than those calculated by ETRAN. The ANISN/MORSE-E results are similar to measured depth dose data in location of the maximum dose depth and dose fall-off beyond the maximum. The ETRAN results show a more prominent peak at a greater depth than ANISN/MORSE-E.

2. The group-skipping model, in general, predicts a broader dose peak from that predicted by the continuous-slowing-down model. This results in better agreement with experimental measurements in the region of the maximum dose.

3. The results from MORSE-E's two-dimensional simulation of a large beam with small center-line detectors agrees well with that from the one-dimensional simulation of a center-line pencil beam with large detectors at depths less than the point of the maximum dose. Since the one-dimensional geometry simulation is more efficient on computer running time than its two-dimensional counterparts, it is reasonable to use the geometry model reversal when the radius of the incident beam is greater than the electron range. Two-dimensional geometry calculation should be performed only if either the off-axis doses are to be predicted or the radius of the incident beam is less than the electron range.

The ANISN code has been used to evaluate the angular and energy spectra of transmitted electrons for a 1 MeV electron beam incident on both aluminum and gold slabs for which

experimental results are available. For aluminum slabs, it appears that the ETRAN calculations, with energy loss straggling, predicts the measured results somewhat better than the ANISN calculations. For gold slabs, the energy spectra calculated by ANISN with the group-skipping model shows generally better agreement with the experimental data at all energies than the ETRAN predictions. However, the angular distributions predicted by ETRAN appear to match measurements better for gold slabs.

The last part of the calculations has been performed to study the charge deposition distribution in a water phantom, a biophysical quantity of interest in electron beam therapy. For the case of a 20 MeV electron beam incident on water, the results calculated from a modified MORSE-E code with the group-skipping model show fair agreement with the measured data. ETRAN results appear to be better in predicting the position of maximum charge deposition.

Based upon the investigations of this study, the group-skipping model electron transport cross-section data can be used with multigroup neutral particle transport codes to predict the energy deposition distributions in a water phantom. The group-skipping model is also recommended to study the energy spectra of transmitted electrons in gold slabs. The ETRAN-straggling calculations should be used to calculate charge deposition distributions, transmitted electron spectra in aluminum slabs, and angular distributions of transmitted electrons in gold

slabs.

The current group-skipping model has not adequately treated the energy degradation by photon production which becomes important for very high energy beams. Further work in the preparation of electron transport cross-section should include the penetration of bremsstrahlung. The group-skipping model should also be tested with several kinds of transport media other than those reported here to determine the extent of its applicability.

In experimental measurements, the incident electron beam is contaminated with lower energy electrons and photons, produced by interactions of the beam with the lead collimators and trimmers used to define the beam area. To determine the effect of this beam contamination on the energy deposition distribution, subsequent areas of investigation should include a beam-defining device into the irradiation geometry simulation. The combinatorial geometry module of MORSE code is capable of doing this, but the volume detector analysis module of MORSE-E code should be combined into the MORSE code to produce good results. This kind of Monte Carlo simulation, however, is expected to be very consuming on computer time.

BIBLIOGRAPHY

1. "Cancer - A Progress Report", Newsweek, Nov. 2, 1981.

2. "Cancer," Encyclopaedia Britannica; Vol. 4, (1973).

3. "Radiology," Encyclopaedia Britannica; Vol. 18, (1973).

4. W. J. Meredith, and J. B. Massey, Fundmental Physics of Radiology. Baltimore: Williams & Wilkins Co., pp. 364-369, (1968).

5. R. F. Nelson, "High Energy Electron Beam Treatment Planning for Betatron 10-24 Mev," Acta Radioligica, Vol.9, (1970).

6. Florence C. H. Chu, "Experience with Electron Irradiation of Breast Cancer," p.343 of Symposium on High-Energy Electrons--Montreux 1964, Zuppinger and Poretti, eds. (Springer Verlag, Berlin).

7. D. W. Anderson, Oral Roberts Univ., private communication.

8. International Commission on Radiation Units and Measurements. ICRU Report 21, "Radiation Dosimetry: Electrons with Initial Energies between 1 and 50 MeV," Washington, D.C., pp. 42-46,(1974).

9. H. Svensson, and G. Hettinger, "Measurement of Doses from High-Energy Electron Beam at Small Phantom Depths," Acta Radiologica, Vol. 6, (1967).

10. M. J. Berger and S. M. Seltzer, "ETRAN Monte Carlo Code System for Electron and Photon Transport Through Extended Media," CCC-107, Rodiation Shielding Information Center, Oak Ridge National Lab., June 1968,

11. M. J. Berger and S. M. Seltzer, in 12th Int. Cong. Radiol., Tokyo, 1969.

12. A. E. Nahum, "Calculations of Electron Flux Spectra in Water Irradiated with Megvoltage Electron and Photon Beams with Applications to Dosimetry," Univ. of Edinburgh, Ph.D. Thesis, (1976).

13. A. Özdemir, "Electron Transport Using the Discrete Ordinates Method," Univ. of Oklahoma, Ph.D. Thesis, (1981).

14. W. W. Engle, Jr., "A User's Manual for ANISN: A One-Dimensional Discrete Ordinates Transport Code with Anisotropic Scattering," USAEC report K-1693, Oak Ridge National Lab., 1967.

15. F. R. Mynatt, A User's Manual for DOT, A Two-Dimensional Discrete Ordinates Transport Code with Anisotropic Scattering, CCC-89, RSIC, Oak Ridge National Lab. (1968).

16. K. D. Lathrop, TWOTRAN, A FORTRAN Program for Two-Dimensional Transport, Report GA-8747, Gulf General Atomic, Inc.,1968.

17. E. A. Straker, P. N. Stevens, D. C. Irving, and V. R. Cain, MORSE Code: A Multigroup Neutron and Gamma-Ray Monte Carlo Transport Code, USAEC Report ORNL-4585, Oak Ridge National Lab., 1970.

18. EURATOM European Shielding Information Service, MORSE-E: A General Purpose Monte Carlo Multigroup Neutron and Gamma-Ray Transport Code, RSIC Code Package CCC-258, Oak Ridge National Lab., 1975.

19. D. L. Anderson, "The Discovery of the Electron," Van Nostrand, 1964.

20. R. D. Evans, The Atomic Nucleus, McGraw-Hill Book Co., New York (1955).

21. H. A. Bethe and J. Ashkin, Experimental Nuclear Physics, E. Segre, ed., Vol. I, "Passage of Radiation through Matter," John Wiley and Sons, Inc., New York (1953).

22. C. D. Zerby and F. L. Keller, "Electron Transport Theory, Calculations, and Experiments," Nucl. Sci. Eng., 27, pp. 190-218 (1967).

23. U. Fano, Phys. Rev., 92, p. 328 (1953).

24. M. J. Berger and S. M. Seltzer, "Tables of Energy Losses and Ranges of Electrons and Positrons," NAS-NRC Publ.1133(1964).

25. B. B. Rossi and K. I. Greisen, Revs. Mod. Phys., 13, p. 240 (1941).

26. H. A. Bethe, Handbuch der Physik, Julius Springer, Berlin, Vol. 24, p.273, (1933).

27. C. Møller, Ann. Physik, 14, p.531 (1932).

28. H. A. Bethe and W. Heitler, Proc. Roy. Soc. (London), A146, p. 83 (1934).

29. R. E. Lapp and H. L. Andrews, Nuclear Radiation Physics, Prentice-Hall, Inc., Englewood Cliffs, N. J. p.265, (1972).

30. R. D. Birkhoff, Handbuch der Physik, S. Flugge, ed., Vol.34, Springer-Verlag, Berlin (1958).

31. G. A. Goudsmit and J. L. Saunderson, Phys. Rev., 57, p.24, (1940).

32. H. A. Bethe, Ann. Physik, 5, p. 325, (1930).

33. F. Rohrlich and B. C. Carlson, Phys. Rev., 93, p.38, (1954).

34. E. J. Williams, Proc. Roy. Soc. London, 125, p.420, (1929).

35. L. Landau, J. Phys. USSR, 8, p.201, (1944).

36. J. Blunck and S. Leisegang, Z. Physik, 128, p.500, (1950).

37. W. Borsch-Supan, J. Res. Natl. Bur. Std., 65B, p.245, (1961).

38. O. Blunck and K. Westphal, Z. Physik, 130, p.641, (1951).

39. W. T. Scott, Rev. Mod. Phys., 35, p.231, (1963).

40. M. J. Berger, Methods in Computational Physics, Vol. I, Eds. B. Edler, S. Fernbach, and M. Rotenberg, "Monte Carlo Calculation of Penetration and Diffusion of Fast Charged Particles," p.135, Academic Press, New York (1963).

41. P. N. Stevens, D. K. Trubey, C. W. Garrett, and W. E. Selph, "Radiation Transport," Reactor Shielding for Nuclear Engineers, Ed. N. M. Schaeffer, pp. 119-159, (1973).

42. M. Clark, Jr. and K. F. Hansen, Numerical Methods of Reactor Analysis, Academic Press, New York, pp. 223-231, (1964).

43. L. V. Spencer, "Theory of Electron Penetration," Phys. Rev., 98, p. 1597, (1955).

44. L. V. Spencer and U. Fano, Calculation of Spatial Distributions by Polynomial Expansion, J. Res. Nat. Bur. Stand., 46, p.446, (1951).

45. H. Goldstein and J. E. Wilkins, Jr., Calculations of the Penetration of Gamma Rays, NYO-3075, (1954).

46. J. Certaine, A Solution of Neutron Transport Equation, Part II: NDA Univac Moment Calculations, NYO-6268, (1955).

47. U. Fano, L. V. Spencer and M. J. Berger, Penetration and Diffusion of X-rays, Encyclopedia of Physics, S. Flugge (Ed.), Springer-Verlag, New York, p. 724, (1959).

48. H. W. Lewis, Phys. Rev., 78, p. 526, (1950).

49. L. V. Spencer, "Energy Dissipation by Fast Electrons," Nat. Bur. of Stand, Monograph 1, (1959).

50. P. N. Stevens, D. K. Trubey, C. W. Garrett, and W. E. Selph, "Radiation Transport," Reactor Shielding for Nuclear Engineers, Ed. N. M. Schaeffer, pp. 132-148, (1973).

51. M. Clark, Jr. and K. F. Hansen, Numerical Methods of Reactor Analysis, Academic Press, New York, pp. 204-223, (1964).

52. B. G. Carlson, Solution of the Transport Equation by Sn Approximation, LA-1891, (1955).

53. J. E. Morel, Nucl. Sci. & Eng., 71, p.64, (1979).

54. D. E. Bartine, W. W. Engle Jr., et al., "Low Energy Electron Transport by Method of Discrete Ordinates," Nucl. Sci. Eng., 48, p. 159, (1972).

55. M. Clark, Jr. and K. F. Hansen, Numerical Methods of Reactor Analysis, Academic Press, New York, pp. 239-276, (1964).

56. D. O. Schneider and D. V. Cormack, Radiation Research, 11, p. 418, (1958).

57. M. J. Berger and S. M. Seltzer, Ann. New York Acad. Sci., 161, p. 8, (1969).

58. J. A. Halbleib, Sr., "ACCEPT: A Three-Dimensional Electron/Photon Monte Carlo Transport Code Using Combinatorial Geometry," CCC-374, RSIC, Oak Ridge National Lab. (1979).

59. D. H. Rester and J. H. Derrickson, Journal of Applied Physics, 42, p. 714, (1971).

60. W. Alexander, A. Brynjolesson and R. D. Cooper. "Charge Distribution of High-Energy Electrons in Light Materials", U. S. Army Natick Lab., Technical Report FD-2 (1964).

APPENDIX I

RELATIONSHIP BETWEEN THE LEGENDRE COEFFICIENTS FOR SINGLE ELASTIC SCATTERING AND MULTIPLE SCATTERING

A. Single Scattering

For a homogeneous transport medium, the scattering cross-section is a function of only the angle θ_o between the vectors Ω' and Ω, which are the direction of motion before and after the scattering [51]. It is convenient to consider the variable $\cos\theta_o = \mu_o$, rather than θ_o itself. The scattering cross-section can be expanded in terms of the Legendre polynomials $P_n(\mu_o)$. Thus, we have

$$\sigma_s(\mu_o) = \frac{1}{2\pi} \sum_{n=o}^{\infty} \left(\frac{2n+1}{2}\right) \sigma_{s,n} \; P_n(\mu_o) \quad , \tag{A.1}$$

the factor $\frac{2n+1}{4\pi}$ being inserted for later convenience. From the orthogonality of the Legendre polynomials [50], we get

$$\sigma_{s,n} = 2\pi \int_{-1}^{1} d\mu_o \, \sigma_s(\mu_o) \, P_n(\mu_o) \quad , \tag{A.2}$$

The physical interpretation of $\sigma_{s,n}$ may be made for the following special cases:

(1). If the scattering is isotropic, $\sigma_s(\mu_o)$ is a constant in μ_o, thus

$$\sigma_{s,n} = 0 \qquad n > 0$$

and $\sigma_s(\mu_o) = \frac{\sigma_{s,o}}{4\pi} = \frac{\text{probability of scatter}}{\text{unit solid angle}} = \frac{\sigma_s}{4\pi}$

where $\sigma_s = \int_{4\pi} \sigma_s(\Omega)\, d\Omega = \int_{-1}^{1} 2\pi\sigma_s(\mu_o)\, d\mu_o$

= total physical scattering cross-section,

therefore, $\sigma_{s,o} = \sigma_s$.

Based upon the above discussion, the following conclusions may be drawn:

(i). The first order expansion coefficient, $\sigma_{s,o}$, is identical with the total physical scattering cross-section, σ_s.

(ii). The higher order coefficients are corrections (linear, quadratic, etc.) for anisotropy of scattering.

(iii). For isotropic scattering, the expansion coefficients may be put into the simple expresions of

$$\sigma_{s,o} = \sigma_s \qquad (A.3)$$

$$\sigma_{s,n} = 0 \quad \text{for } n \neq 0 \qquad (A.4)$$

(2). If the scattering is totally forward, the scattering cross-section may conventionally be defined as the (Dirac) delta function $\delta(\mu_o - 1)$ by

$$\sigma_s(\mu_o) = \delta(\mu_o - 1) = 0 \quad \text{for } \mu_o \neq 1$$

$$\int_{-1}^{1} \delta(\mu_o - 1)\, d\mu_o = 1 . \qquad (A.5)$$

These equations imply

$$\int_{-1}^{1} f(\mu_o)\, \delta(\mu_o - 1)\, d\mu_o = f(1) \qquad (A.6)$$

for any function $f(\mu_o)$. Substituting $f(\mu_o) = P_n(\mu_o)$ into Eq. (A.6), we have

$$\sigma_{s,n} = \int_{-1}^{1} P_n(\mu_o)\, \delta(\mu_o - 1)\, d\mu_o = P_n(1) \quad , \qquad (A.7)$$

From the characteristic of Legendre polynomials, Eq. (A.7) can be simplified as

$$\sigma_{s,n} = 1 \qquad \text{for all } n \ .$$

Therefore, for totally forward scattering, all expansion coefficients have the value of 1.

B. Multiple Elastic Scattering

As discussed in Chapter II, Goudsmit and Saunderson [31] developed a theory of multiple elastic scattering. In their theory, the distribution of scattering is represented as a series in Legendre polynomials by the following expression

$$F(\mu, t) = \sum_{n=0}^{\infty} \left(\frac{2n+1}{2}\right) \exp\left(-\int_o^t K_n(t')\, dt'\right) P_n(\mu) \qquad (A.8)$$

where $K_n(t) = \int_{-1}^{1} 2\pi N\, \sigma_s(\mu, t) \left(1 - P_n(\mu)\right) d\mu \qquad (A.9)$

and $F(\mu, t)$ = the distribution function at depth t in material, (t is equal to the size of a "short step" in the ETRAN computer code system)

$P_n(\mu)$ = a legendre polynomial of degree n

$\sigma_s(\mu, t)$ = scattering cross-section per unit solid angle

N = atoms per unit volume.

The single elastic cross-section σ_s is a function of energy, but it is assumed that there exists a unique relationship between energy and depth t. In a homogeneous medium, this cross-section

can be expanded in terms of Legendre polynomials. Thus

$$\sigma_s(\mu,t) = \frac{1}{2\pi} \sum_{m=0}^{\infty} \left(\frac{2m+1}{2}\right)\sigma_{s,m}(t) P_m(\mu) \quad . \qquad (A.10)$$

Equation (A.8) can be rewritten in the following form

$$F(\mu,t) = \sum_{n=0}^{\infty} \left(\frac{2n+1}{2}\right) H_n(t) P_n(\mu)$$

where the Legendre expansion coefficients, $H_n(t)$, for multiple elastic scattering are defined by

$$H_n(t) = \exp\left(-2\pi N \int_{-1}^{1} \sigma_s(\mu,t)\left(1- P_n(\mu)\right) d\mu\right)$$

$$= \exp\left(-2\pi N \int_0^t \int_{-1}^{1} \left(\frac{1}{2\pi} \sum_{m=0}^{\infty} \left(\frac{2m+1}{2}\right)\sigma_{s,m}(t)' P_m(\mu)\right)\right.$$

$$\left.\left(1- P_n(\mu)\right) d\mu\, dt'\right)$$

Using the orthogonality property of the Legendre polynomials, the expansion coefficients can be obtained as

$$H_n(t) = \exp\left(-N \int_0^t \left(\sigma_{s,o}(t') - \sigma_{s,n}(t')\right) dt'\right) \quad . \qquad (A.11)$$

Equation (A.11) gives the relationship between the Legendre expansion coefficients of single elastic scattering and multiple elastic scattering. No particular meanings are given to the multiple scattering expansion coefficients, rather, they may be regarded as a transform. The physical interpretation of $H_n(t)$ may be understood in the following special cases:

(1). If the target thickness t approaches zero, the multiple elastic scattering cross-section should reflect a totally forward scattering. From Eq. (A.11), we get

$$\lim_{t\to o} H_n(t) = \lim_{t\to o} \exp\left(-N\int_o^t \left(\sigma_{s,o}(t') - \sigma_{s,n}(t')\right)dt'\right)$$

$$= \exp(0)$$

$$= 1 \qquad \text{for all } n .$$

This is identical with the totally forward single elastic scattering cross-section discussed earlier in this appendix.

(2). If the target thickness t is extremely large, the Legendre expansion coefficients of the multiple scattering cross-section have the following property

$$\lim_{t\to\infty} H_n(t) = \lim_{t\to\infty} \exp\left(-N\int_o^t \left(\sigma_{s,o}(t') - \sigma_{s,n}(t')\right)dt'\right)$$

$$= \begin{cases} 1 & \text{for } n = 0 \\ 0 & \text{for } n \neq 0 \end{cases}$$

This implies the thicker the distance traveled, the more isotropic the multiple scattering cross-section should be. In the case of an extreme thickness, the expansion coefficients of multiple scattering become identical with those coefficients of an isotropic single elastic scattering.

APPENDIX II

ELECTRON TRANSPORT CROSS-SECTION PROCESSING PROGRAM

```
C
C
C       ETCSPP (ELECTRON TRANSPORT CROSS-SECTION PROCESSING PROGRAM)
C
C       THIS PROGRAM CONVERTS THE ELECTRON STOPPING POWER DATA READ FROM
C       DATAPAC6 CALCULATIONS INTO MULTI-GROUP ELECTRON TRANSPORT CROSS-
C       SECTION DATA IN ANISN FORMAT.
C
C
C       FORMAT OF CARD INPUT FOR ETCSPP
C
C
C       EMAX,NCYC,KMAX,NGS,ISUB,LMAX      F10.0,5I5
C       LEXT                              I5
C       ZEFF,AM,RHO                       3F10.0
C       MGIT,IGTOG,IMAX,IPCS,IPAC         5I5
C       N1,N2,N3,(HOL(I),I=1,6)           3I6,6A8
C
C
C       MEANING OF INPUT VARIABLES FOR PROGRAM ETCSPP
C
C
C  EMAX    ENERGY (IN MEV) OF PRIMARY ELECTRONS INCIDENT ON TARGET.
C  NCYC    PARAMETER INDICATING FINENESS OF ENERGY GRID. THE NUMBER OF
C          GRID INTERVALS REQUIRED TO REDUCE THE ENERGY BY A FACTOR OF
C          TWO IS EQUAL TO NCYC.
C  KMAX    KMAX+1 IS THE NUMBER OF ENERGY GROUPS FOR WHICH CROSS SECTIONS
C          ARE STORED.
C  NGS     NUMBER OF ENERGY GROUPS SKIPPED BY A CATASTROPHICALLY COLLIDED
C          ELECTRON. FOR CONTINUOUS-SLOWING-DOWN MODEL, NGS=1. FOR GROUP-
C          SKIPPING MODEL, NGS IS GREATER THAN 1 AND LESS THAN NCYC.
C  ISUB    PARAMETER RELATING TO THE DIVISION OF ELECTRON STEPS INTO
C          SUBSTEPS. AN INTERGER EQUALS TO OR GREATER THAN 1 . THE SIZE
C          OF SUBSTEPS = THE SIZE OF STEPS DIVIDED BY ISUB.
C  LMAX    NUMBER OF LEGENDRE COEFFICIENTS , INCLUDING P0.
C  LEXT    NUMBER OF LEGENDRE COEFFICIENTS FOR THE EXTENDED TRANSPORT
C          WITHIN-GROUP CROSS SECTIONS. AN INTEGER EQUALS TO OR LESS
C          THAN LMAX.
C  ZEFF    EFFECTIVE ATOMIC NUMBER OF THE TRANSPORT MEDIUM.
C  AM      ATOMIC OR MOLECULAR WEIGHT OF THE TRANSPORT MEDIUM.
C  RHO     DENSITY OF THE TRANSPORT MEDIUM, IN GRAMS PER C.C..
C  MGIT    1  THE CROSS-SECTION DATA IS PRODUCED IN THE GROUP INDEPENDENT
C             TAPE FORMAT.
C          0  THE CROSS-SECTION DATA IS PRODUCED IN THE STANDARD ANISN
C             FORMAT.
```

```
C **********
C   MAIN PROGRAM
      REAL*8 T(100),EBLOS(100),BLOS(100),ELOS(100) ,H(100,240)
      REAL*8 ECATL(100),ECLOS(100)
      COMMON /COEF/CRX(105,50) ,EBLOS,BLOS,ELOS,T,H
      COMMON /EGS/XNCYC,EMAX
      COMMON /MEDIA/ZEFF,AM,RHO
      DIMENSION ETA(100) ,E(100),W(100,50),ICTR(100),Y(100,50),JCTR(100)
      DIMENSION C(100,105,50),XTEMP(100)
      REAL*8 HOL(6)
      READ(5,111)  EMAX,NCYC,KMAX,NGS,ISUB,LMAX
  111 FORMAT(F10.0,5I5)
      IF(NGS.LT.NCYC) GO TO 127
      WRITE(6,125)
  125 FORMAT(//,10X,' ** ERROR ** NGS NOT LESS THAN NCYC.')
      STOP
  127 CONTINUE
      XMAX=0.50
      READ(5,1) LEXT
    1 FORMAT(I5)
      READ(5,102) ZEFF,AM,RHO
  102 FORMAT(3F10.0)
      WRITE(6,*)  EMAX,NCYC,KMAX,NGS,ISUB,LMAX
      XNCYC=FLOAT(NCYC)
      READ (5,103) MGIT,IGTOG,IMAX,IPCS,IPAC
  103 FORMAT(5I5)
      WRITE(6,*) ZEFF,AM,RHO
      WRITE(6,*) MGIT,IGTOG,IMAX,IPCS,IPAC
      IF(NGS.GT.1) GO TO 95
      XCUT=0.50
      GO TO 97
   95 CALL XFRAC(XMAX,NGS,XCUT)
   97 CONTINUE
      CALL SINGS(XCUT,LMAX,KMAX,W,ICTR,Y,JCTR)
      KMAX1=KMAX+1
      WRITE(6,1212) LMAX
 1212 FORMAT('1EXPANSION ORDER OF DOWN-SCATTER CROSS-SEC IS',I5)
      KMAX5=KMAX+5
      NGS1=NGS+1
      READ(5,701) N1,N2,N3,(HOL(I),I=1,6)
  701 FORMAT(3I6,6A8)
      L1 = LEXT+1
      L2= L1+1
      L3= L2+1
      CALL READIN(N,LMAXI,K,IPAC)
      NP1=N+1
      I1=IGTOG
```

```
C  IGTOG  LOCATION OF WITHIN-GROUP SCATTERING CROSS SECTIONS, USUALLY 5.
C  IMAX   TABLE LENGTH, I.E., THE NUMBER OF CROSS SECTIONS FOR EACH GROUP.
C        USUALLY EQUAL TO IGTOG+NGS.
C  IPCS   1  PRINTOUT THE CROSS SECTION DATA
C        0  DO NOT PRINTOUT CROSS-SECTION DATA.
C  IPAC   1  PRINTOUT THE DATAPAC DATA READ FROM TAPE UNIT 20
C        0  DO NOT PRINTOUT THE DATA READ FROM TAPE UNIT 20
C  N1,N2,N3,(HOL(I),I=1,6)   ARE PART OF THE IDENTIFICATION RECORD
C        (4I6,6A8) PRECEDES THE CROSS SECTIONS FOR EACH COEFFICIENT.
C        THIS IDENTIFICATION RECORD IS REQUIRED IN THE MORSE CODE.
C        THE ELEMENT IDENTIFIER WHICH MUST BE THE FOURTH INTEGER IN
C        THE IDENTIFICATION RECORD IS SEQUENTIALLY DEFINED IN THE
C        PROGRAM WITH VALUES FROM 1 TO LMAX.
C
C
C
C     BRIEF DESCRIPTION OF SUBROUTINES USED IN ETCSPP
C
C
C  MAIN PROGRAM
C  READS INTO MEMORY THE VARIOUS RUN PARAMETERS .
C  CALAULATES THE MACROSCOPIC ENERGY ABSORPTION CROSS-SECTION
C  AND THE MACROSCOPIC TRANSPORT CROSS-SECTION .
C  WRITES OUTPUT DATA ONTO A TAPE (UNIT 64).
C
C  SUBROUTINE READIN
C  READS INTO MEMORY VARIOUS DATA CALCULATED BY DATAPAC6 (FROM TAPE
C  UNIT 20). THE DATA INCLUDES ENERGY GROUP NUMBER, NUMBER OF LEGENGRE
C  COEFFICIENTS FOR EACH GROUP, MEAN ENERGY OF EACH GROUP, TOTAL,
C  RADIATIVE AND COLLISIONAL STOPPING POWER, AND MULTIPLE ELASTIC
C  SCATTERING COEFFICIENTS FROM GOUDSMIT-SAUNDERSON DISTRIBUTION.
C
C  SUBROUTINE EXTEND
C  USES THE EXTENDED TRANSPORT THEORY TO REDUCE THE COEFFICIENTS OF
C  WITHIN-GROUP CROSS SECTIONS TO LEXT+1 TERMS.
C
C  SUBROUTINE SINGS
C  CALCULATES THE NORMALIZED LEGENDRE EXPANSION COEFFICIENTS FOR
C  MODERATE INELASTIC COLLISION TO THE NEXT LOWER GROUP AND FOR
C  CATASTROPHIC COLLISION TO THE GROUP DOWN-SCATTERED BY NGS GROUPS.
C
C  SUBROUTINE POLY
C  CALAULATES THE LEGENDRE POLYNOMIAL.
C
C  SUBROUTINE XFRAC
C  CALAULATES THE CUT-OFF VALUES OF FRACTIONAL ENERGY TRANSFER FOR
C  MODERATE INELASTIC COLLISION OR CATASTROPHIC COLLISION.
```

```
C **********
C   MAIN PROGRAM
      REAL*8 T(100),EBLOS(100),BLOS(100),ELOS(100) ,H(100,240)
      REAL*8 ECATL(100),ECLOS(100)
      COMMON /COEF/CRX(105,50) ,EBLOS,BLOS,ELOS,T,H
      COMMON /EGS/XNCYC,EMAX
      COMMON /MEDIA/ZEFF,AM,RHO
      DIMENSION ETA(100) ,E(100),W(100,50),ICTR(100),Y(100,50),JCTR(100)
      DIMENSION C(100,105,50),XTEMP(100)
      REAL*8 HOL(6)
      READ(5,111)  EMAX,NCYC,KMAX,NGS,ISUB,LMAX
  111 FORMAT(F10.0,5I5)
      IF(NGS.LT.NCYC) GO TO 127
      WRITE(6,125)
  125 FORMAT(//,10X,' ** ERROR ** NGS NOT LESS THAN NCYC.')
      STOP
  127 CONTINUE
      XMAX=0.50
      READ(5,1) LEXT
    1 FORMAT(I5)
      READ(5,102) ZEFF,AM,RHO
  102 FORMAT(3F10.0)
      WRITE(6,*)  EMAX,NCYC,KMAX,NGS,ISUB,LMAX
      XNCYC=FLOAT(NCYC)
      READ (5,103) MGIT,IGTOG,IMAX,IPCS,IPAC
  103 FORMAT(5I5)
      WRITE(6,*) ZEFF,AM,RHO
      WRITE(6,*) MGIT,IGTOG,IMAX,IPCS,IPAC
      IF(NGS.GT.1) GO TO 95
      XCUT=0.50
      GO TO 97
   95 CALL XFRAC(XMAX,NGS,XCUT)
   97 CONTINUE
      CALL SINGS(XCUT,LMAX,KMAX,W,ICTR,Y,JCTR)
      KMAX1=KMAX+1
      WRITE(6,1212) LMAX
 1212 FORMAT('1EXPANSION ORDER OF DOWN-SCATTER CROSS-SEC IS',I5)
      KMAX5=KMAX+5
      NGS1=NGS+1
      READ(5,701) N1,N2,N3,(HOL(I),I=1,6)
  701 FORMAT(3I6,6A8)
      L1 = LEXT+1
      L2= L1+1
      L3= L2+1
      CALL READIN(N,LMAXI,K,IPAC)
      NP1=N+1
      I1=IGTOG
```

```
      I2=I1+1
      LMAXX=LMAXI-1
      WRITE(6,2) LMAXX
    2 FORMAT('1ORDER OF EXTENDED TRANSPORT IN-GROUP CROSS SECTION=',I5)
      WRITE(6,3) LEXT
 3    FORMAT('0ORDER OF EXTENDED TRANSPORT X-S(IN-GR) SET IS',I5)
      KMN=KMAX-NGS
      DO 134 I=1,KMAX1
      ECAT=T(I)-T(I+NGS)
      IF(I.GT.KMN) GO TO 132
      E(I)=T(I)/0.511
      E1=(2*E(I)+1.)/(E(I)+1.)**2
      E2=(E(I)/(E(I)+1.))**2
      E3=((E(I)+1.)/E(I))**2/(E(I)+2.)
      CE=0.30057*T(I)*E3*ZEFF/AM
      U1=ALOG(XMAX)+1./(1.-XMAX)+(1.+E1)*ALOG(1.-XMAX)+
     % 0.5*E2*XMAX**2
C
      U2=ALOG(XCUT)+1./(1.-XCUT)+(1.+E1)*ALOG(1.-XCUT)+
     % 0.5*E2*XCUT**2
      ECATL(I)=CE*(U1-U2)
      GO TO 134
  132 DO 133 K=I,KMAX1
  133 ECATL(K)=0.0
      GO TO 136
  134 CONTINUE
  136 CONTINUE
      DO 1117 KK=1,KMAX1
      WRITE(6,1114) KK,EBLOS(KK),ELOS(KK),BLOS(KK),ECATL(KK)
 1114 FORMAT(/,5X,I5,5X,4E13.6)
 1117 CONTINUE
C **********
C  CALCULATION OF FIRST BLOCK. K=1 CASE
      K=1
      SUM=0.0
      DO 5 I=1,KMAX5
      DO 5 J=1,LMAX
   5  CRX(I,J)=0.0
      ECLOS(1)=EBLOS(1)-ECATL(1)
      CRX(1,1)=ECLOS(1)*RHO
      SUM=SUM+ECLOS(1)
      CRX(4,1)=ECLOS(1)/(T(1)-T(2)) * RHO
      CRX(5,1)=ECLOS(1)/(T(1)-T(2) ) * RHO*ISUB
      CRXCAT=ECATL(1)/(T(1)-T(NGS1))*RHO
      CRX(4,1)=CRX(4,1)+CRX(5,1)+CRXCAT
      DO 8 J=2,LMAX
 8    CRX(5,J) = CRX(5,1)     *(2*(J-1)+1)*H(1,J)
      CALL  EXTEND(L1,L2,L3,LMAX,I1)
```

```
      IF(MGIT.NE.0) GO TO 9
      DO 707 I=1,KMAXS
      DO 707 J=1,LMAX
  707 C(K,I,J)=CRX(I,J)
      GO TO 709
    9 WRITE(64) ((CRX(I,J),I=1,IMAX),J=1,LMAX)
  709 CONTINUE
C ***************
C  CALCULATION OF ALL OTHER BLOCKS  K=2,3,4,...N  CASE
      DO  30  K=2,N
      ICTRI=ICTR(K)
      JCTRI=JCTR(K)
      DO 7 I=1,KMAXS
      DO 7 J=1,LMAX
      CRX(I,J)=0.0
    7 CONTINUE
      ECLOS(K)=EBLOS(K)-ECATL(K)
      CRX(1,1)=ECLOS(K) *RHO
      SUM=SUM+ECLOS(K)
      CRX(4,1)=ECLOS(K)/(T(K)-T(K+1)) * RHO
      DO 20 J=1,LMAX
      CRX(I1,J)=ECLOS(K)*(2*J-1)*H(K,J)/(T(K)-T(K+1))*RHO*ISUB
      XTEMP(J)=CRX(I1,J)/ISUB
   20 CONTINUE
      DO  22 L=1,LMAX
      CRX(I2,L) =ECLOS(K-1)*(2*L-1)*W(K-1,L)/(T(K-1)-T(K))*RHO
   22  CONTINUE
      IF(NGS.EQ.1) GO TO 24
      IF(K.LT.NGS1) GO TO 24
      DO 23 L=1,LMAX
      CRX(IMAX,L)=ECATL(K-NGS)*(2*L-1)*Y(K-NGS,L)/(T(K-NGS)-T(K))*RHO
   23 CONTINUE
   24 CONTINUE
      CRXCAT=ECATL(K)/(T(K)-T(K+NGS))*RHO
      CRX(4,1)=CRX(I1,1)+CRX(4,1)+CRXCAT
      CALL  EXTEND(L1,L2,L3,LMAX,I1)
      IF(MGIT.NE.0) GO TO 29
      DO 737 I=1,KMAXS
      DO 737 J=1,LMAX
  737 C(K,I,J)=CRX(I,J)
      GO TO 739
   29 WRITE(64) ((CRX(I,J),I=1,IMAX),J=1,LMAX)
  739 CONTINUE
   30 CONTINUE
C ******************
C  CALCULATION OF  FINAL GROUP CROSS-SECTION
C  USE SUM AS BIG X-S  TO DEPOSIT ALL REMAINING ENERGY
      K=N+1
```

```
      ICTRI=ICTR(K)
      T(K-1)=T(N)
      T(K)=T(N)*T(N)/T(N-1)
      T(K+1) =T(K)*T(K)/T(K-1)
      T(K+2)=T(K+1) * T(K+1) / T(K)
      CRX(4,1)=SUM/(T(K)-T(K+1)) * RHO
      EBLOS(K)=EBLOS(N)
      DO 35 I=1,KMAX5
      DO 35 J=1,LMAX
   35 CRX(I,J)=0.0
      CRX(1,1)=SUM *RHO
      CRX(4,1)=SUM/(T(K)-T(K+1) ) * RHO
      DO 36 J=1,LMAX
      CRX(I1,J)=EBLOS(K)*(2*J-1)*H(K-1,J)/(T(K)-T(K+1))*RHO*ISUB
   36 CONTINUE
      CRX(4,1)=CRX(I1,1)+CRX(4,1)
      DO 41  L=1,LMAX
      CRX(I2,L)=XTEMP(L)
   41 CONTINUE
      CRX(2,1)= CRX(4,1) - CRX(I1,1)
      CALL  EXTEND(L1,L2,L3,LMAX,I1)
      IF(MGIT.NE.0) GO TO 149
      DO 757 I=1,KMAX5
      DO 757 J=1,LMAX
  757 C(K,I,J)=CRX(I,J)
      GO TO 759
  149 WRITE(64) ((CRX(I,J),I=1,IMAX),J=1,LMAX)
      GO TO 778
  759 CONTINUE
      DO 777 J=1,LMAX
      WRITE(64)N1,N2,N3,J,(HOL(I),I=1,6)
  702 FORMAT(///,4I6,6A8)
      WRITE(64)((C(K,I,J),I=2,KMAX5),K=1,KMAX1)
      IF(IPCS.EQ.0) GO TO 777
      WRITE(6,702) N1,N2,N3,J,(HOL(I),I=1,6)
      DO 777 I=1,IMAX
      WRITE(6,48) I, (C(K,I,J),K=1,KMAX1)
  777 CONTINUE
      WRITE(6,652)
  652 FORMAT(//,9X,' ENERGY ABSORPTION CROSS SECTION FOR ELECTRON ENERGY
     $ GROUPS ARE: ')
      WRITE(6,700) (C(K,1,1),K=1,KMAX1)
  700 FORMAT(//,(/,10X,5F13.5))
  778 CONTINUE
      ENDFILE 64
      REWIND 64
      IF(MGIT.EQ.0) GO TO 799
      IF(IPCS.EQ.0) GO TO 799
      NSETS=0
   42 READ(64,END=50) ((CRX(I,J),I=1,IMAX),J=1,LMAX)
```

```
   43  NSETS=NSETS+1
       WRITE(6,45) NSETS
    45 FORMAT('0ENERGY GROUP NUMBER ',I5,//)
       DO 47 I=1,IMAX
    47 WRITE(6,48) I, (CRX(I,J),J=1,LMAX)
    48 FORMAT('0I=',I5,/(' ',10X,8E14.5))
       GO TO 42
    50 WRITE(6,52) NSETS
    52 FORMAT('0END OF FILE FOUND  AFTER ',I5,' ENERGY  GROUPS')
   799 CONTINUE
       STOP
       END
C ************************
       SUBROUTINE READIN(N,LBIG,K,IPAC)
       REAL*8 T(100),EBLOS(100),BLOS(100),ELOS(100) ,H(100,240)
       REAL*8 ECATL(100),ECLOS(100)
C LBIG IS THE VALUE OF LMAXI FOR FIRST ENERGY GROUP
C MAXIMUM NUMBER OF ENERGY GROUP IS 100
       COMMON /COEF/CRX(105,50) ,EBLOS,BLOS;ELOS,T,H
       HMIN=1.0E-5
       KLAST=100
       LLAST=240
   10  READ(20,END=22) K,LMAXI,T(K), EBLOS(K),BLOS(K),ELOS(K),
      1   (H(K,L),L=1,LMAXI)
       IF(IPAC.EQ.0) GO TO 15
       WRITE(6,9)K,LMAXI,T(K),EBLOS(K),BLOS(K),ELOS(K),(H(K,L),L=1,LMAXI)
     9 FORMAT(2I6,4F10.6,30(/8(2X,F12.7)))
    15 CONTINUE
       IF(K.GT.1) GO TO 19
       DO 17 L=1,LMAXI
       IF(H(1,L).LT.HMIN) GO TO 18
 17    CONTINUE
       IF(L.GT.LMAXI) L=LMAXI
 19    CONTINUE
 18    LBIG=L
       IF(LMAXI.GT.LLAST) GO TO 24
       IF(K.GT.KLAST) GO TO 24
       GO TO 10
 22    N=K
       T(N+1)=T(N)*T(N)/T(N-1)
       T(N+2)= T(N+1) * T(N+1)/ T(N)
       RETURN
    24 WRITE(6,25) K,KLAST,LMAXI,LLAST
    25 FORMAT('0CHECK DIMENSIONS ',I5,' .GT.',I5,' .OR. ',I5,' .GT.',I5)
       STOP
       END
C  **********
       SUBROUTINE EXTEND(L1,L2,L3,LMAX,IG)
       REAL*8 T(100),EBLOS(100),BLOS(100),ELOS(100) ,H(100,240)
       REAL*8 ECATL(100),ECLOS(100)
```

```
      COMMON /COEF/CRX(105,50) ,EBLOS,BLOS,ELOS,T,H
      C1 = CRX(IG,L2)/(2*L1+1)
      TEMP1=CRX(IG,1)
      DO 25 J=1,L2
      CRX(IG,J) = CRX(IG,J)-(2*(J-1)+1)*C1
      TEMP2=CRX(IG,1)
   25 CRX(IG,J)=CRX(IG,J)*TEMP1/TEMP2
      IF(LMAX.LT.L3) GO TO 28
      DO 26 J=L3,LMAX
 26   CRX(IG,J)=0.0
   28 RETURN
      END
C  **********
      SUBROUTINE SINGS(XCUT,LMAX,IGM,W,ICTR,Y,JCTR)
      COMMON /COEF/CRX(105,50) ,EBLOS,BLOS,ELOS,E,H
      COMMON /EGS/XNCYC,EMAX
      COMMON /MEDIA/ZEFF,AM,RHO
      DIMENSION T(100),K(100),K1(100),K2(100),ST(100),C12(100)
      DIMENSION X(100),E(100)
      DIMENSION W(100,50),ICTR(100),Y(100,50),JCTR(100),WN(100),YN(100)
      DIMENSION HE(100),BV(100),EE(100),CM(100)
      REAL MU1,MU2,MUC
      REAL*8 P(50,202),Z(202),DMU(202),T
      REAL*8  ETA(100),CRXI(100)
      REAL    K,K1,K2,ST
      JMAX=200
      LMAX= LMAX + 1
      JMAX1=JMAX-1
      JMAX2=JMAX+1
      JMAX3= JMAX+2
      Z(1)= 0.500D0
      DO 100 J=2,JMAX3
      IF(J.GT.51) GO TO 53
      Z(J)=Z(J-1)+0.004
      GO TO 97
   53 CONTINUE
      IF(J.GT.101) GO TO 55
      Z(J)=Z(J-1)+0.003
      GO TO 97
   55 CONTINUE
      IF(J.GT.151) GO TO 56
      Z(J)=Z(J-1)+0.002
      GO TO 97
   56 Z(J)=Z(J-1)+0.00098
   97 DMU(J-1)=Z(J)-Z(J-1)
  100 CONTINUE
      DO 110 J=1,JMAX2
      Z(J)=0.5D0*(Z(J) + Z(J+1))
  110 CONTINUE
      KMAX=IGM
```

```
      KMAX1= KMAX+1
      KMAX2= KMAX1+1
      KMAX3= KMAX2+1
      FK=1.-0.5**(1./XNCYC)
      EE(1)= 2.0*EMAX/(2.-FK)
      DO  3 I=2,KMAX3
      EE(I)=(1.0-FK)* EE(I-1)
3     CONTINUE
      E(1)=EMAX
      DO 10 IK=2,KMAX2
      E(IK)=  (1.0-FK)* E(IK-1)
10    CONTINUE
      CALL XFRAC(XCUT,1,XETA)
      WRITE(6,112) XCUT
 112  FORMAT(//,10X,' CUTOFF FRACTIONAL ENERGY TRANSFER FOR CATASTROPHIC
     $ COLLISION =',F8.5)
      WRITE(6,113) XETA
 113  FORMAT(//,10X,'   CUTOFF FRACTIONAL ENERGY TRANSFER  FOR  MODERATE
     $ COLLISION =',F8.5)
      IF(XETA.LT.XCUT) GO TO 115
      WRITE(6,114)
 114  FORMAT(//,10X,' *** ERROR *** THE VALUE OF NGS CONFLICTS WITH THE
     $ ENERGY GROUP STRUCTURE. ')
      STOP
 115  CONTINUE
      DO  12 IK=1,KMAX1
      ETA(IK)=E(IK)*XETA
      CM(IK)=E(IK)*(1.0-XCUT)
      HE(IK)=E(IK)/2.000
      BV(IK)= E(IK)-ETA(IK)
12    CONTINUE
      CALL POLY(P,Z,LMAX)
      DO  500 I=1,KMAX1
       T(I)= E(I)   / 0.5110
      K(I)= 1.0  + E(I) / 0.5110
      K1(I)=   (2.0   * K(I)-1.0   ) / (K(I)*K(I) )
      K2(I)=  ((K(I)- 1.0   ) / K(I))**2
      ST(I)= ( 1.0  + 1.0  /T(I) )**2
      C12(I)=7.55417*RHO*ZEFF*ST(I)/AM
      MU1=SQRT((HE(I)*(E(I)+1.022  ))/(E(I)*(HE(I)+1.022   )) )
      DO 41 J=1,JMAX2
      IF(MU1.LE.Z(J)) GO TO 42
41    CONTINUE
42    JMIN=J-1
      MU2= SQRT((BV(I)*(E(I)+1.022   ))/(E(I)*(BV(I)+1.022   )) )
      DO 43 JJJ=1,JMAX2
      IF( MU2.LE.Z(JJJ)) GO TO 44
43    CONTINUE
44    JM=JJJ-1
      MUC=SQRT((CM(I)*(E(I)+1.022))/(E(I)*(CM(I)+1.022)))
```

```
      DO 47 JI=1,JMAX2
      IF(MUC.LE.Z(JI)) GO TO 49
   47 CONTINUE
   49 JC=JI-1
      NDUMMY=0
      IRUN=0
      JDUMMY=0
      JRUN=0
      DO  70 L=1,LMAX
      SUM=0.0
      DO 60  J=JC,JM
      SUM= SUM + Z(J)*P(L,J)*  ((1.0D0/(2.0D0* Z(J)*Z(J) )**2) +
     1 K1(I)/(2.0D0*Z(J)*Z(J)*(Z(J)*Z(J)-1.0D0)* (T(I)+2.0D0) ) +
     2  (1.0D0/((Z(J)*Z(J)-1.0D0)*(T(I)+2.0D0) )**2 ) +
     3  K2(I)/((T(I)*Z(J)*Z(J)-T(I)-2.0D0)**2) )*DMU(J)
60    CONTINUE
      W(I,L)= C12(I) * SUM
      WN(I)=W(I,1)
      IF(W(I,L).GT. 0.0 ) IRUN=IRUN+1
      IF(W(I,L).LT. 0.0   .AND. NDUMMY.EQ. 0 ) GO TO 65
      GO TO 70
65    ICTR(I)= IRUN
      NDUMMY=999
 70   CONTINUE
      DO  77 L=1,LMAX
      SUM=0.0
      DO 75  J=JMIN,JC
      SUM= SUM + Z(J)*P(L,J)*  ((1.0D0/(2.0D0* Z(J)*Z(J) )**2) +
     1 K1(I)/(2.0D0*Z(J)*Z(J)*(Z(J)*Z(J)-1.0D0)* (T(I)+2.0D0) ) +
     2  (1.0D0/((Z(J)*Z(J)-1.0D0)*(T(I)+2.0D0) )**2 ) +
     3  K2(I)/((T(I)*Z(J)*Z(J)-T(I)-2.0D0)**2) )*DMU(J)
75    CONTINUE
      Y(I,L)= C12(I) * SUM
      YN(I)=Y(I,1)
      IF(Y(I,L).GT. 0.0 ) JRUN=JRUN+1
      IF(Y(I,L).LT. 0.0   .AND. JDUMMY.EQ. 0 ) GO TO 76
      GO TO 77
  76  JCTR(I)= JRUN
      JDUMMY=999
 77   CONTINUE
500   CONTINUE
      DO 475 I=1,KMAX1
      DO 476 L=1,LMAX
      W(I,L)= W(I,L)/WN(I)
      Y(I,L)=Y(I,L)/YN(I)
476   CONTINUE
475   CONTINUE
      WRITE(6,525)
 525  FORMAT(1X,'*** I AM WRITING OUT  ICTR(I) VALUES ***' )
      WRITE(6,*) (ICTR(I),I=1,KMAX1)
```

```
      WRITE(6,544)
  544 FORMAT(1X,'*** I AM WRITING OUT  JCTR(I) VALUES ***' )
      WRITE(6,*) (JCTR(I),I=1,KMAX1)
      RETURN
      END
C  **********
      SUBROUTINE POLY(P,Z,LMAX)
C** INDEX  I  IMPLIES THE EXPANSION ORDER  UP TO LMAX
C** INDEX  J  IMPLIES THE  INTEGRATION GRID POINTS I.E.  Z(J)  POINTS
      REAL*8 P(50,202),Z(202) ,G
      JMAX=200
      LMAX=LMAX+1
      DO 10 I=1,LMAX
      DO 20 J=1,JMAX
C**  NEXT 3 CARDS SET  P=0 VALUES
      IF(I.NE.1) GO TO 11
      P(I,J)=1.0D0
      GO TO 20
C** NEXT 3 CARDS SET P=1 VALUES
 11   IF(I.NE.2) GO TO 12
      P(I,J)=Z(J)
      GO TO 20
 12    G=Z(J)*P(I-1,J)
      P(I,J)=G-P(I-2,J)+G-(G-P(I-2,J))/FLOAT(I-1)
  20  CONTINUE
  10  CONTINUE
      RETURN
      END
      SUBROUTINE XFRAC(XC,NGP,X1)
      COMMON /EGS/XNCYC,EMAX
      EPS= 0.0001
      FK=1.-0.5**(NGP/XNCYC)
      T=EMAX/0.511
      T1=(2*T+1)/(T+1.)**2
      T2=(T/(T+1.))**2
      X1=XC*0.95
      DX=0.5*X1
      NN=1
  10  CONTINUE
      U1=ALOG(XC)+1./(1.-XC)+(1.+T1)*ALOG(1.-XC)+0.5*T2*(XC**2)
      U2=ALOG(X1)+1./(1.-X1)+(1.+T1)*ALOG(1.-X1)+0.5*T2*(X1**2)
      V1=-1./XC+1./(1.-XC)+T2*XC+T1*ALOG(1./XC-1.)
      V2=-1./X1+1./(1.-X1)+T2*X1+T1*ALOG(1./X1-1.)
      Y=(U1-U2)/(V1-V2)
      DELTA=Y-FK
      IF(DELTA.GT.EPS) GO TO 50
      IF(ABS(DELTA).GT.EPS) GO TO 70
      WRITE(6,110)NN,X1,Y,FK
      GO TO 100
  50  CONTINUE
```

```
      WRITE(6,110)NN,X1,Y,FK
      X10=X1
      X1=X1-DX
      DX=ABS(0.5*(X10-X1))
      NN=NN+1
      GO TO 10
   70 CONTINUE
      WRITE(6,110)NN,X1,Y,FK
      X10=X1
      X1=X1+DX
      DX=ABS(0.5*(X10-X1))
      NN=NN+1
      GO TO 10
  100 WRITE(6,115)
  110 FORMAT(//,I5,3E13.6)
  115 FORMAT(//,' DESIRED PRECISION IS REACHED. ')
      RETURN
      END
```